

Outbursts and stellar properties of the classical Be star HD 6226

Noel D. Richardson,^{1*} Olivier Thizy,² Jon E. Bjorkman,³ Alex Carciofi,⁴
 Amanda C. Rubio,⁴ Joshua D. Thomas,⁵ Karen S. Bjorkman,³ Jonathan Labadie-Bartz,⁴
 Matheus Genaro,⁴ John P. Wisniewski,⁶ Luqian Wang,⁷ Douglas R. Gies,⁷
 S. Drew Chojnowski,⁸ Andrea Daly,¹ Thompson Edwards,⁵ Carlie Fowler,⁵
 Allison D. Gullingsrud,³ Nolan Habel,³ David J. James,⁹ Emily Kehoe,⁵
 Heidi Kuchta,³ Alexis Lane,¹ Anatoly Miroshnichenko^{10,11,12} Ashish Mishra,³
 Herbert Pablo,¹³ Maurice Peploski,⁵ Joshua Pepper,¹⁴ Joseph E. Rodriguez,¹⁵
 Robert J. Siverd,¹⁶ Keivan G. Stassun,¹⁷ Daniel J. Stevens,^{18,19,20} Jesica L. Trucks,²¹ James Windsor,²²
 Mackenna Wood,⁵ Étienne Bertrand,² Jean-Jacques Broussat,² Erik Bryssinck,²
 Christian Buil,² Stéphane Charbonnel,² Arnold de Bruin,² Joe Dahlen,² Valerie Desnoux,²
 James Dull,²³ Olivier Garde,² Keith Graham,² Kevin Gurney,² Alun Halsey,²
 Patrik Fosaneli,² Joan Guarro Fló,² Franck Houpert,² Foster James,² Christian Kreider,²
 Robin Leadbeater,² Tim Lester,² Dong Li,² Alain Maetz,² Albert Stiewing,²
 Peter Somogyi,² Jean-Noël Terry,² Stéphane Ubaud,² and Ulrich Waldschlaeger²

¹*Department of Physics and Astronomy, Embry-Riddle Aeronautical University, 3700 Willow Creek Road, Prescott, AZ 86301, USA*

²ARAS

³*Ritter Observatory, Department of Physics and Astronomy, The University of Toledo, Toledo, OH 43606-3390, USA*

⁴*Instituto de Astronomia, Geofísica e Ciências Atmosféricas, Universidade de São Paulo, Rua do Matão 1226*

⁵*Department of Physics, Clarkson University, 8 Clarkson Ave, Potsdam, New York 13699, USA*

⁶*Homer L. Dodge Department of Physics and Astronomy, University of Oklahoma, 440 W. Brooks St., Norman, OK 73019, USA*

⁷*Center for High Angular Resolution Astronomy and Department of Physics and Astronomy, Georgia State University, P.O. Box 5060, Atlanta, GA 30302-5060, USA*

⁸*Apache Point Observatory and New Mexico State University, PO Box 59, Sunspot, NM 88349-0059, USA*

⁹*ASTRAVEO, LLC, PO Box 1668, Gloucester, MA 01931, USA*

¹⁰*Department of Physics and Astronomy, University of North Carolina at Greensboro, P.O. Box 26170, Greensboro, NC 27402-6170, USA*

¹¹*Main Astronomical Observatory of the Russian Academy of Sciences, Saint-Petersburg, Pulkovskoye Shosse, 65, 196140, Russia*

¹²*Fesenkov Astrophysical Institute, Observatory, 23, Almaty, 050020, Kazakhstan*

¹³*American Association of Variable Star Observers, 49 Bay State Road, Cambridge, MA 02138, USA*

¹⁴*Department of Physics, Lehigh University, 16 Memorial Drive East, Bethlehem, PA 18015, USA*

¹⁵*Center for Astrophysics | Harvard & Smithsonian, 60 Garden St, Cambridge, MA 02138, USA*

¹⁶*Gemini Observatory/NSF's NOIRLab, 670 N. A'ohoku Place, Hilo, HI, 96720, USA*

¹⁷*Department of Physics and Astronomy, Vanderbilt University, Nashville, TN 37235, USA*

¹⁸*Department of Astronomy & Astrophysics, The Pennsylvania State University, 525 Davey Lab, University Park, PA 16802, USA*

¹⁹*Eberly Research Fellow*

²⁰*Center for Exoplanets and Habitable Worlds, The Pennsylvania State University, 525 Davey Lab, University Park, PA 16802, USA*

²¹*Abrams Planetarium, Michigan State University, East Lansing, MI, USA*

²²*Department of Astronomy and Planetary Science, Northern Arizona University, Flagstaff, AZ, 86011, USA*

²³*The College of Idaho, Caldwell, ID 83605, USA*

arXiv:2109.11026v1 [astro-ph.SR] 22 Sep 2021

Accepted XXX. Received YYY; in original form ZZZ

ABSTRACT

The bright and understudied classical Be star HD 6226 has exhibited multiple outbursts in the last several years during which the star grew a viscous decretion disk. We analyze 659 optical spectra of the system collected from 2017-2020, along with a UV spectrum from the *Hubble Space Telescope* and high cadence photometry from both *TESS* and the KELT survey. We find that the star has a spectral type of B2.5IIIe, with a rotation rate of 74% of critical. The star is nearly pole-on with an inclination of $13^\circ.4$. We confirm the spectroscopic pulsational properties previously reported, and report on three photometric oscillations from KELT photometry. The outbursting behavior is studied with equivalent width measurements of $H\alpha$ and $H\beta$, and the variations in both of these can be quantitatively explained with two frequencies through a Fourier analysis. One of the frequencies for the emission outbursts is equal to the difference between two photometric oscillations, linking these pulsation modes to the mass ejection mechanism for some outbursts. During the *TESS* observation time period of 2019 October 7 to 2019 November 2, the star was building a disk. With a large dataset of $H\alpha$ and $H\beta$ spectroscopy, we are able to determine the timescales of dissipation in both of these lines, similar to past work on Be stars that has been done with optical photometry. HD 6226 is an ideal target with which to study the Be disk-evolution given its apparent periodic nature, allowing for targeted observations with other facilities in the future.

Key words: stars: emission-line, Be – stars: circumstellar matter – stars: early-type – stars: oscillations – stars: individual: HD 6226 – stars: rotation

1 INTRODUCTION

Classical Be stars are non-supergiant B stars that are rotating at nearly critical rates (Rivinius et al. 2003). The rapid rotation, perhaps coupled with other triggers such as pulsations or binarity, causes the formation of equatorial decretion disks. These disks are seen in hydrogen emission lines (the ‘e’ in Be) and sometimes other spectral lines, free-free excess emission in the infrared and radio, and through polarization of the continuum light (see review in Rivinius et al. 2013). Long-baseline interferometry has verified the disk hypothesis and shown that the disk material rotates in a Keplerian manner (e.g., Kraus et al. 2012). The Be phenomenon tends to peak near the early-type B stars (McSwain & Gies 2005) although this may be in part due to the observational biases where the observables of later type Be stars are harder to observe, (e.g., Shokry et al. 2018; Vieira et al. 2017).

Amongst the Be stars, the under-studied HD 6226 (V442 And, BD+46 245, SAO 36891) is the target of this study. It was noticed by Bozic & Harmanec (1998) that the photometry of the star showed semi-regular outbursts, and HD 6226 was one of the first Be stars predicted to be a Be star from its photometric behavior. They suspected that the star was a previously unrecognized Be star. The outbursts differed from one cycle to another, but a time-series of the times of maximum light hinted at quasi-regular outbursts for the system. In the year 2000, $H\alpha$ emission was detected that verified the Be nature of the system, indicating an outburst period of ~ 600 d (Božić et al. 2004). During most of this photometric cycle, the star was observed in a low-state with little variability followed by outbursts of variable duration and amplitude.

Božić et al. (2004) also analyzed a collection of 35 spectra of HD 6226 taken over a span of ~ 6 years to further constrain the nature of the variability. The emission profile for $H\alpha$ was typically double-peaked during the outbursts, although the strength varied greatly. The outbursts can last for weeks or months, but each outburst has a different behavior compared to previous emission episodes. During most of the photometric cycle, the star is in a low-state with little variability followed by outbursts of variable duration and amplitude.

However, Gandet (2019) showed a blue spectrum obtained shortly after the end of the data analyzed by Božić et al. (2004), taken during a time period where there should be no emission with their derived 600-d period, and this spectrum shows clear $H\beta$ emission from a disk. Similarly, Šlechta & Škoda (2005) found $H\alpha$ emission at a time when it was predicted to be absent by Božić et al. (2004).

In addition to these disk variations, the star’s photospheric absorption profiles for He I and metal lines shifted in radial velocity with a strict period of 2.615 d (Božić et al. 2004). The period was phased accurately over the course of > 6 years, and recent spectra (Section 4) verify the periodicity in the position of the line center. This period is similar to that of the pulsations observed in the slowly pulsating B stars (see, e.g., Aerts et al. 2010). Božić et al. (2004) considered this to be a rotational property of the star, despite its similarity to pulsational behavior of other Be stars.

It has been shown that the variability of HD 6226 bears similarities to the outbursting Be star ω CMa (28 CMa) and μ Centaurii. μ Cen was the first Be star where pulsations were a reasonable explanation for the disk outbursts (Rivinius et al. 1998). In the cases of ω CMa (Ghoreyshi et al. 2018) and λ Eri (Mennickent et al. 1998), the outbursts have been able to be predicted through photometry, and the stars show line profile variations similar to those observed in the spectrum of HD 6226 (Božić et al. 2004). One specific outburst of ω CMa was monitored with photometry during the dissipation of the disk. Models of the dissipation using HDUST and the viscous decretion disk model (Lee et al. 1991; Carciofi 2011) provided the first ever measurement of the viscosity parameter in the disk, $\alpha = 1$, and a disk mass injection rate of $\dot{M} = (3.5 \pm 1.3) \times 10^{-8} M_\odot \text{ yr}^{-1}$ (Carciofi et al. 2012). The mass injection rate is also an order of magnitude above the mass loss rate of the wind. More work was done on ω CMa by Ghoreyshi et al. (2018), who analyzed the photometric behavior over a period of nearly 40 years. They found that each outburst lasts for many years and that the outbursts do not seem to be periodic. They also found that the viscosity parameter, α varies from 0.1 to 1.0.

In 2017 August, amateur spectroscopists noted new $H\alpha$ emission in spectra of HD 6226. This prompted us to begin an intensive observing campaign that incorporates a large collection of optical spectra, *TESS* photometry, and the first high-quality ultraviolet spectrum of the star.

* E-mail: noel.richardson@erau.edu

These observations are detailed in Section 2. In Section 3, we discuss the fundamental parameters of the star from the optical and UV spectroscopy, along with a model fit to a disk-free optical spectrum and the ultraviolet spectral energy distribution. Section 4 details the pulsational mode seen in the optical spectroscopy as well as photometric oscillations from ground-based photometry. Section 5 details the star’s outbursting properties, while Section 6 presents our analysis of the *TESS* data that were serendipitously taken while the star was building a disk. Section 7 discusses our results and we conclude this study in Section 8.

2 OBSERVATIONS

2.1 Optical Spectroscopy

We collected many optical spectra that are archived in the BeSS archive¹ (Neiner et al. 2011). These spectra had moderate to high spectral resolving power ($R \sim 7,000 - 25,000$), and spanned the time between 2017 January and 2020 March. While some studies (e.g., Wisniewski et al. 2010) have found offsets between differing resolutions of spectroscopy for measurements such as the equivalent width of lines, we find that these data provide measurements similar to each other if the resolving power was greater than ~ 5000 . Thus, we rejected lower resolution spectra from the BeSS archive for this reason. All spectroscopic data were reduced using standard techniques, with corrections for bias, dark, and flats being taken into account. We note that more than half of the spectra we obtained from the BeSS archive were taken with the eshel spectrograph², which is an echelle spectrograph manufactured by the Shelyak company. We utilize these spectra for studying the pulsational properties of the star as they have uniform resolution and wavelength coverage for different observers and locations.

In addition to the BeSS archive, we obtained some data from facilities within our collaboration, including the 1-m telescope at Ritter Observatory (Toledo, Ohio, USA), the 0.8-m telescope at the Three College Observatory (North Carolina, USA), the 0.3-m telescope Reynolds Observatory (Potsdam, New York, USA), and the 3.5-m telescope at Apache Point Observatory (Sunspot, New Mexico, USA). All these data were reduced with standard techniques employing use of biases, darks (when needed), flats, and comparison lamp spectra. All spectroscopic data utilized in this project are summarized in Table 1 that lists the observer/observatory with the telescope aperture, the number of spectra and the resolving power of these data, as well as the HJDs of the time-series.

All spectroscopic data were normalized to the local continuum consistently around features of interest, and $H\alpha$ spectra were corrected for telluric contamination by means of division by a telluric template from the atlas given by Hinkle et al. (2000). We analyzed 659 $H\alpha$ spectra, 363 $H\beta$ spectra, 372 spectra covering the He I 4471 and Mg II 4481 lines, 374 spectra covering the He I 4713 line, 362 spectra covering the He I 4921 line, and 369 spectra covering the He I 5876 line.

2.2 Ultraviolet Spectroscopy with HST

We obtained an ultraviolet spectrum of HD 6226 with the *Hubble Space Telescope* and the Space Telescope Imaging Spectrograph

(STIS) on 2018 March 5 over the course of two consecutive orbits. We used the E230M and E140M gratings to cover the range of 1150–3000Å with a spectral resolving power of at least 40,000 (Kimble et al. 1998). The 0.2×0.05ND slit was used to obtain the spectra as the object is too bright to observe without a neutral density filter. The first orbit consisted of two E230M observations, with exposures of 572 s with the central wavelength of 2707Å, and an exposure of 862 s centered at 1978Å. The second orbit used the E140M mode, centered at 1425Å, and we exposed for 2919 s. Overall, the data are of high quality, with a typical signal-to-noise ratio of 15–20 per resolution element for most of the spectrum. The FUV channel had a higher signal-to-noise ratio than that of the NUV channels, allowing for stellar classification using the methods of Rountree & Sonneborn (1991, 1993).

2.3 KELT and KWS photometry

The Kilodegree Extremely Little Telescope (KELT) is a photometric survey using two small-aperture (42 mm) widefield ($26^\circ \times 26^\circ$) telescopes, with a northern location at Winer Observatory in Arizona in the United States, and a southern location at the South African Astronomical Observatory near Sutherland, South Africa. The KELT survey covers over 60% of the sky and is designed to detect transiting exoplanets around stars in the magnitude range $8 < V < 10$, but obtains photometry for stars between $7 < V < 13$. Labadie-Bartz et al. (2017) included HD 6226 (V442 And) in their survey of light curves of Be stars. We utilized these data, as well as some newer observations. These data are reduced with the same techniques as Labadie-Bartz et al. (2017), using the techniques described in detail by Pepper et al. (2007, 2012). The KELT pipeline produces both raw and detrended versions of the light curves. The detrending process is built into the KELT pipeline, and uses the Trend Filtering Algorithm (TFA) (Kovács et al. 2005) as implemented in the VAR-TOOLS package described by Hartman (2012). We used these data in our pulsational analysis after removing outliers and subtracting long-term trends on scales of more than 6-days.

We also use some lower-precision photometry taken with the Kamogata/Kiso/Kyoto Wide-field Survey (KWS)³. These data were taken in *V*-band, and have a typical error listed of 0.008 mag, but subsequent exposures show differences of ~ 0.02 mag. This discrepancy in the errors and subsequent exposure measurements led us to only use these data for qualitative purposes in Section 7.

2.4 TESS photometry

The *Transiting Exoplanet Survey Satellite* (*TESS*, Ricker et al. 2016) observed HD 6226 (TIC 196501216) for 25.02 days with a two-minute cadence. The resulting light curve contains 18,012 points taken during the satellite’s Sector 17 campaign (2019 October 7–2019 November 2). We utilized the light curve reduced and available from MAST for the pulsational analysis, which included data taken with a 2-minute cadence. We also use the available full-frame images, which contains long-term trends for the analysis of the disk and represent a 30-minute cadence for the time-series.

Jenkins et al. (2016) describe the *TESS* science processing operations centre (SPOC) pipeline that produces the 2-min light curves. We downloaded these 2-min data and used ‘PDCSAP’ flux, which generally produces smooth light curves without any large drifts in

¹ <http://basebe.obspm.fr>

² <https://www.shelyak.com/description-eshel/?lang=en>

³ <http://kws.cetus-net.org/maehara/V5data.py>

Table 1. List of contributed spectra, in order of number of spectra. All spectra cover H α , with the datasets highlighted in bold including lines such as He I λ 5876, H β , and Mg II λ 4481 that were used in further analysis.

Observer or Observatory	N_{spectra}	HJD _{first} −2450000	HJD _{end} −2450000	Spectrograph	Aperture (m)	R
Thizy	245	7987.5452	8794.3721	eshel	0.28	11,000
Guarro Flo	76	7993.4328	8880.3072	eshel	0.40	9,000
Charbonnel	57	8315.5591	8721.6023	eshel	0.50	11,000
Li	54	8000.157	8771.038	LHIRES	0.28	18,000
Stiewing	49	8770.7	8906.6573	LHIRES	0.28	18,000
Houpert	38	8057.4159	8847.3196	LHIRES	0.28	15,000
Garde	37	7802.2705	8865.2392	eshel	0.40	11,000
Daglen	20	7777.6348	8855.6228	LHIRES	0.35	17,000
Bryssinck	20	8881.3059	8881.3059	LHIRES	0.28	9,000
Ritter Obs.	16	8176.5764	8208.5546	Low-Dispersion Spectrograph	1.00	4,300
Kreider	15	8199.3425	8887.3368	LHIRES	0.43	11,000
Fosanelli	9	7811.3601	8351.4384	LHIRES	0.30	12,000
Desnoux	9	7956.5319	8441.2923	LHIRES	0.23	14,000
Clarkson	9	7998.7549	8176.5078	LHIRES	0.30	
Bertrand	7	8051.48	8402.4273	LHIRES	0.20	15,000
Foster	7	8486.7017	8860.6762	LHIRES	0.43	13,000
Leadbeater	7	8769.3878	8816.2459	LHIRES	0.28	5,400
de Bruin	6	8017.4124	8884.2778	L200	0.28	6,200
Graham	5	8104.5126	8775.6183	LHIRES	0.30	13,000
Buil	4	7988.4413	8074.4039	eshel	0.25	11,000
Buil	4	8011.5289	8767.4588	VHIRES	0.25	39,000
Terry	4	8018.4112	8352.4009	LHIRES	0.28	13,000
Maetz	4	8718.4373	8871.3256	LHIRES	0.21	12,000
Halsey	4	8784.5018	8868.3617	LHIRES	0.23	12,000
Three College Obs.	3	8134.5832	8193.5283	eshel	0.81	11,000
de Bruin	3	8818.4372	8865.307	L200	0.28	18,000
Lester	1	7770.5334		LHIRES	0.31	8,700
Apache Point Obs.	1	8175.5618		ARCES	3.50	38,000
Ubaud	1	8358.6368		LHIRES	0.28	19,000
Broussat	1	8373.4894		LHIRES	0.23	13,000
Gurney	1	8441.4463		LHIRES	0.25	13,000
Somogyi	1	8818.3911		LHIRES	0.30	18,000
Dumont	1	8848.3183		LHIRES	0.50	24,000
Dull	1	8880.3072		LHIRES	0.35	16,000

flux from systematic effects on the detector. We performed no additional processing on these light curves. We also note that these data were taken during a time when the star had a changing disk, and the long-term trends that are likely associated with the outbursts (e.g., [Božić et al. 2004](#)) are therefore removed from this light curve, but variability on the time scales of a few days remains intact.

3 FUNDAMENTAL PARAMETERS OF HD 6226

3.1 Spectral classification in the ultraviolet and optical

One of our goals for the ultraviolet observations with *HST* was to ensure that the stellar parameters were correctly measured, including the spectral type. This is especially important for Be stars, where the disk can contaminate the flux and change line ratios, or introduce emission in some lines, altering the measured spectral type. We anticipate that even though Balmer emission was present at the time of our *HST* observations, the disk has minimal effect at these shorter wavelengths.

Ultraviolet spectroscopic classification for B stars is described in detail by [Rountree & Sonneborn \(1991, 1993\)](#). Ultraviolet classification is done for B stars in the range of 1200–1900Å. The main lines used in UV classification, include He II λ 1640, C III λ 1247, C IV $\lambda\lambda$

1548,1551, N III $\lambda\lambda$ 1748,1751, N IV λ 1718, Al III $\lambda\lambda$ 1854,1863, Si II $\lambda\lambda$ 1264,1310, Si III λ 1300, Si IV $\lambda\lambda$ 1393,1402, and Fe II $\lambda\lambda$ 1600–1610. All these lines are included in the *HST* spectrum, with sufficient signal-to-noise to permit easy detection of lines if they are present.

This portion of the ultraviolet spectrum between 1200–1900Å, shown in Figure 1, has some important features. He II λ 1640 is very weak, with N III λ 1748–1751 and N IV λ 1718 absent. Si II λ 1264 is stronger than C III λ 1247, with Si II λ 1310 weaker than Si III λ 1300. These features are consistent with a B2.5 spectral type. The presence of C IV $\lambda\lambda$ 1548, 1551 in the spectrum indicates a luminosity class III. We also show in Fig. 1 a comparison of the *HST* ultraviolet spectrum with that of the B2.5III standard star π^2 Cyg from the work of [Lesh \(1968\)](#) and [Rountree & Sonneborn \(1993\)](#). The spectrum of HD 6226 appears to be very similar to that of the standard star with the major classification lines matching quite well.

The MiMeS survey ([Wade et al. 2016](#)) observed a large number of O and B stars searching for magnetic fields through optical spectropolarimetry with the ESPaDOnS spectrograph on the CFHT⁴. HD 6226

⁴ The ESPaDOnS data were downloaded from the Polarbase archive ([Donati et al. 1997](#); [Petit et al. 2014](#)), <http://polarbase.irap.omp.eu/>

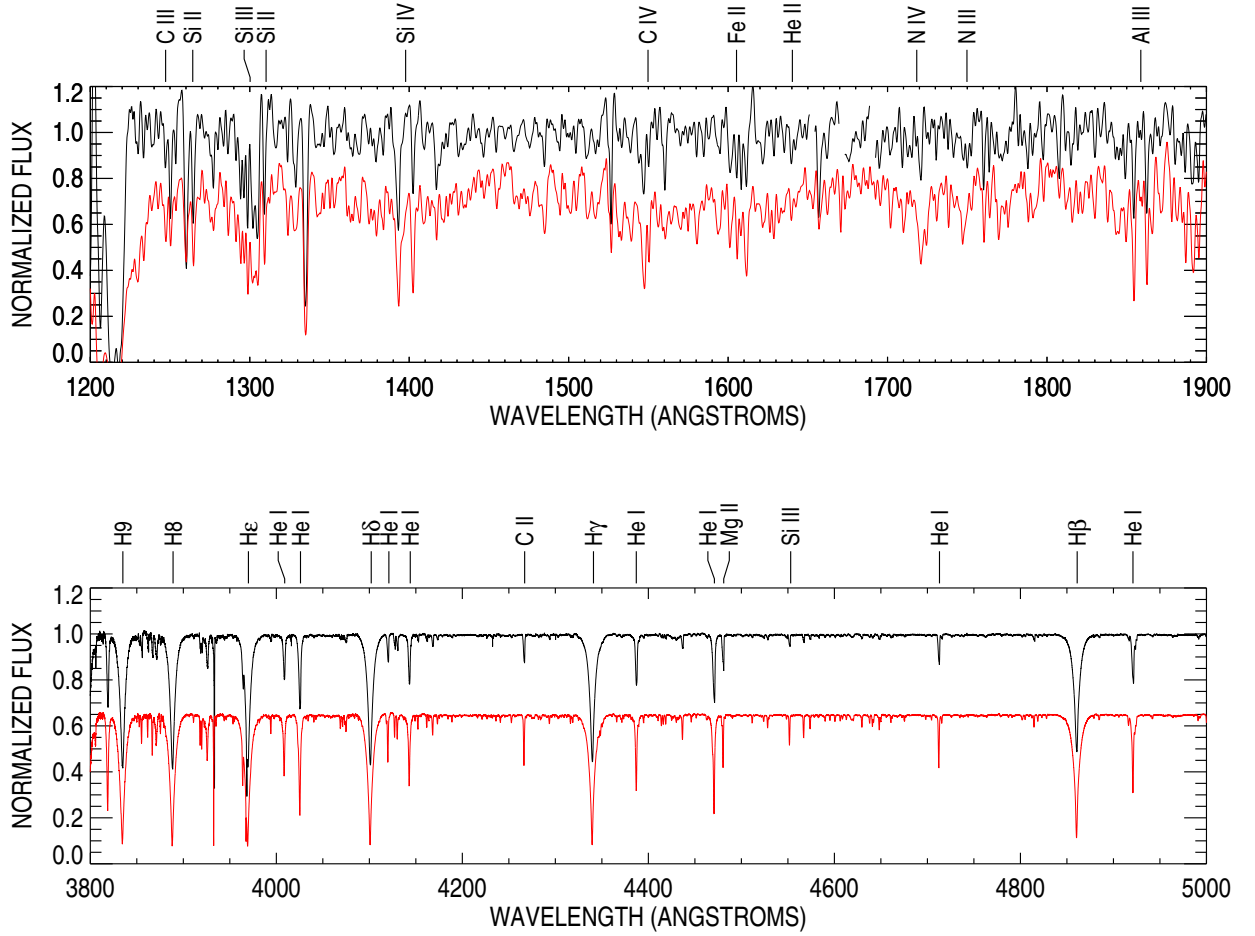


Figure 1. A comparison of the spectrum of HD 6226 (black spectrum, top) and the spectral standard star π^2 Cyg (red spectrum, bottom). The UV spectrum of HD 6226 is from our *HST* program, while the spectrum of π^2 Cyg was obtained from the *IUE* archive. The *HST* data were smoothed to the resolution of the *IUE* data. The optical spectra were taken with the ESPaDOnS spectrograph on the CFHT, and from the archive. The optical spectrum showed no signature of H α or any other Balmer emission. Observations have been smoothed for clarity in the figure. We shifted the spectrum of π^2 Cyg to match the radial velocity of HD 6226.

was included in the sample, and the spectrum from 2011 June 17 shows no obvious signs of Balmer emission (see Fig. 1). We assume that the star was disk-free at the time of the ESPaDOnS observation, although we have no photometric record around that time period. The Stokes *I* spectrum from this observation was very high quality, with a signal to noise ratio of several hundred in the continuum. The ESPaDOnS archive also contained a spectrum of the standard star π^2 Cyg. The spectra of the two stars are indistinguishable in the Balmer lines. The He I and metal lines matched in ratio, but the lines of π^2 Cyg are narrower and deeper than the lines of HD 6226. This is consistent with the previous observations of Božić et al. (2004) showing that the projected rotational velocity $v \sin i$ of HD 6226 is 70 km s^{-1} , while the results of Abt et al. (2002) show that π^2 Cyg has a $v \sin i$ of 35 km s^{-1} . While optical classification of Be stars can be difficult given possible disk contamination, it seems that the quiescent optical

spectrum of HD 6226 yields a classification that is consistent with that from the ultraviolet spectroscopy.

3.2 The Ultraviolet SED and underlying parameters

The ultraviolet portion of the spectral energy distribution is not affected by the free-bound and free-free emission that causes the infrared excess observed in Be stars. Thus, the UV SED, as measured with our *HST* observations, and the optical line profiles in the absence of emission, can be used to determine the stellar parameters. We used the BEATLAS Markov Chain Monte Carlo (MCMC) method, described in Mota et al. (in prep) and Mota (2019). BEATLAS consists of a grid of thousands of radiative transfer models for Be stars, calculated with the HDUST code (Carciofi & Bjorkman 2006, 2008), that covers the range of stellar parameters relevant to the Be phenomenon (i.e., spectral subclasses O9 to A0). To explore the grid and sample the

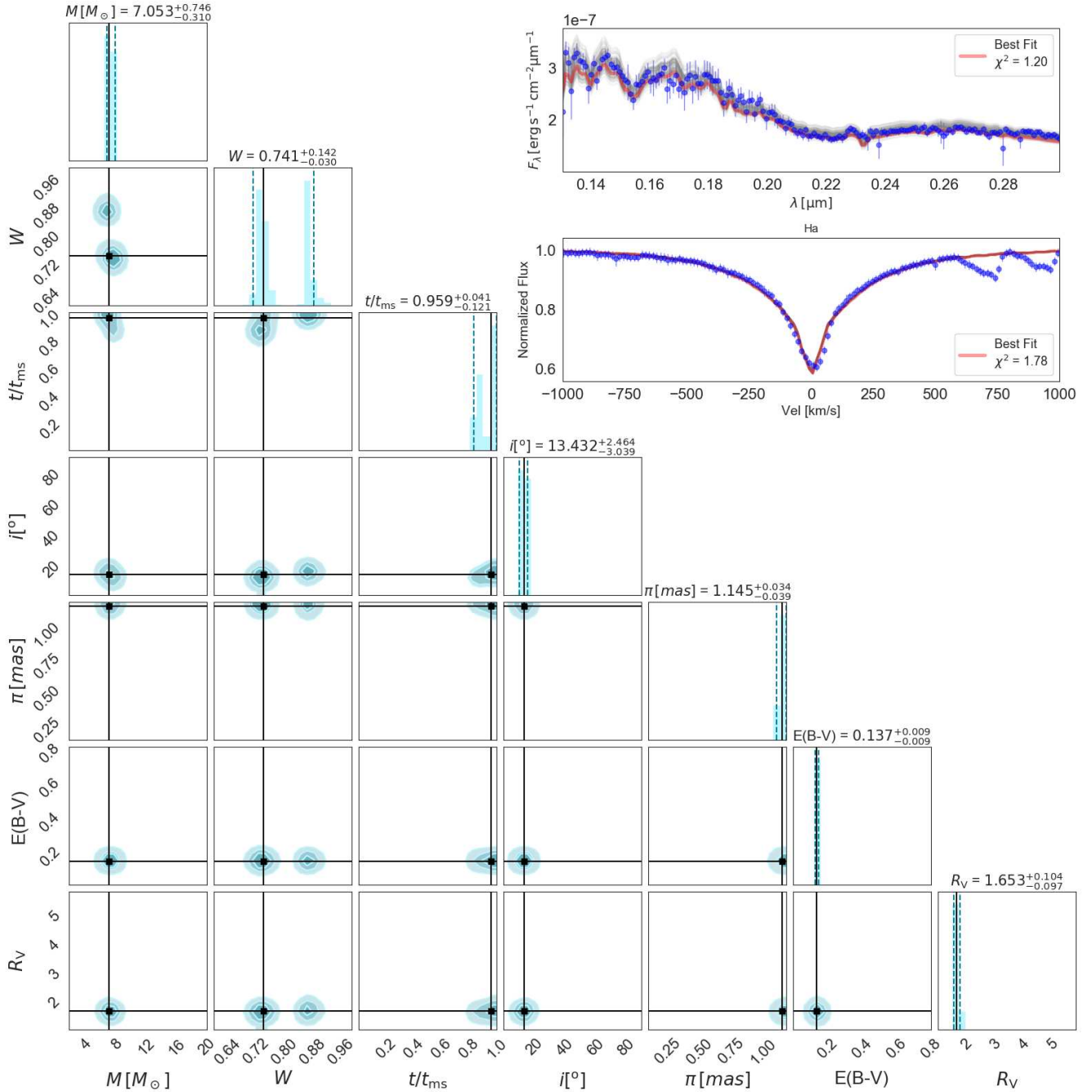


Figure 2. Corner plot for a MCMC simulation of HD 6226. The main diagonal shows the probability density function for each fitted parameter (see text for details). The vertical dashed lines mark the limits of the HDR, while the solid black line is the mean value in the region, and the most likely value for each parameter. The off-diagonal plots indicate the two-on-two correlations of the probabilities. The inset shows the UV SED (upper part) and H α spectrum (bottom part). The data are shown as the blue points with error bars. The red line represents the model obtained from the most likely values for each of the parameters, and the grey lines in the SED panel are the models proposed in the last position of each of the walkers in the BEATLAS simulation. Note that the model is only used to calculate the hydrogen lines, so the C II doublet is not modeled in the shown profile.

parameter space, the python implementation of the affine-invariant MCMC ensemble sampler of [Goodman & Weare \(2010\)](#), *emcee*, is used. Using the Monte Carlo approach has the distinct advantage of providing us not just a best fit model, but rather a probability density function for each of the parameters, and the correlations between them, which makes a more statistically robust inference for the derived parameters.

The BEATLAS simulation takes as input the grid of models, the observational data for the star and whatever prior information is available in the literature. As input data, we use the ultraviolet *HST* observation described in Section 2.2, and the archival ESPaDOnS H α line profile, which was made when the star had no signs of a disk in the optical Balmer profiles. As prior information, we use the Gaia DR2 parallax ([Gaia Collaboration et al. 2018](#)) of $\pi = 0.639 \pm 0.077$ mas.

The stellar parameters covered in BEATLAS are the mass, M_{star} , the inclination angle of the star’s spin axis with respect to the line of sight, i , the rotation rate, $W = \frac{v \sin i}{v_{\text{orb}}}$, as defined in Rivinius et al. (2013), and the fractional age of the star in units of main sequence lifetime (t/t_{MS}). In addition to these, fitted parameters are the parallax, π , and two parameters that define the interstellar reddening, namely $E(B - V)$ and the total-to-selective extinction ratio, R_V . We note that the $E(B - V)$ and R_V parameters could be slightly contaminated by circumstellar disk that was present at the time of the ultraviolet observations, based on our H α and H β analysis (Section 5). The code also derives values for the equatorial and polar radii as well as the gravity darkening exponent β (originally defined by von Zeipel 1924). Other parameters needed for the BEATLAS HDUST runs (e.g., R_{star}) are calculated using the Geneva grid of models for fast spinning stars (Georgy et al. 2013a).

The simulation was run with 300 walkers and 5000 steps, and had an acceptance fraction of 0.33, which is within the range defined by Foreman-Mackey et al. (2013) for examining the parameter space that will describe the stellar parameters. The walkers represent the number of separate models exploring parameter space during the Monte Carlo run, whereas the steps are the number of iterations that each walker takes during the process. The results are shown in Fig. 2 and the outcome is summarized in Table 2. We define the uncertainty range in the determination of each parameter as the range of the highest density (or probability) region (HDR) of each probability density function (PDF) that contains 68% of the density. The most likely (or “best fit”) value for each parameter is represented by the mean of the HDR.

Both the ultraviolet SED and the H α line profile are fit well by the models. The $E(B - V)$ parameter is quite well constrained by the 2200Å band associated with interstellar matter (Cardelli et al. 1989). The high uncertainties in W are explained by the double-peaked shape of the PDF, which indicates that while the highest probability lies around the values of 0.74, but a much larger value for W cannot be excluded. The star is seen at an almost pole-on orientation ($i = 13.4^{+2.5}_{-3.0}$ °). The estimated value for $v \sin i = 57^{+42}_{-18}$ km s $^{-1}$ is in agreement with the value of 70 km s $^{-1}$ of Božić et al. (2004).

The inferred parallax is about 50% larger (about 4σ), than the Gaia DR2 value. To investigate this issue we performed two other BEATLAS simulations, one without the parallax prior, another two forcing the parallax to lie within 1σ of the Gaia DR2 or EDR3 values. In the first of these simulations, our results are very similar to those of our derived model using the Gaia parallax, with a slightly different mass ($7.3M_{\odot}$), and a similar goodness of fit. In the second model, the derived mass is then much larger ($10.3M_{\odot}$), but the quality of the fit is much poorer, as the reduced χ^2 is increased by roughly a factor of 3 for the UV SED, and about a factor of 1.5 for the H α line. Finally, in a third model, we also use the newer Gaia EDR3 parallax as a prior. This model suffered from unrealistic values of W and $v \sin i$. Since we see that the value for $v \sin i$ must be higher than that of the spectral standard π^2 Cyg (Section 3.1), the derived value of 26 km s $^{-1}$ from the third model led us to adopt the model that has a free parallax and has a distance consistent with the Gaia DR2 measurement. The inconsistencies from these models seem to lie with the Gaia parallax, which may be explained with an unresolved binary companion in the system. If the orbital inclination of a binary companion is similar to the rotational inclination, $\sim 13^\circ$, then we suspect that any orbital-related photometric or spectroscopic variations would be too small to detect.

We note that Božić et al. (2004) did find a ~ 25 d period that could

Parameter	Value	Type
$M [M_{\odot}]$	$7.05^{+0.75}_{-0.31}$	Free
W	$0.74^{+0.14}_{-0.03}$	Free
t/t_{ms}	$0.96^{+0.04}_{-0.12}$	Free
$i [^\circ]$	$13.4^{+2.5}_{-3.0}$	Free
$\pi [mas]$	$1.14^{+0.03}_{-0.04}$	Free
$E(B-V)$	$0.14^{+0.01}_{-0.01}$	Free
R_V	$1.65^{+0.10}_{-0.10}$	Free
R_{eq}/R_p	$1.27^{+0.12}_{-0.02}$	Derived
$R_{\text{eq}} [R_{\odot}]$	$7.4^{+1.3}_{-1.1}$	Derived
$\log(L) [L_{\odot}]$	$3.58^{+0.19}_{-0.17}$	Derived
$\log(g) [cgs]$	$3.55^{+0.18}_{-0.17}$	Derived
β	$0.18^{+0.00}_{-0.02}$	Derived
$v \sin i [km/s]$	57^{+42}_{-18}	Derived
$T_{\text{eff}} [K]$	17000^{+3500}_{-2600}	Derived

Table 2. Fitted and derived parameters for HD 6226 using the BEATLAS MCMC sampler.

be associated with such a binary, but their data were too scarce to make a strong statement about the cause of that periodicity. Many Be stars are thought to have a stripped star companion, such as the case of ϕ Per (Gies et al. 1998; Mourard et al. 2015) and several other Be stars (see, e.g., Wang et al. 2018, and references therein). If the putative binary companion is a stripped star, then its luminosity would be much smaller than that of the Be star, and it would not influence our analysis of the UV spectrum. However, if the companion were a main-sequence star of comparable mass to HD 6226, it could help reconcile the UV spectrum with the Gaia distance. The presence of a companion star may cause additional uncertainty in the derived parameters such the main-sequence lifetime.

The proper motion of HD 6226, combined with the high radial velocity of the star makes the star a runaway star according to Boubert & Evans (2018). It is situated well out of the plane of the Galaxy, and the mean radial velocity indicates that it is on its way back to the plane. We used the GaLPy package (Bovy 2015) and the Gaia proper motion to estimate the time of flight since ejection from the disk. Using a mean radial velocity of -55 km s $^{-1}$, the result is a time of flight of 31 Myrs which compares to the evolutionary age of 51 Myrs for a $7M_{\odot}$ model from Georgy et al. (2013b). It may be a star that was spun up by binary mass transfer and then ejected when the companion experienced a supernova explosion. Many OB runaways are indeed rapid rotators that have experienced spin up. In that case, HD 6226 may have been rejuvenated by mass transfer, and the current age estimate corresponds to the time since mass transfer was completed.

4 PULSATIONAL PROPERTIES

Božić et al. (2004) found that HD 6226 had a spectroscopic variability signature with a period of 2.61507 ± 0.00013 days, which they interpreted as the rotational period. They found some evidence of line profile variations with a period of $\sim 24 - 29$ d in the He I $\lambda 6678$ transition, but they did not have sufficient spectral cadence to document adequately such long timescale variability.

We confirmed this spectroscopic signature of pulsations with our time-series spectroscopy, concentrating on data taken with eshel spectrographs for consistency between the different observational setups. We considered the lines of He I $\lambda 4471$, 4713, 4921, and 5876, along with Mg II $\lambda 4481$. We chose these lines as they had

reasonable signal-to-noise ratios ($S/N \sim 100$ per resolution element), and were sufficiently far from the edge of the orders. By limiting our analysis to the eshel data, we had more than 350 observations per line. There is evidence of similar variations in the hydrogen lines (see, e.g., Figs. 5 and 8 for a dynamical representation of the data during the *TESS* observation time frame), but the frequent contamination by the disk emission prevented us from analyzing the exact behavior. The behavior is similar to that of the pulsating Be stars discussed by Rivinius et al. (2003), and we interpret these variations in that context here.

We performed a cross-correlation of our spectra against a template line profile from the TLUSTY BSTAR2006 grid (Lanz & Hubeny 2007) using the parameters of $T_{\text{eff}} = 17,000$ K, $\log g = 3.0$, and $v \sin i = 70$ km s $^{-1}$, similar to that of Božić et al. (2004) and our modeling results. This is also consistent with fundamental parameters of other normal B giants, such as the B3III star HD 209008 that was found to have $T_{\text{eff}} = 15,800$ K by Nieva & Przybilla (2014). We used this rather than our model from Section 3, as the model in Section 3 only calculates the hydrogen line profiles. The resulting velocities are included in the Appendix. Many of these lines were used by Rivinius et al. (2003), allowing us to qualitatively compare our results to that of other Be stars.

We calculated Fourier amplitude spectra (Fig. 3) for the radial velocity of each spectral line with the Period04 software (Lenz & Breger 2005). In Fig. 3, we show the Fourier amplitude spectrum of the Mg II radial velocities. All lines show similar behavior in the resulting Fourier analysis, and the inset plot shows the resulting peak frequency, which is common for all lines, of 0.382332 ± 0.000026 d $^{-1}$, corresponding to a period of 2.61553 ± 0.00018 d. We note that the inset panel shows the Fourier spectrum for all line transitions, and these were combined in the derived frequency. This value is very similar to the 2.61507 ± 0.00013 d period derived by Božić et al. (2004), and the differences could be that our time-series has a shorter baseline and lower spectral resolution than that of Božić et al. (2004), but also has a larger number of spectra. Our maximum radial velocity occurs at the epoch HJD 2,458,041.67168 \pm 0.00025, which is within errors of the maximum radial velocity epoch measured by Božić et al. (2004).

Our Fourier transform spectra shown in Fig. 3 all showed several aliases of the dominant frequency due to diurnal sampling. These included frequencies of the form $n \pm f$, where n is an integer between 1 and 6. These aliases are highlighted with vertical red dashed lines. Once we fit the dominant period and subtracted the trends from the data, these aliases did not show up in Fourier amplitude spectra of the residuals. The variance of the residuals between the sinusoidal fit and the data are comparable to typical errors in the data. The amplitude of the spectral variations varied depending on the line measured. The fit parameters are given in Table 3, with the fits shown in Fig. 4.

We subtracted average line profiles of each transition from all observations and show the resulting residual variations in Fig. 4, which shows the variability of He I 5876 and Mg II 4481. The observations show a bright or dark part of the profile moving from blue to red across the profile over the period. The *TESS* photometry, which will be discussed in Section 6, also show some evidence of the pulsational period, although at lower amplitude given the redder passband of the *TESS* instrument than the KELT data. The results of the other lines were similar and are shown in the online appendix.

Overall, we suspect that this periodic line profile variation corresponds to a low-order non-radial mode. We re-examined the KELT photometry of HD 6226 (Fig. 3; Labadie-Bartz et al. 2017), and saw that there is a weak associated peak in the Fourier spectrum with an amplitude of 2.3 millimag. With such a weak associated

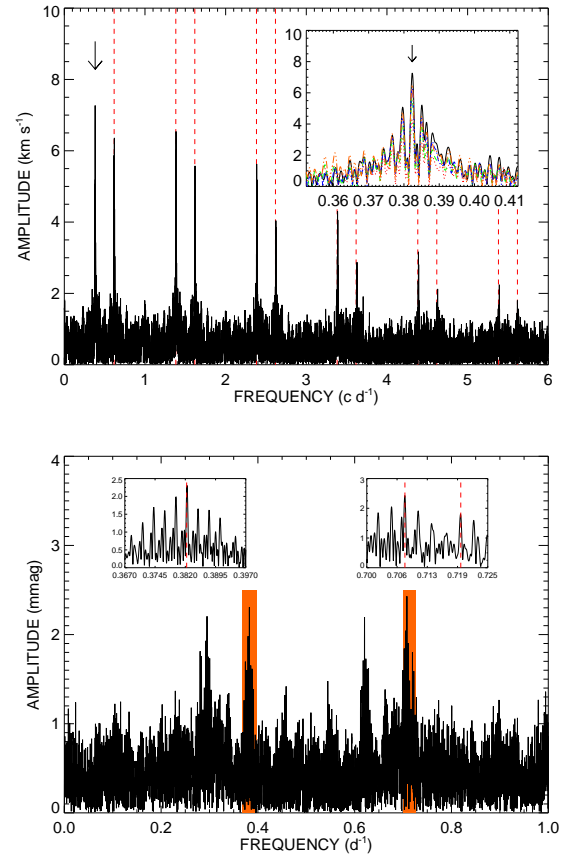


Figure 3. Fourier Amplitude spectra of radial velocity measurements of He I $\lambda\lambda 471, 4713, 4921, 5876$ (red, blue, green, and orange, respectively) and Mg II $\lambda 4481$ (black) are shown in the top panel. The dominant frequency is indicated with a large arrow, while diurnal aliases are indicated with vertical red, dashed lines. The bottom panel shows the Fourier amplitude spectrum of the KELT photometry. The orange highlighted regions represent the regions that are zoomed in for the two inset panels, where we show the derived frequencies as vertical red dashed lines. All other peaks are aliases of the derived frequencies similar to the derived frequencies from the spectroscopic measurements. The neighboring peaks for both time-series are spaced close to the expectation for 365 d, originating from the Earth-based data sets.

light variation, we suspect that it should be at least an $l = 2$ mode based on comparisons to the pulsations discussed by Rivinius et al. (2003). Qualitatively, our greyscales in Fig. 4 look similar to ω CMA that were observed by Rivinius et al. (2003). However, the case of HD 6226 provides a much longer period than in any of the Be stars studied by Rivinius et al. (2003). Given the long period, we suspect that the star is a slowly pulsating B star (SPB), and is not a pulsating β Cephei star.

The KELT data were detrended to remove variability on time-scales longer than 6 days so as to remove the outbursting trends from the data as well as any systematic effects associated with yearly or lunar cycles. We found that the frequency detected in the spectroscopic absorption lines was also seen in the photometry, with an amplitude of 2.35 millimag. The KELT data also show evidence of a pair of frequencies at 0.70786 d $^{-1}$ and 0.71936 d $^{-1}$. These correspond to periods of 1.41 and 1.39 days, with amplitudes of 2.6 mmag and 2.2 mmag. We show the Fourier transform from the KELT data in the second panel of Fig. 3. The 1.4 d timescale was also seen in the *TESS*

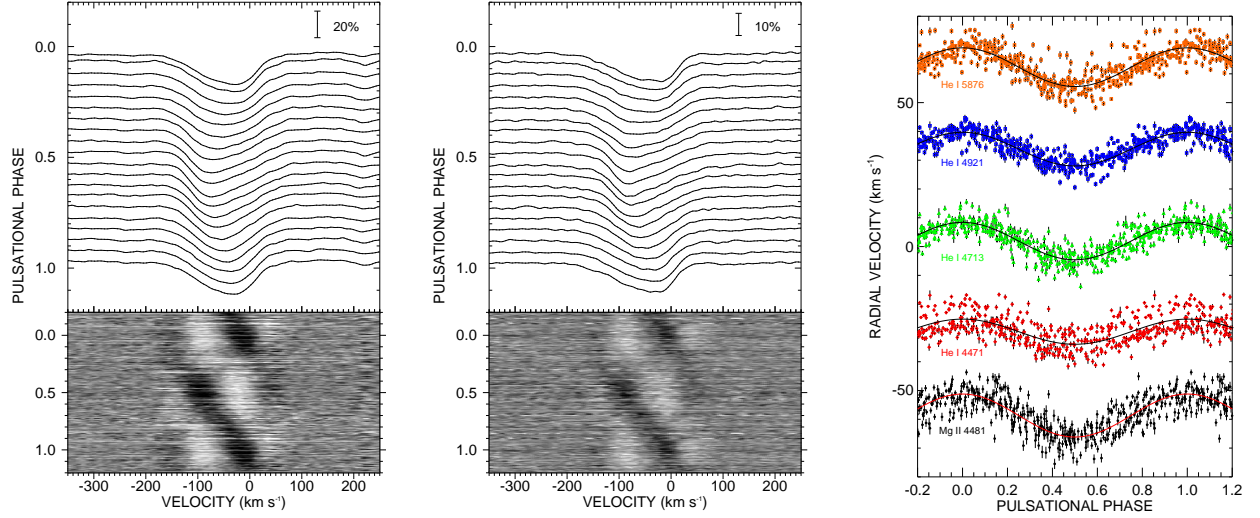


Figure 4. Dynamical representation of HD 6226 He I λ 5876 (left) and Mg II λ 4481 (center) spectra during our campaign phased on the 2.6 d pulsational period. The grey scales show the differences from an average profile and the phasing is referenced in Table 3. The black/white contrast indicates a $\pm 4\%$ deviation in each plot. The depth of the individual line profiles is shown in continuum units in each panel. Each shown line profile represents an average of all observations in a 0.05 phase interval. Representations of the He I λ 4471, 4713, 4921 profiles are shown in the Appendix. On the right panel, we show the radial velocity of the absorption lines measured (Mg II (black), He I 4471 (red), He I 4713 (green), He I 4921 (blue), and He I 5876 (orange)). Each point was measured via cross correlation with a TLUSTY stellar atmosphere model with similar stellar parameters. Measurements are offset for clarity and color coded. All measurements are phased to the same reference time and period.

Table 3. Derived pulsational frequencies from spectroscopic and photometric measurements

Line	Frequency (c d^{-1})	Period (d)	Amplitude (km s^{-1})	V_0 (km s^{-1})	r.m.s. (km s^{-1})	$N_{\text{measurements}}$
He I 4471	0.382313(36)	2.61566	4.36(33)	-59.6	4.00	372
He I 4713	0.382325(20)	2.61557	6.49(22)	-58.1	3.07	374
He I 4921	0.382310(18)	2.61568	5.84(21)	-56.2	2.52	362
He I 5876	0.382342(21)	2.61546	6.72(25)	-57.7	3.50	369
Mg II 4481	0.382368(22)	2.61528	7.46(32)	-58.7	3.99	372
Combined	0.382332(26)	2.61553(18)
Božić et al. (2004)	0.38240(02)	2.61507(13)	35
Photometric Band	Frequency (c d^{-1})	Period (d)	Amplitude (mmag)			
KELT ($\sim R$)	0.38243(21)	2.6149(47)	2.35			
KELT ($\sim R$)	0.70787(21)	1.41269(42)	2.61			
KELT ($\sim R$)	0.71940(26)	1.39013(50)	2.16			

data, but the period varied over the time of the *TESS* data, which we discuss in terms of the outbursting disk in Section 6.

There are three detected pulsational modes between the analysis of the spectroscopy and the KELT photometry. These modes are consistent with those of slowly pulsating B stars. Given the model presented for the Be star based on the data available in Fig. 2 and Table 2, we see that the mass is $7.1 M_{\odot}$, which is near the high end for what we expect for an SPB star (see Chapter 2 of Aerts et al. 2010). Indeed, the star would seem to lie closer to the expected instability strip for the β Cephei stars. However, Miglio et al. (2007b) find that the instability strip for SPB stars extends itself to higher luminosities and has a large overlap with the instability strip for the β Cephei stars.

We conclude that HD 6226 is a slowly pulsating B star with nar-

row lines and $P=2.6$ d. We see a higher amplitude radial velocity variation in the Mg II line than in the He I lines, and Božić et al. (2004) found that the metal lines had higher amplitude variations. We suspect that the larger amplitude of the metallic radial velocity shifts are due to the intrinsic atomic broadening in each case. Metal transitions have narrower features that create more contrasting features in the Doppler-shift distribution of the profiles. Indeed the bumps look sharper in the Mg II case in Figure 4. This results in a larger amplitude when measured using cross-correlation methods. The star also exhibits two photometric periods of $P=1.39$ and 1.41 d providing the constructive modes and episodic ejections, which will be discussed by explaining the $H\alpha$ and $H\beta$ outburst behavior in the following section.

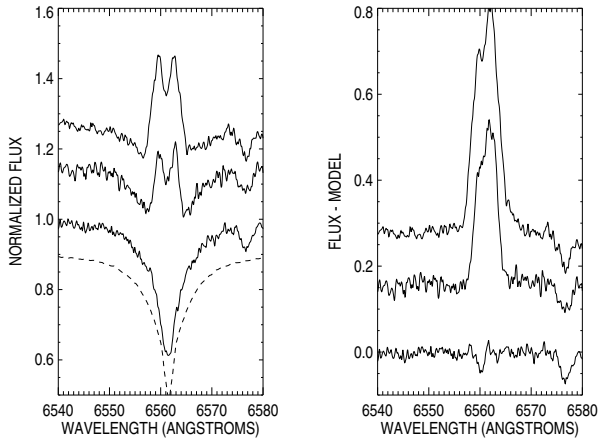


Figure 5. $H\alpha$ line profiles from the first well-observed outburst in our spectroscopic dataset, showing three representative profiles. The weak emission profile (pure absorption) on the bottom was taken on HJD 2458077.2, the moderate emission was taken during the decay phase on HJD 2458018.5, and the strong profile (top) was taken on HJD 2457999.5. The spectra are offset for clarity, and we show the model calculated in Section 3.2 as a dashed line. We subtracted the model from these profiles to obtain the profiles shown in the right panel and found the disk profiles to be single-peaked. Note that the subtracted model is only for the hydrogen line, leaving the weak C II $\lambda\lambda$ 6578,6583 absorption lines in the subtracted region.

5 SPECTROSCOPIC MEASUREMENTS OF THE OUTBURSTING DISK ACTIVITY

Be star outbursts are typically considered to be discrete events with time-scales of days to decades, representing a time when material from the star is transferred to an equatorial decretion disk, governed by gravity and viscosity. During the outburst events, the emission and polarization can change as the inner-most portions of the disk increase in density (Rivinius et al. 2003). The appearance of these outbursts depend on many system properties, including the inclination of the disk, as an edge-on disk will absorb light and cause the star to appear dimmer, whereas a nearly pole-on star will appear brighter (Sigut & Patel 2013). In the case of HD 6226, Labadie-Bartz et al. (2017) examined the star with KELT photometry, observing photometric outbursts and classifying the star as having intermediate periodicity with periodic variability with time-scales greater than 2 days. They also found outburst variability with semi-regular outbursts, and reported a period of 60.3 d.

The star went through dramatic episodes of disk building and loss through the time period of 2017–2020 (see, e.g., Fig. 6). With our extensive spectroscopic dataset, we can study these disk episodes through measurements of sensitive lines, in particular $H\alpha$ and $H\beta$.

Our study of HD 6226 truly began in late August 2017 when one of us (Thizy) observed the star was growing a disk shortly after it had been observed in a disk-less state. We began our analysis of the stellar disk with measurements of the equivalent width of the $H\alpha$ and $H\beta$ lines. In Fig. 5, we show three of the $H\alpha$ profiles from the time surrounding the first outburst from our campaign. We subtracted the model described in Section 3.2 from the profiles and found that the disk does not show double peaks. This further supports the results of Section 3.2, in that we observe the disk close to a pole-on orientation, and we then see only a small separation of the peaks observed in the raw spectra in Fig. 5.

We measured the equivalent width of the $H\alpha$ and $H\beta$ profiles, as

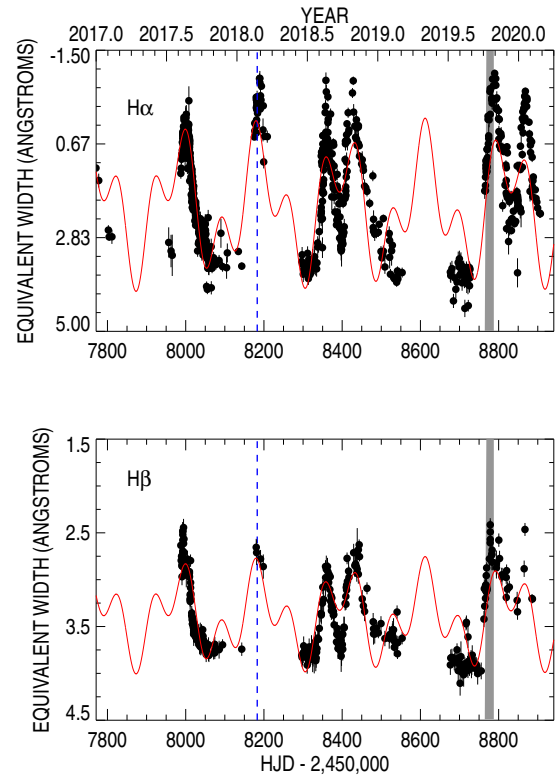


Figure 6. $H\alpha$ (top) and $H\beta$ (bottom) equivalent widths. We show the time of the *HST* observation with a vertical blue dashed line. The timing of the *TESS* observations is shown as a grey rectangular region. We overplotted our two-frequency fit to the data as a red solid line. The dashed blue line represents the epoch of the *HST* observation.

shown in Fig. 6. We tabulate these values in the Appendix online. The $H\alpha$ equivalent width shows evidence of six outbursts during the time period we examined, with some additional emission present at the time preceding our campaign. Overall, these variations are seen to be similar, but the amplitude of the $H\beta$ variability is smaller than the $H\alpha$ variations, as expected. The $H\alpha$ variations are better sampled, as more $H\alpha$ spectra exist in BeSS, but are often seen to have larger errors, which can be explained as the $H\beta$ spectra are all from eshel spectrographs, and are therefore more consistent between different observers. Errors were estimated based on the signal-to-noise ratio for the observation as well as the spectral resolution. This was done based on the derivation by Vollmann & Eversberg (2006) with the formula

$$\sigma = \frac{n\Delta\lambda - W_\lambda}{SNR}.$$

Here, σ represents the error, n is the number of data points across the region of integration, $\Delta\lambda$ is the pixel separation, W_λ is the measured equivalent width, and the SNR is the signal-to-noise per resolution element.

We analyzed the data with the same kinds of Fourier techniques used in our pulsational analysis and found evidence of two frequencies in the data. We note that Fourier analysis is not a perfect way to go about understanding the outbursts as they are inherently non-sinusoidal. For example, we know that the light curves of Be stars are often modeled to have exponential decay (e.g., Ghoreyshi et al. 2018). However, the Fourier analysis shows that the timing of the maxima and minima in the equivalent width variability can be repro-

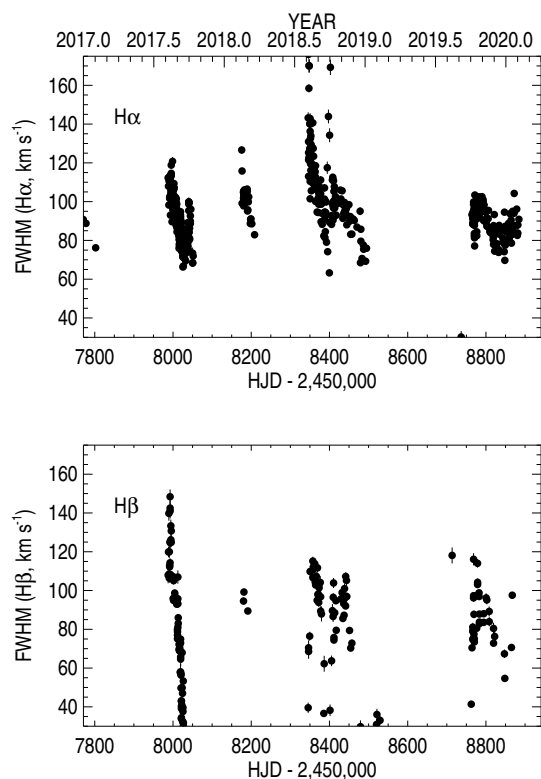


Figure 7. The FWHM of the $H\alpha$ (top) and $H\beta$ (bottom) emission features, calculated from the residual of the of the observed minus photospheric model profiles (§3.2).

duced with two periods. The details of the two found periods and the fit are given in Table 4. We note that the variable in Table 4 of $W_{\lambda 0}$ refers to the point at which the equivalent widths oscillate around, which is an “average” equivalent width, so that the variability shown in Fig. 6 can be reproduced by the equation

$$W_{\lambda} = W_{\lambda 0} + \sum_{i=0}^n A_i \sin(2\pi(f_i t + \phi_i)).$$

In this formulation, A_i is the amplitude of the particular sine wave, f_i is the frequency, t is the time, and ϕ_i is a phase introduced to shift the maxima to the correct time points. We note that there was no indication of the 2.615 d pulsational period (Section 4) in the analysis of the equivalent widths.

Be star disk lines are often analyzed with the ratio of the violet-to-red emission peak heights (V/R). With HD 6226, this is a difficult measurement to consider as the disk peak is quite narrow compared to most Be stars, likely due to a pole-on orientation. The raw profiles show a double-peaked emission, but they appear as single-peaked when the model spectrum is subtracted (see Fig. 5). In our online supplement, we show individual line profiles and dynamical representations of the data in Appendix A, along with a 3-D printable version of the first outburst in $H\alpha$ in Appendix B.

One advantage of the analysis of V/R measurements is that one can determine the radial velocity difference between the two peaks. In the case of μ Cen (Rivinius et al. 1998), the onset of a disk outburst shows a larger separation of the radial velocity of V and R peaks due to the disk material being located closest to the star at that time. As time continues during the outburst, the material moves further out, causing the velocities to lower and the peaks to move closer together.

Since we are unable to measure the V and R peaks directly, we decided to fit the residual profile resulting from subtracting the model spectrum from the individual observations. Our fit was comprised of a simple Gaussian, yielding three parameters: the central peak velocity, the peak height, and the width, which are tabulated in Appendix C. The full width at half maximum is a good proxy for the difference in the radial velocity difference between the V and R peaks as it measures the difference of the velocity between the two sides of the emission that is roughly Gaussian shaped. In order to make these measurements, we first culled our data to observations when the equivalent width was less than 2.75\AA for $H\alpha$ or less than 3.6\AA for the $H\beta$ profile so that we only measure spectra with a disk profile that is easily seen with the typical S/N of the data. The FWHM measurements are shown in Fig. 7, and we see a general decline in each of the outbursts. For the $H\beta$ observations, the data are more uniform, and we see the width becomes very narrow near the end of the outbursts. The peak height measurements show almost identical curves to the equivalent width curves, so are not shown in our plots. We estimated the errors of these measurements as the error from the fit of the Gaussian, which is likely an underestimate of the actual error.

6 TESS PHOTOMETRY

The *TESS* observations were obtained as the disk was beginning to grow according to the $H\alpha$ and $H\beta$ activity, as shown in the grey-highlighted portion of Fig. 6. This is supported by the full-frame image light curve that shows an increase in flux through the beginning part of the *TESS* observations. The flux then decreases even while the $H\alpha$ equivalent width continues to grow due to the different formation radii for the broad-band optical flux and hydrogen emission. The $H\alpha$ and $H\beta$ line profiles increase in strength throughout the time period of the *TESS* observations, and the line profile peak oscillates from being blueshifted to redshifted and back during this time-scale (Fig. 8).

We show the *TESS* light curve in the top panel of Fig. 9. The light curve shows variations with a time scale of ~ 1.4 d. The extracted 30-minute cadence light curve shows the effect of the disk growth during this time. This looks to be similar to the time scale of the shifting of the profile morphology in Fig. 8. We performed a Fourier analysis of the *TESS* photometry. In the bottom panels of Fig. 9, we show the combined Fourier transform of the entire 2-minute cadence *TESS* light curve. We divided the light curve into two halves based on the gap in coverage. The Fourier spectrum of the entire data set shows the strongest peak to be a broad feature near 0.7 d^{-1} , which is confirmed visually in the second half of the light curve. We also indicate the pulsational frequency seen spectroscopically as well as the two additional frequencies derived from the KELT data in the panels for the Fourier spectra. The KELT data were too sparse in this time period for inter-comparison.

In order to further examine the variability in the observed light curve, we took 5-day segments of the 2-minute cadence light curve and then performed a Fourier analysis on each segment. The resulting strongest peak is indicated in each of the Fourier spectra shown in Fig. 9 with a red point. The peak frequencies are plotted in the top-middle panel, where the symbol size is proportional to the amplitude of the signal. The $H\alpha$ equivalent width measurements from the same time period are also plotted for convenience, showing an increase in emission during this time.

The beginning of the *TESS* observations is dominated by a lower-amplitude signal that becomes smaller with time. As the disk reaches a maximum near the time of the *TESS* data gap (so that the satellite

Table 4. Derived Frequencies for the Equivalent Widths

Line	Frequency (c d^{-1})	Period (d)	Amplitude (\AA)	$W_{\lambda 10}$ (\AA)	phase (relative to) (HJD - 2,450,000)
H α	0.004742(19)	211.9(8)	1.157(41)	2.073(31)	0.9180(72)
H α	0.011499(29)	87.0(6)	0.845(40)	...	0.7138(83)
H β	0.004742(67)	211.9(8)	0.342(37)	3.479(35)	0.918(17)
H β	0.011499(80)	87.0(6)	0.284(37)	...	0.714(20)

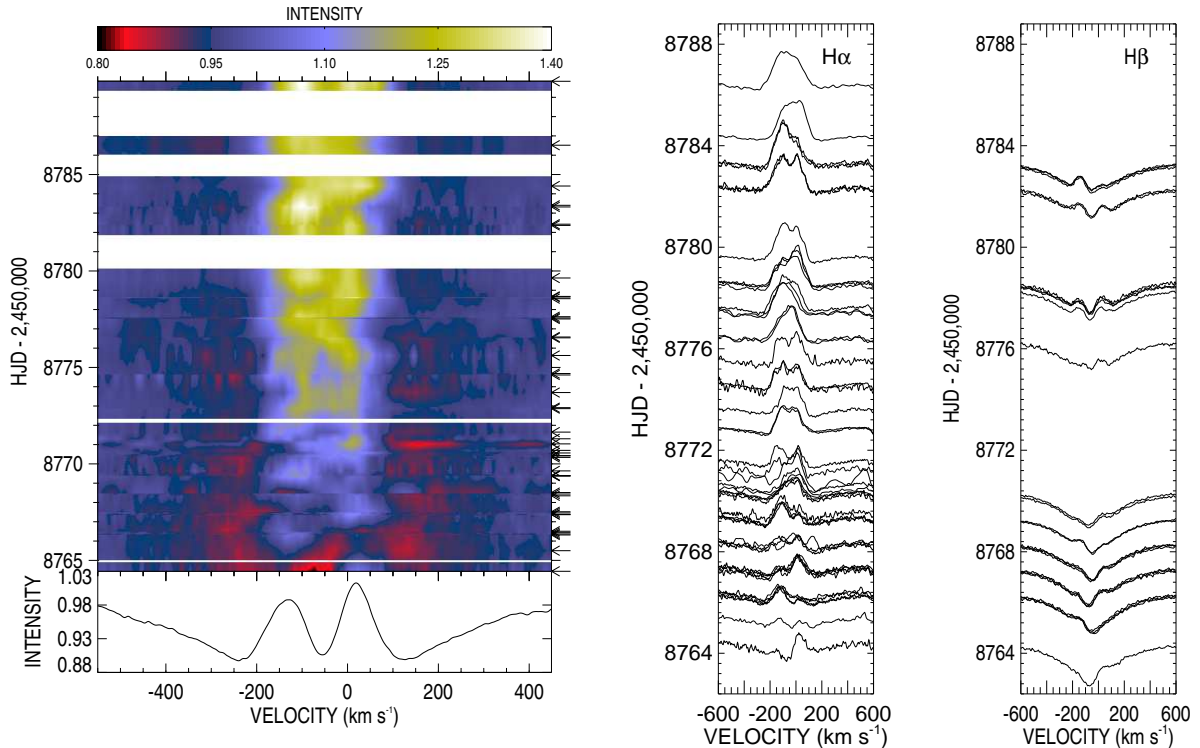


Figure 8. A dynamical representation of the H α spectra from the time of the *TESS* photometry is shown on the left, with an average profile shown in the bottom panel. On the right, we show the line profiles of H α (left panel) and H β (right panel). The time of the observations is noted on the y-axis. We note that some evidence of the pulsational signature (2.615 d) is seen in the dynamical spectrum.

can send data back to Earth), the signal became strong and then stayed roughly constant in frequency and amplitude for the remainder of the *TESS* observations. This is consistent with a constructive interference of the two KELT periods being the driving mechanism for the disk growth for the HD 6226 system.

7 DISCUSSION

The KELT study of the photometric behavior of 610 Be stars found 21% of the Be stars show semi-regular outbursts (Labadie-Bartz et al. 2017, 2018). However, these are not necessarily periodic. Amongst the semi-regular outbursting Be stars, λ Eri has been shown to have periodic photometric outbursts with a period of either 469 d or 939 d (Mennickent et al. 1998), which are harmonics of each other. If we consider the longer period harmonics, λ Eri shows signs of multiple outbursts that have different strengths each cycle. Mennickent et al. (1998) also showed that HR 2142 had a periodic timescale of 344 d in its photometry.

The periodic nature of the outbursts can provide the context in which we can predict upcoming outbursts of disk activity in order to better observe and then model the formation scenarios of Be star disks. Our data presented here on HD 6226 have shown the strong activity cycles for pulsations and outbursting activities in this fairly bright Be star, similar to those seen for λ Eri and HR 2142. We anticipate that much of the predictable nature of the equivalent widths (see Fig. 6) can only be used to predict the time periods when outbursts should occur. We suspect that the recurrence timescales derived may be a sort of beating mode of multiple stellar pulsations, where the ‘difference/combination frequencies’ exist when there is some non-linear coupling coinciding with a maximum time of these pulsations ejecting material into the disk.

Given the two frequencies needed to reproduce the timing of the H α and H β variations in Fig. 6 and Table 4, we can speculate that the disk is grown through coherent addition of several various stellar phenomena. We see a slow pulsational period of 2.6 d (Section 4, Table 3) that is reminiscent of the slowly pulsating B stars and is not atypical amongst the classical Be stars. SPB stars have longer

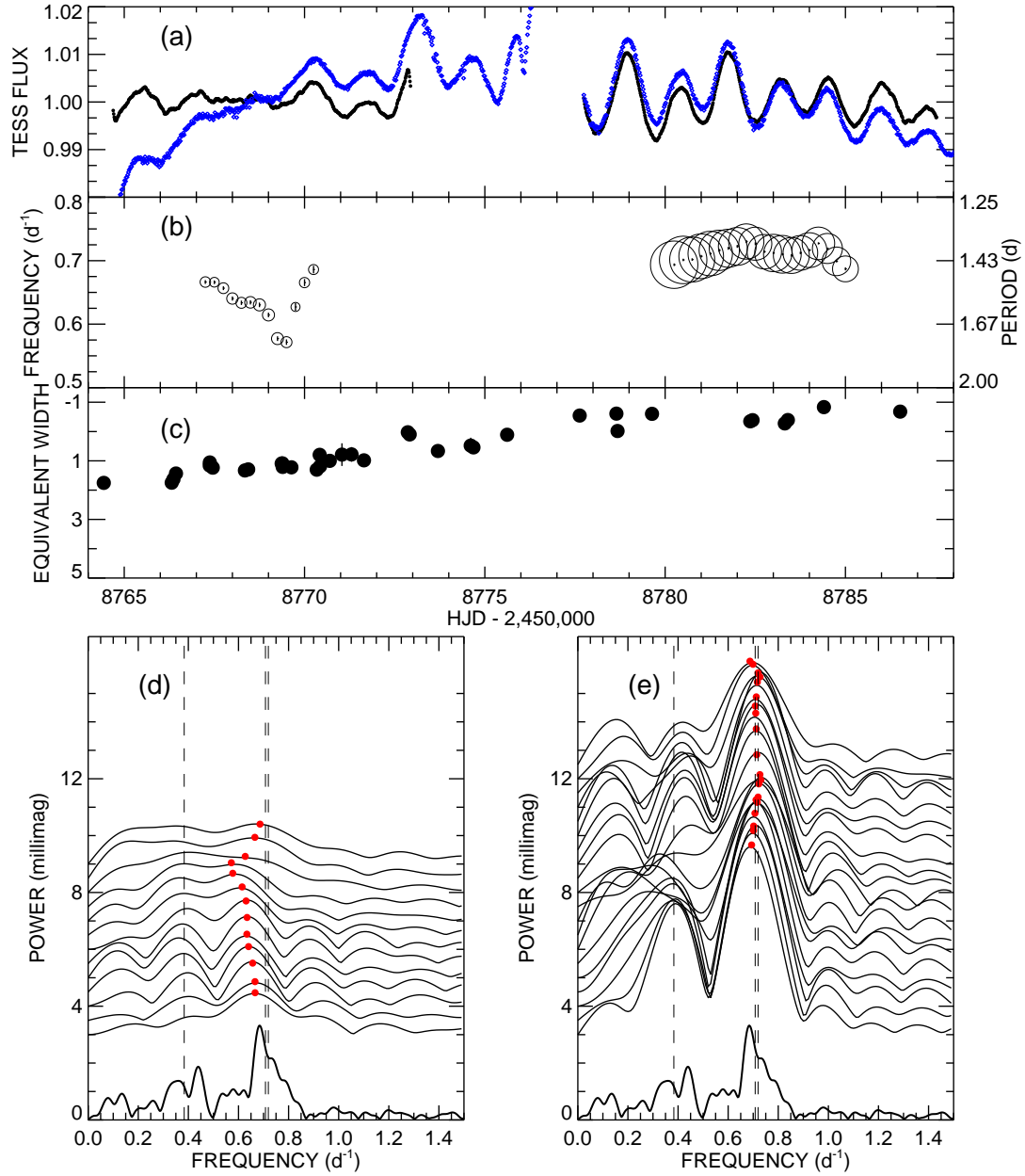


Figure 9. Panel (a): The *TESS* light curve is plotted (black: 2 minute cadence data; blue: full-frame image light curve). Panel (b): The measured frequencies for five-day increments of the time-string is shown. The errors on the measured frequencies are shown, and the circles representing the measurement are proportional to the measured amplitude of the measured frequencies. Panel (c): The measured $H\alpha$ equivalent width during the time of the *TESS* observations, which is seen to be increasing during the first half of this time period. Panels (d) and (e) show the Fourier spectra of the time-series. The bottom-most spectrum in bold is of the full time-series, and each spectrum above is representative of a five-day increment in the *TESS* data. Panel (d) shows the data from the first half of the *TESS* observations, while panel (e) shows the second half. In both panels (d) and (e), the red points indicate the peak frequency and amplitude of the individual Fourier spectra. The vertical dashed lines indicate the frequency of the pulsational signals discussed in Section 4.

pulsational periods than the β Cephei stars and likely are the result of g -modes rather than p -modes (see, e.g., Miglio et al. 2007a). Our results on the spectroscopic time series are indeed consistent with the mode calculations of Miglio et al. (2007a) for this star being a SPB star with an $l=1, 2$, or 3 mode. While our spectroscopic data do not directly show any additional modes, it has been well established that these stars often show multiple pulsational modes (see recent analysis of Fedurco et al. 2020), which could include the two photometric frequencies we discussed in Section 4.

It is reasonable to assume that the pulsational modes could be coupled to cause a disk outburst on these time scales, and in fact our analysis points to that being one of the mechanisms behind the disk outburst episodes. The secondary period used in the fit shown in Fig. 6 has a frequency of $0.0115 \text{ cycles day}^{-1}$, which corresponds to the dominant difference frequency of the two photometric oscillations we see in the KELT data at 0.7194 and $0.7079 \text{ cycles day}^{-1}$. Given the results of the fundamental parameters, we anticipate that these frequencies are similar to those seen in the *SMEI* and *BRITTE* photometry of 28 Cyg (Baade et al. 2018). Pulsations have long been thought to be a driving force behind the mass ejections in Be stars, but in the case of HD 6226, we see strong evidence that the coupling of two modes can build a disk from the analysis of the KELT photometry and BeSS spectroscopy. These two frequencies have amplitudes of 2.2 and 2.6 millimags. Given the difference in luminosity classes for these objects, a sub-giant for 28 Cyg and a giant for HD 6226, these modes may be g -modes for the star, although no spectroscopic signature is seen at these frequencies with our data for mode identification.

The $\sim 0.7 \text{ d}^{-1}$ frequency observed in HD 6226 was the strongest signal present in the short 25-day observation from *TESS*, which is similar to the two pulsational frequencies found with KELT at 0.70787 and 0.71940 d^{-1} . The *TESS* observations were fortuitously taken as the disk was building (Fig. 8) and near in time to when the beating of the frequencies were near the maximum of constructive interference (see Fig. 9). We note that the frequency measured from *TESS* data is likely at a phase where the combination of the two pulsational modes measured from the KELT data are adding together in a manner that the power and derived frequency would appear to change over this time period.

We can begin to understand more about the decay of the disk from the data in hand. In recent years, the viscous decretion disk (VDD) model has been successfully used to describe a large suite of multi-wavelength observational results of Be stars (e.g., Carciofi et al. 2012; Klement et al. 2015). The results of this model have been used to calculate the changes in photometry (Haubois et al. 2012) and polarization of the disk during an outburst (Haubois et al. 2014; Draper et al. 2011).

Rímulo et al. (2016) show that the photometry of the dissipation is generally given in the form of

$$m(t) = m_0 - (\Delta_{\text{mag}}) e^{-\frac{\epsilon_{\text{band}}(t-t_0)}{\tau}}.$$

In this derivation, $m(t)$ is the time-dependent magnitude, m_0 is the quiescent magnitude, Δ_{mag} is the amplitude of the decay, $\frac{\epsilon_{\text{band}}}{\tau}$ dictates the timescale of the decay of the light curve, and t_0 is a zero-point in time. From Haubois et al. (2012), we note that the parameter τ is inversely proportional to the viscosity parameter α of the disk. The models are built from the results of the HDUST models for the VDD that have been well described by Carciofi & Bjorkman (2006, 2008).

Our results for the $H\alpha$ and $H\beta$ line strength, shown in Fig. 6 and in detail for the first outburst in Fig. 10, are similar to the photometric

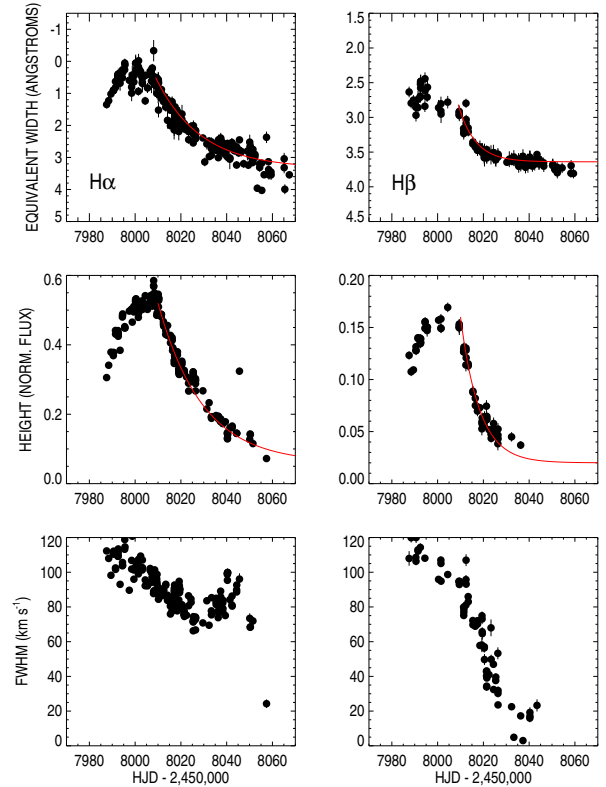


Figure 10. $H\alpha$ (left) and $H\beta$ (right) equivalent widths, peak height and the width of the emission feature during the best-observed outburst. We show similar fits for four more outbursts in Appendix A.

decay of Be stars such as ω CMa (Ghoreyshi et al. 2018) and therefore offer an exceptional dataset with which to fit the exponential decay of the disk dissipation. Of the six outbursts we observed, the first one, peaking near HJD 2,458,000), was the best observed so we concentrate our efforts on the discussion of this particular outburst. There is some evidence that the disk did not fully dissipate at the end of this episode, as we observe larger equivalent widths in mid-2019, but these changes are very small and likely will not influence our results.

In Figure 10, we show the measurements of equivalent width, the Gaussian peak height, and the Gaussian full-width-at-half-maximum (FWHM) for both $H\alpha$ and $H\beta$ during the first, and best-observed, outburst. These measurements were described in Section 5 and are tabulated online in the Appendix. The equivalent width variability can be understood as a proxy for the light emitted from the disk in these particular lines. The equivalent width is similar to the product of the height and FWHM, modified by a constant.

We did a basic fit of the exponential decay with an equation of form

$$W_{\lambda}(t) = W_{\lambda,0} + (W_{\lambda}(\text{peak}) - W_{\lambda,0}) e^{-\frac{(t-t_{\text{peak}})}{\Delta t}}.$$

This decay curve can be used for both the equivalent width as well as the peak height from the Gaussian fit of the residuals of the data and the TLUSTY model. This is estimated with an equivalent width or height, $W_{\lambda,0}$, the peak and quiescent emission, $W_{\lambda}(\text{peak}, 0)$, a time in which we estimate the curve has fully decayed, Δt , and the time of the peak emission prior to the decay, t_{peak} . We show estimates of the fits for the equivalent widths and peak heights of both $H\alpha$ and

Table 5. Estimated Exponential Decay for the Spectroscopic Measurements

Outburst 1								
Line	$W_{\lambda,0}$ (Å)	$W_{\lambda}(\text{peak})$ (Å)	Δt (d)	t_0 (HJD-2,450,000)	H_0 (norm.)	H (peak) (norm.)	Δt (d)	t_0 (HJD-2,450,000)
H α	3.34	0.6	19.5	8007.9	0.04	0.52	19.3	8010.0
H β	3.64	2.84	7.4	8010.0	0.02	0.16	8.3	8010.0.
Outburst 3								
H α	3.34	0.64	23.1	8366.3	0.06	0.52	23.1	8366.3
H β	3.70	3.00	13.2	8366.3	0.02	0.14	11.2	8368.3
Outburst 4								
H α	3.34	-0.50	37.5	8427.5	0.06	0.56	31.9	8443.7
H β	3.70	2.80	23.4	8440.6	0.02	0.18	23.4	8440.6
Outburst 5								
H α	3.34	-0.50	30.5	8792.8	0.20	0.69	28.1	8795.2
H β			Unable to fit		0.08	0.21	10.5	8798.4
Outburst 6								
H α	3.34	-0.27	19.5	8875.4				
H β							Unable to fit	

H β in Fig. 10. The parameters of these fits are shown in Table 5, and we expect the errors of these parameters to be on the order of 5%. We also performed similar fits to at least some of the data from the other four outbursts with reasonable observational coverage of the decay from the campaign, including the coefficients in Table 5 and including the similar figures in Appendix A.

We see from the data shown in Fig. 10 and the estimates of the exponential decay in Table 5 that the H β line decays much quicker than the H α emission. The optical depth at line center is much smaller for H β than for H α . If the disk is conceptually seen as a pseudo-photosphere of given radius (Vieira et al. 2015), then the size of the H α pseudo-photosphere would be larger than the H β one. Therefore, we see evidence that the disk clears from the inner to outer regions, as has been seen for other Be stars (e.g., Wisniewski et al. 2010).

We see from these simple fits to the data that the time scale for Δt to vary from ~ 19 to ~ 37 days for H α , and from ~ 7 to ~ 23 days for H β . The timescales of the disk show that the H α emission remains $\sim 1.4 - 2.7$ times longer than the H β line, which depends on the outburst. With a variety of timescales needed for fitting the decay of the disk in these two lines, we hypothesize that the viscosity parameter, α , could also be variable if the mass injection for the disk stops after the peak. This has been seen in the similar Be star ω CMa, which shows variability in the disk's viscosity coefficient from 0.1-1.0 according to the modeling of the optical light curve by Ghoreyshi et al. (2018). Alternatively, the disk injection could be lower after the peak, in which case the viscosity parameter α could be constant, with a variable disk injection rate.

Unfortunately, the KELT data did not cover this or other outbursts in our campaign with enough cadence to fit an exponential decay to the emergent flux in the KELT bandpass. We were also unable to have reasonable cadence from surveys such as ASAS-SN. A future campaign will need to have high cadence observations of photometry and spectroscopy during an outburst to fully characterize the viscosity parameters of the disk. However, we did find some lower-precision

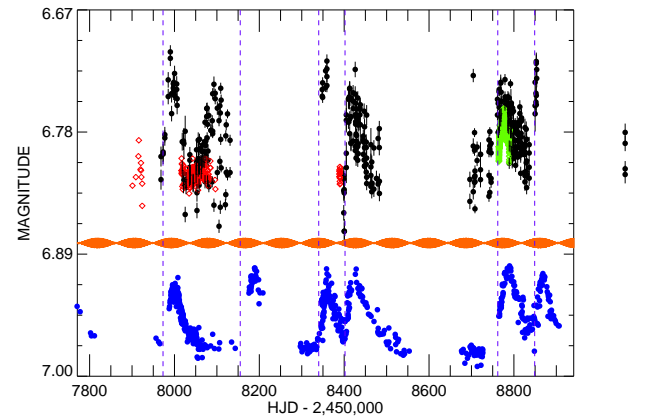


Figure 11. The KWS photometry is plotted in black, with the KELT data overplotted in red, and the 30-minute light curve from *TESS* shown in green. We show a scaled H α equivalent width curve in blue at the bottom. Our derived two-frequency fit for the KELT pulsations are shown in the orange curve, showing the clear beating pattern. We estimated the start times of the H α outbursts, and have marked those with vertical, purple dashed lines.

photometry taken with the Kamogata/Kiso/Kyoto Wide-field Survey (KWS)⁵.

In Fig. 11, we plot the KWS photometry, along with our limited KELT photometry, and the H α equivalent width variability seen in Fig. 6. In addition to the photometry and equivalent widths, we have overplotted the summation of the two pulsation modes found with KELT with frequencies near 0.7 d^{-1} . We see these two pulsation modes providing a beating pattern in the light curve, with the beat period that is comparable to the second frequency used in our Fourier analysis of the H α equivalent widths. We then estimated the timing

⁵ <http://kws.cetus-net.org/maehara/VSdata.py>

of the outbursts in the $H\alpha$ equivalent widths, i.e., the time that the equivalent width begins to grow, and compared these times to the beating pattern. Most of the $H\alpha$ outbursts are accompanied by photometric outbursts (although we are unable to fit the KWS data with an exponential decay like we did with $H\alpha$ and $H\beta$ (see Table 5). This plot shows that as the two modes begin beating constructively, the star sometimes begins to build its disk. It appears that sometimes the constructive interference of pulsational modes can build the Be star disk in the HD 6226 system.

We also see a change in the FWHM of the disk emission during the outbursts, as shown in Figs. 7 and 10. One can envision the disk as optically thick out to some radius, the pseudo-photosphere as described above, where the disk profile would be double-peaked at a more moderate inclination. In the case of HD 6226, our results are consistent with the disk clearing from the inside out during the outbursts. Near the end of these outbursts, some of the material may be falling back toward the star, causing the FWHM to grow at the end of these outbursts.

When the star begins an ejection of material, this feeds the disk and the material spreads outward in the disk. When the injection mechanism is turned off, likely when pulsational modes no longer add constructively for matter ejection near the stellar equator, the inner part of the disk begins to drain of material more quickly than the outer part. This causes the $H\beta$ line to decay faster than $H\alpha$, and then the FWHM of the emission will also become narrower. That is seen in detail in Fig. 10 and with the exponential decay fits in Table 5.

8 CONCLUSIONS

Our study of HD 6226 has found many interesting properties of the Be star, which we summarize here:

- The star shows a consistent spectral type with both optical spectra taken during the quiescent phase as well as with an ultraviolet spectrum taken with *HST* near the peak of an outburst. The spectral type is B2.5IIIe, based on the similarity of the B2.5III standard star π^2 Cygni. A TLUSTY model with $T_{\text{eff}} = 17,000$ K, $\log g = 3.0$, and $v \sin i = 70 \text{ km s}^{-1}$ matches our observations well. The system is seen near pole-on based on the inclination derived from our model, and is similar to these parameters from the TLUSTY model.

- HD 6226 is seen to have one pulsation period of 2.61553 d that is seen in spectroscopy. The variations are similar to those of a low-order mode, perhaps an $l = 2$ mode. There is some marginal power near this frequency in the Fourier analysis of the *TESS* data, but was very weak.

- The star shows a periodic behavior in the $H\alpha$ and $H\beta$ emission. Of the two periods (212 and 87 d) found for the $H\alpha$ behavior, we find that the 87 d period is a difference frequency of two pulsational frequencies observed in the KELT data. The predicted curve, shown in Fig. 6, predicts the times of maximum and minimum equivalent width. We encourage observers to take frequent spectra of HD 6226 in the month or more prior to predicted times of outburst so that the build-up of disk material can be well observed. Thus far, no outburst has been seen in detail from the beginning of the material build-up.

- When the star begins an outburst, we see a wide emission profile superimposed on the stellar photospheric line. The peak was fit with a Gaussian profile, which we see having a wide full-width-at-half-maximum and then becoming more narrow with time. This can be interpreted as material moving from the interior to the outer parts of the disk. The disk then dissipates leaving the profile too weak to detect the signature of material falling back onto the star. This general

picture agrees with the hydrodynamic simulations of Haubois et al. (2012).

- The $H\alpha$ and $H\beta$ variability during the outbursts is similar to the photometric behavior that has been modeled for other Be stars during their outbursts (e.g., Vieira et al. 2017). The decay curves can be used for future modeling with the viscous accretion disk codes used for Be star disks (e.g., Haubois et al. 2012; Ghoreyshi et al. 2018). No general modeling for the viscous disk parameters has been done for the entire population of Be stars, so the exact parameters of the disk decay are unconstrained. The time scale for each of the outbursts is different, indicating that the viscosity parameter is variable with each outburst or that the mass injection rate is variable.

- Two of the modes seen in the KELT photometry have a beating frequency that is equal to one of the two frequencies found in the Fourier analysis of the $H\alpha$ and $H\beta$ equivalent widths. The beating properties indicate that the constructive interference of the pulsational modes could be the driving mechanism behind the outbursts for this Be star.

The continued study of the star HD 6226 will be necessary for a better understanding of how disks are built and dissipate for Be stars. The most needed observations in future are a confirmation of periodic behavior of the outbursts, and potentially a study of the polarization of the disk during an outburst. It's unclear if we should expect a signature of polarization because of the near pole-on orientation of the star. However, if this is caught very early in an outburst, a strong polarization signal could be seen as the material is ejected from a particular spot on the stellar surface. The fact that the outbursts appear to be periodic allows us to consider mounting observational campaigns to catch the outburst with multiple techniques such as photometry, spectroscopy, polarimetry, or even long baseline interferometry. We had also considered modeling the phase variations of the line profiles with current asteroseismology tools such as FAMIAS (Zima 2008). However, these tools assume a non-rotating star, and Be stars are known to be rotating at nearly critical speeds. Furthermore, our data are of lower S/N and spectral resolution than needed for the code, given the typical data quality found in BeSS. The complete analysis of this pulsational mode will require a dedicated campaign in the future.

The unique time frame and data set collected during the time that *TESS* observed the star represents one of the best data sets collected showing the growth of a disk of a Be star. The complementary spectroscopy and *TESS* photometry will undoubtedly prove essential to future modeling efforts of Be stars and their disks. Other Be stars have been observed by both *TESS* and *BRITe-Constellation*, but very few with such extensive spectroscopic coverage. We hope this study will help to excite amateur spectroscopists to provide similar data sets for both HD 6226 and other Be stars in the future.

DATA AVAILABILITY

The data for this paper are largely available online, with links given for various surveys used throughout the text. *HST* and *TESS* data are available freely from MAST. The optical spectroscopy are largely available through BeSS, and most of the KELT data were from Labadie-Bartz et al. (2017). Any author requesting any spectra that are not in BeSS or MAST is encouraged to contact the authors for these data.

ACKNOWLEDGEMENTS

Some spectra were obtained with the Ritter 1-m telescope. Ritter Observatory recently celebrated its fiftieth anniversary of first light during the course of this project, and we dedicate this paper to the hard work and determination of the retired observatory directors Adolf Witt, Bernie Bopp, and Nancy Morrison. Observations at Ritter Observatory would not have been possible without the support and hard work of the observatory technician, Michael Brown. Further, many of the Ritter observations were supported by an enthusiastic team of undergraduate students who volunteered their time, whom we thank for their dedication. We also thank Peter Wysocki for their help with the GalPy calculations in Section 3.

This work has made use of data from the European Space Agency (ESA) mission *Gaia* (<https://www.cosmos.esa.int/gaia>), processed by the *Gaia* Data Processing and Analysis Consortium (DPAC, <https://www.cosmos.esa.int/web/gaia/dpac/consortium>). Funding for the DPAC has been provided by national institutions, in particular the institutions participating in the *Gaia* Multi-lateral Agreement. This work has also made use of the BeSS database, operated at LESIA, Observatoire de Meudon, France: <http://basebe.obspm.fr>. The professional astronomers thank this international group of enthusiastic amateur spectroscopists for their time and personal investments in this project, as their curiosity was contagious amongst our team. We also thank Justin Barnes for assistance in creating the 3D STL file presented in Appendix B and to Kristy Richardson for assistance in photographing the 3D-printed model.

Support for *HST* Program number 15432 was provided by NASA through a grant from the Space Telescope Science Institute, which is operated by the Association of Universities for Research in Astronomy, Incorporated, under NASA contract NAS 5–26555. This paper includes data collected by the TESS mission through the TESS-GI program G022064. Funding for the TESS mission is provided by the NASA Explorer Program.

NDR acknowledges previous postdoctoral support by the University of Toledo and by the Helen Luedtke Brooks Endowed Professorship. JEB and KSB acknowledge support of the NSF through grant AST-1412135. Participation in this project by A. Daly and A. Lane was supported by Embry-Riddle Aeronautical University's Undergraduate Research Institute. DRG is supported through NSF grant AST-190826. ACC acknowledges support from CNPq (grant 311446/2019-1) and FAPESP (grant 2018/04055-8). ACR acknowledges the support of FAPESP grants 2017/08001-7 and 2018/13285-7. MG acknowledges the support of FAPESP grant 2018/05326-5. This work made use of the computing facilities of the Laboratory of Astroinformatics (IAG/USP, NAT/Unicsul), whose purchase was made possible by the Brazilian agency FAPESP (grant 2009/54006-4) and the INCT-A. D.J.S. is supported as an Eberly Research Fellow by the Eberly College of Science at the Pennsylvania State University. The Center for Exoplanets and Habitable Worlds is supported by the Pennsylvania State University, the Eberly College of Science, and the Pennsylvania Space Grant Consortium.

REFERENCES

Abt H. A., Levato H., Grosso M., 2002, *ApJ*, **573**, 359
 Aerts C., Christensen-Dalsgaard J., Kurtz D. W., 2010, *Asteroseismology*
 Baade D., et al., 2018, *A&A*, **610**, A70
 Boubert D., Evans N. W., 2018, *MNRAS*, **477**, 5261
 Božić H., et al., 2004, *A&A*, **416**, 669

Bovy J., 2015, *ApJS*, **216**, 29
 Božić H., Harmanec P., 1998, *A&A*, **330**, 222
 Carciofi A. C., 2011, in Neiner C., Wade G., Meynet G., Peters G., eds, *IAU Symposium Vol. 272, Active OB Stars: Structure, Evolution, Mass Loss, and Critical Limits*. pp 325–336 ([arXiv:1009.3969](https://arxiv.org/abs/1009.3969)), [doi:10.1017/S1743921311010738](https://doi.org/10.1017/S1743921311010738)
 Carciofi A. C., Bjorkman J. E., 2006, *ApJ*, **639**, 1081
 Carciofi A. C., Bjorkman J. E., 2008, *ApJ*, **684**, 1374
 Carciofi A. C., Bjorkman J. E., Otero S. A., Okazaki A. T., Štefl S., Rivinius T., Baade D., Haubois X., 2012, *ApJ*, **744**, L15
 Cardelli J. A., Clayton G. C., Mathis J. S., 1989, *ApJ*, **345**, 245
 Donati J. F., Semel M., Carter B. D., Rees D. E., Collier Cameron A., 1997, *MNRAS*, **291**, 658
 Draper Z. H., Wisniewski J. P., Bjorkman K. S., Haubois X., Carciofi A. C., Bjorkman J. E., Meade M. R., Okazaki A., 2011, *ApJ*, **728**, L40
 Fedurco M., Paunzen E., Hümmerich S., Bernhard K., Parimucha Š., 2020, *A&A*, **633**, A122
 Foreman-Mackey D., Hogg D. W., Lang D., Goodman J., 2013, *PASP*, **125**, 306
 Gaia Collaboration et al., 2018, *A&A*, **616**, A1
 Gandet T. L., 2019, *Research Notes of the American Astronomical Society*, **3**, 151
 Georgy C., Ekström S., Granada A., Meynet G., Mowlavi N., Eggenberger P., Maeder A., 2013a, *A&A*, **553**, A24
 Georgy C., et al., 2013b, *A&A*, **558**, A103
 Ghoreyshi M. R., et al., 2018, *MNRAS*, **479**, 2214
 Gies D. R., Bagnuolo William G. J., Ferrara E. C., Kaye A. B., Thaller M. L., Penny L. R., Peters G. J., 1998, *ApJ*, **493**, 440
 Goodman J., Weare J., 2010, *Communications in Applied Mathematics and Computational Science*, **5**, 65
 Hartman J., 2012, VARTOOLS: Light Curve Analysis Program ([ascl:1208.016](https://ascl.net/1208.016))
 Haubois X., Carciofi A. C., Rivinius T., Okazaki A. T., Bjorkman J. E., 2012, *ApJ*, **756**, 156
 Haubois X., Mota B. C., Carciofi A. C., Draper Z. H., Wisniewski J. P., Bednarski D., Rivinius T., 2014, *ApJ*, **785**, 12
 Hinkle K., Wallace L., Valenti J., Harmer D., 2000, *Visible and Near Infrared Atlas of the Arcturus Spectrum 3727-9300 Å*
 Jenkins J. M., et al., 2016, in *Proc. SPIE*. p. 99133E, [doi:10.1117/12.2233418](https://doi.org/10.1117/12.2233418)
 Kimble R. A., et al., 1998, *ApJ*, **492**, L83
 Klement R., et al., 2015, *A&A*, **584**, A85
 Kovács G., Bakos G., Noyes R. W., 2005, *MNRAS*, **356**, 557
 Kraus S., et al., 2012, *ApJ*, **744**, 19
 Labadie-Bartz J., et al., 2017, *AJ*, **153**, 252
 Labadie-Bartz J., et al., 2018, *AJ*, **155**, 53
 Lanz T., Hubeny I., 2007, *ApJS*, **169**, 83
 Lee U., Osaki Y., Saio H., 1991, *MNRAS*, **250**, 432
 Lenz P., Breger M., 2005, *Communications in Asteroseismology*, **146**, 53
 Lesh J. R., 1968, *ApJS*, **17**, 371
 McSwain M. V., Gies D. R., 2005, *ApJS*, **161**, 118
 Mennickert R. E., Sterken C., Vogt N., 1998, *A&A*, **330**, 631
 Miglio A., Montalbán J., Dupret M. A., 2007a, *Communications in Asteroseismology*, **151**, 48
 Miglio A., Montalbán J., Dupret M.-A., 2007b, *MNRAS*, **375**, L21
 Mota B. C., 2019, PhD thesis, Instituto de Astronomia, Geofísica e Ciências Atmosféricas, Universidade de São Paulo
 Mourard D., et al., 2015, *A&A*, **577**, A51
 Neiner C., de Batz B., Cocharad F., Floquet M., Mekkas A., Desnoux V., 2011, *AJ*, **142**, 149
 Nieva M.-F., Przybilla N., 2014, *A&A*, **566**, A7
 Pepper J., et al., 2007, *PASP*, **119**, 923
 Pepper J., Kuhn R. B., Siverd R., James D., Stassun K., 2012, *PASP*, **124**, 230
 Petit P., Louge T., Théado S., Paletou F., Manset N., Morin J., Marsden S. C., Jeffers S. V., 2014, *PASP*, **126**, 469
 Ricker G. R., et al., 2016, in *Proc. SPIE*. p. 99042B, [doi:10.1117/12.2232071](https://doi.org/10.1117/12.2232071)
 Rímulo L. R., Carciofi A. C., Rivinius T., Okazaki A., 2016, in Sígut T. A. A., Jones C. E., eds, *Astronomical Society of the Pacific Conference Series*

- Vol. 506, Bright Emissaries: Be Stars as Messengers of Star-Disk Physics.
p. 157
- Rivinius T., Baade D., Stefl S., Stahl O., Wolf B., Kaufer A., 1998, *A&A*,
[333](#), [125](#)
- Rivinius T., Baade D., Štefl S., 2003, *A&A*, [411](#), [229](#)
- Rivinius T., Carciofi A. C., Martayan C., 2013, *A&ARv*, [21](#), [69](#)
- Rountree J., Sonneborn G., 1991, *ApJ*, [369](#), [515](#)
- Rountree J., Sonneborn G., 1993, NASA Reference Publication, [1312](#)
- Shokry A., et al., 2018, *A&A*, [609](#), [A108](#)
- Sigut T. A. A., Patel P., 2013, *ApJ*, [765](#), [41](#)
- Vieira R. G., Carciofi A. C., Bjorkman J. E., 2015, *MNRAS*, [454](#), [2107](#)
- Vieira R. G., Carciofi A. C., Bjorkman J. E., Rivinius T., Baade D., Rímulo
L. R., 2017, *MNRAS*, [464](#), [3071](#)
- Vollmann K., Eversberg T., 2006, *Astronomische Nachrichten*, [327](#), [862](#)
- Wade G. A., et al., 2016, *MNRAS*, [456](#), [2](#)
- Wang L., Gies D. R., Peters G. J., 2018, *ApJ*, [853](#), [156](#)
- Wisniewski J. P., Draper Z. H., Bjorkman K. S., Meade M. R., Bjorkman
J. E., Kowalski A. F., 2010, *ApJ*, [709](#), [1306](#)
- Zima W., 2008, *Communications in Asteroseismology*, [155](#), [17](#)
- Šlechta M., Škoda P., 2005, *Ap&SS*, [296](#), [179](#)
- von Zeipel H., 1924, *MNRAS*, [84](#), [665](#)

APPENDIX A: ADDITIONAL FIGURES

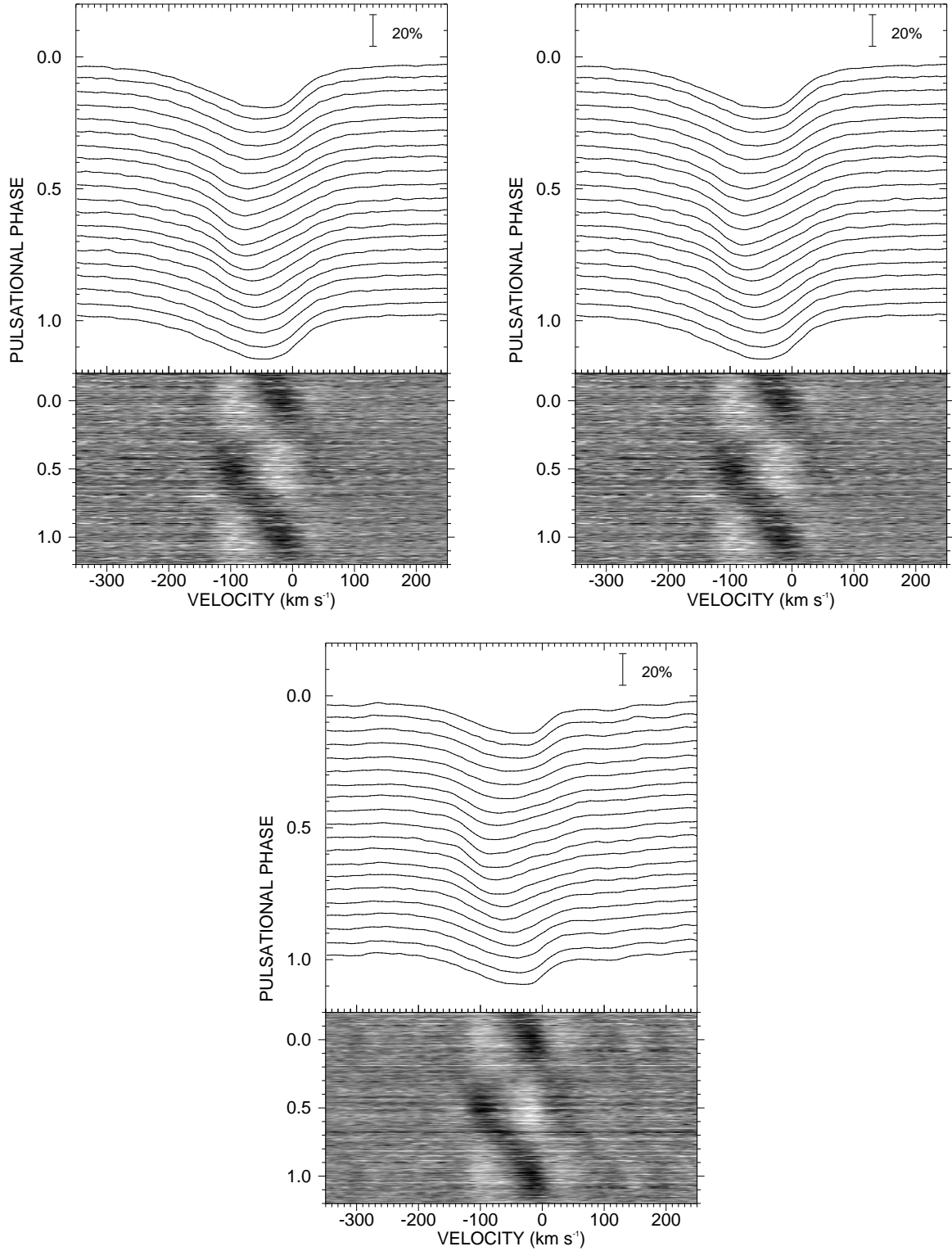


Figure A1. Dynamical representation of HD 6226 He I $\lambda\lambda 4471$ (top left), 4713 (top right), 4921 (bottom) profiles spectra during our campaign for the 2.6 d pulsational period. The grey scales show the differences from an average profile and the phasing is the same as in Fig. 4. The black/white contrast indicates a $\pm 4\%$ deviation in each plot. The depth of the individual line profiles is shown in continuum units in each panel. Each shown line profile represents an average of all observations in a 0.05 phase interval. Representations of the He I $\lambda 5876$ and Mg II 4481 profiles are shown in Fig. 4.

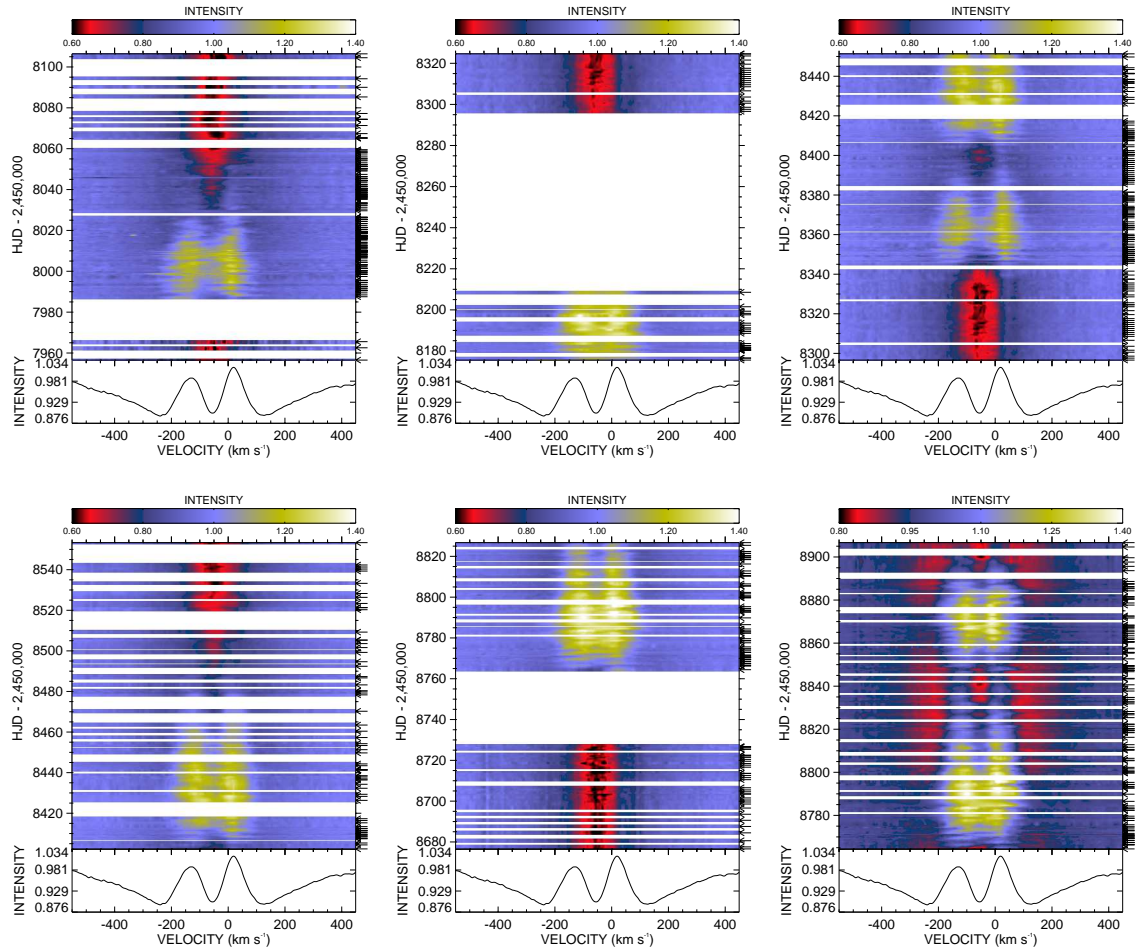


Figure A2. Dynamical representation of HD 6226 H α profiles spectra during our campaign. The average profile for the campaign is shown in the bottom panel of each plot and the vertical scale of each plot is made to be ~ 150 d for each panel, allowing for some overlap between some of the dynamical spectra. Gaps are made to represent gaps in data ≥ 2 d.

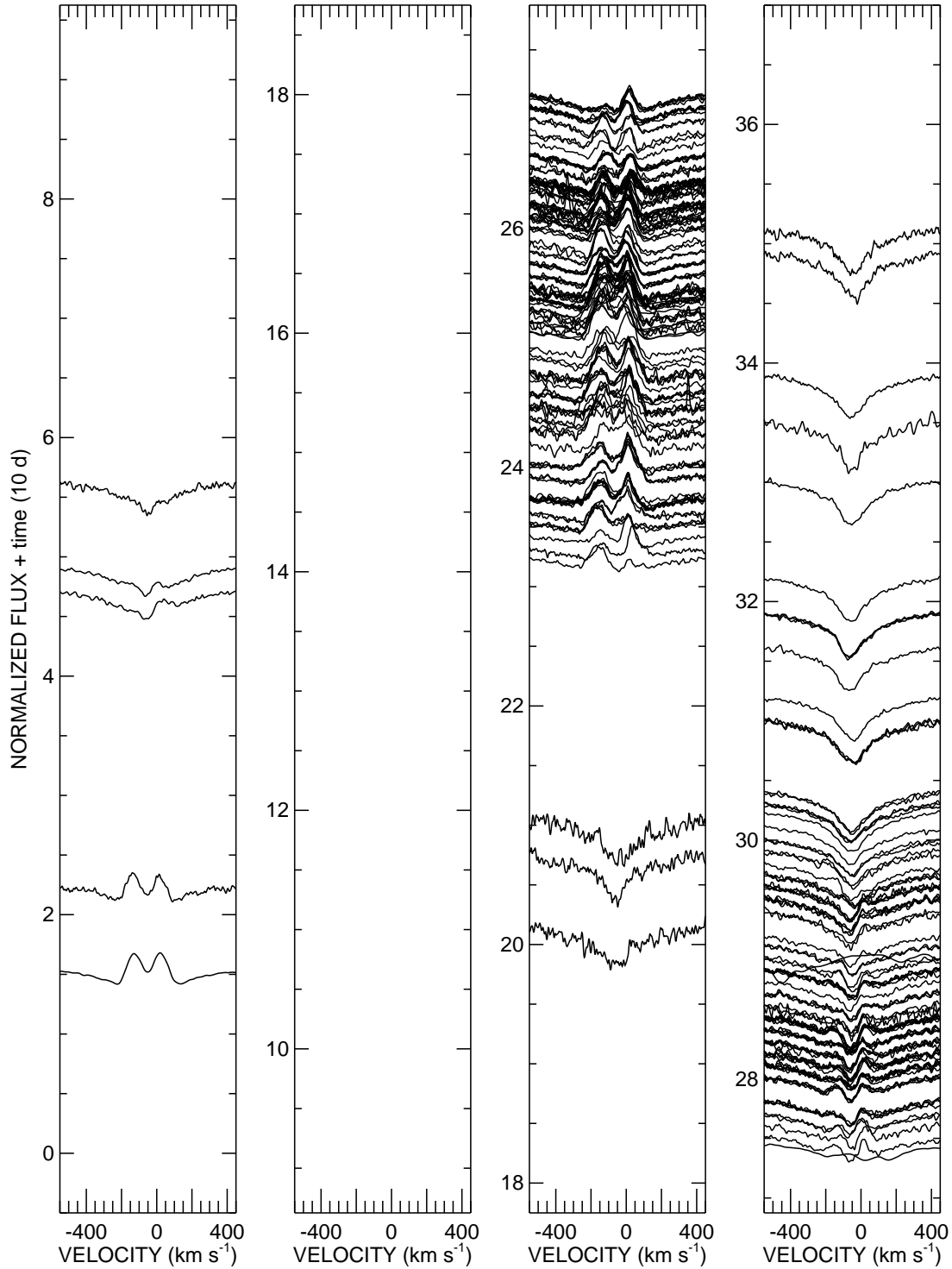


Figure A3. Line profiles of HD 6226 H α profiles spectra during 2017. The offset for the spectra is representative of 10 d per each vertical value of 1. The time point of 0 represents 2017 January 1.

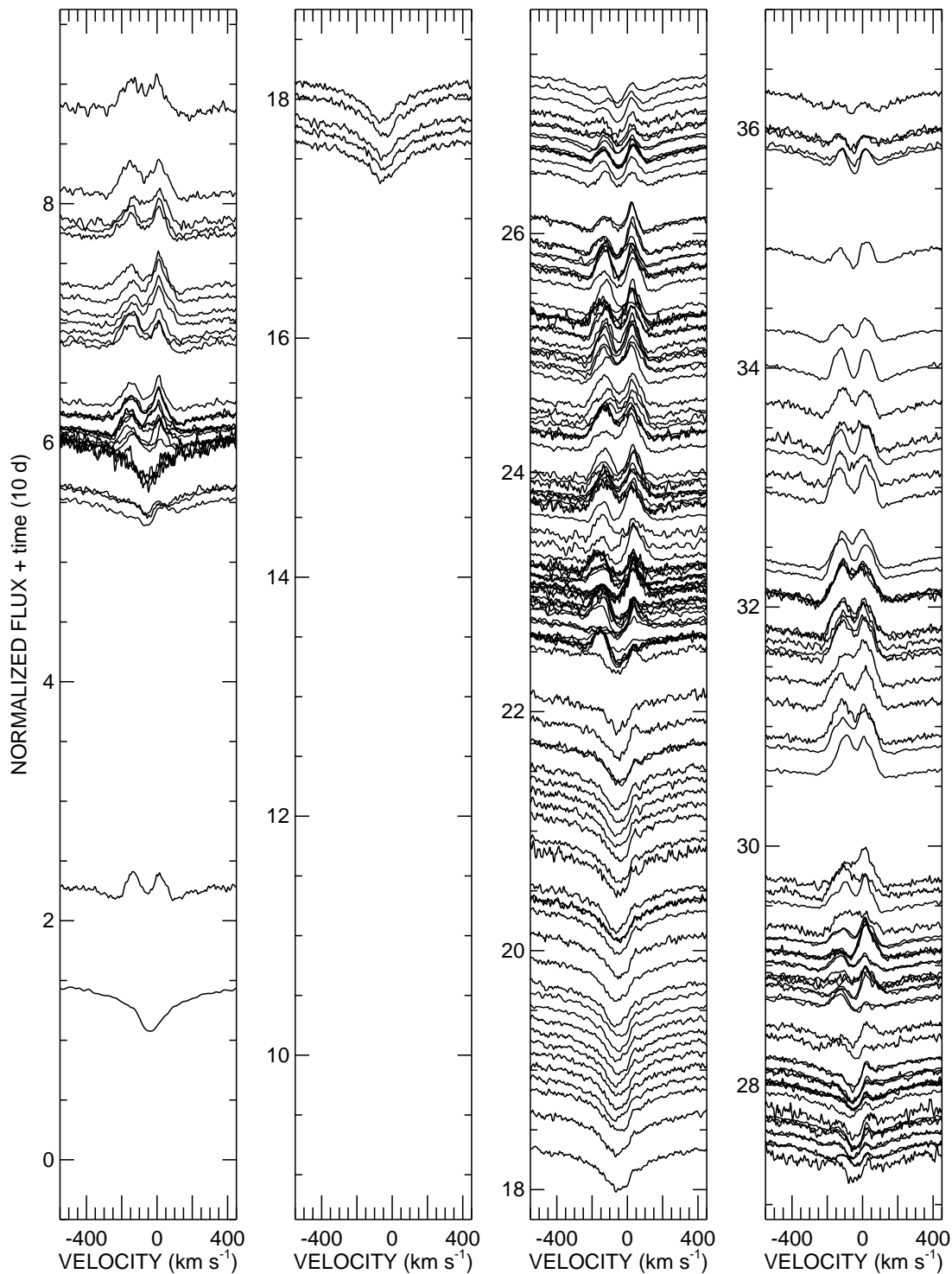


Figure A4. Line profiles of HD 6226 H α profiles spectra during 2018. The offset for the spectra is representative of 10 d per each vertical value of 1. The time point of 0 represents 2018 January 1.

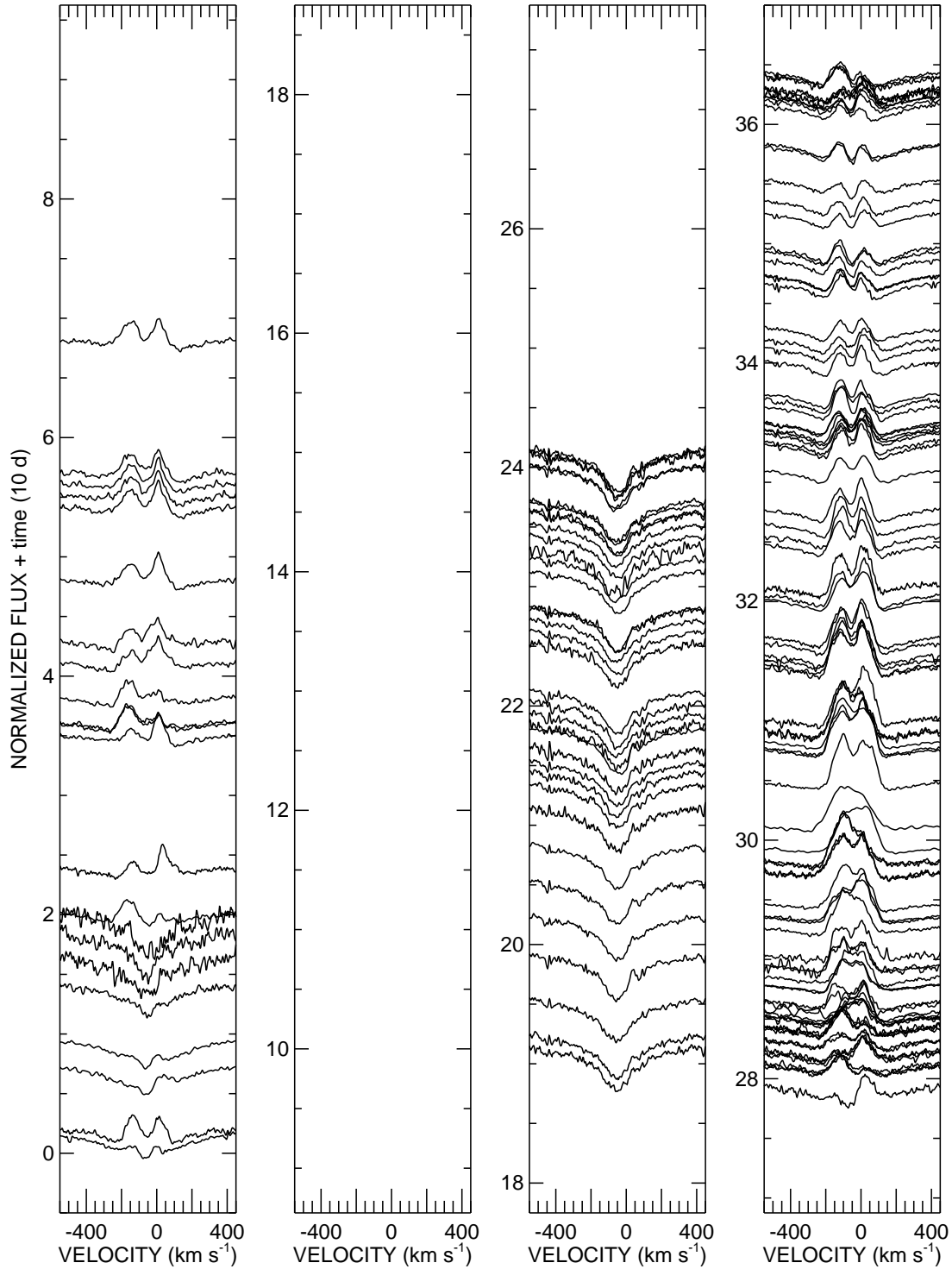


Figure A5. Line profiles of HD 6226 H α profiles spectra during 2019. The offset for the spectra is representative of 10 d per each vertical value of 1. The time point of 0 represents 2019 January 1.

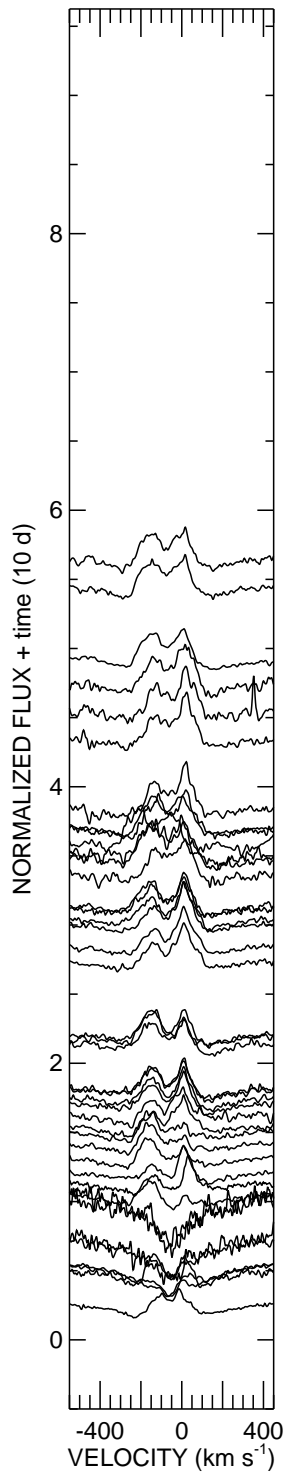


Figure A6. Line profiles of HD 6226 $H\alpha$ profiles spectra during 2020 that were used in this analysis. The offset for the spectra is representative of 10 d per each vertical value of 1. The time point of 0 represents 2020 January 1.

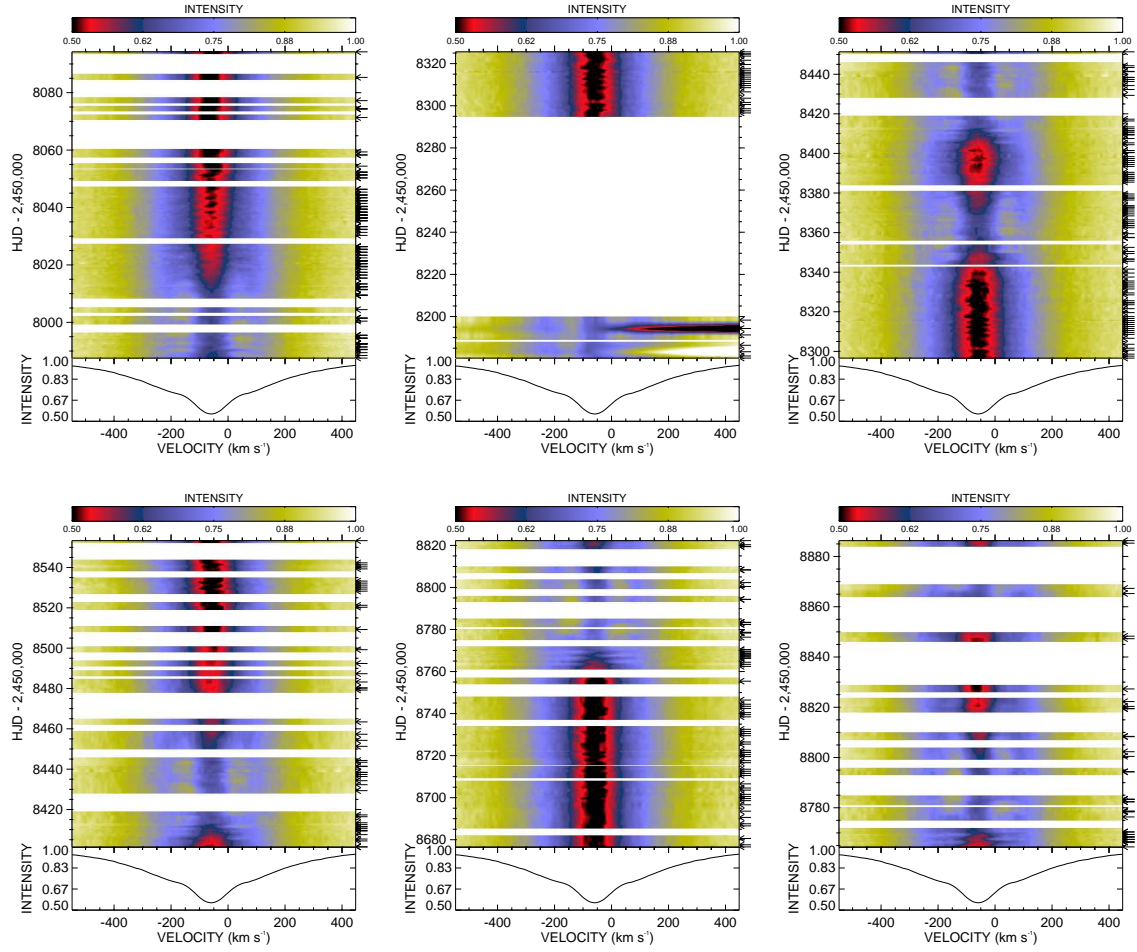


Figure A7. Dynamical representation of HD 6226 $H\beta$ profiles spectra during our campaign. The average profile for the campaign is shown in the bottom panel of each plot and the vertical scale of each plot is made to be ~ 150 d for each panel, allowing for some overlap between some of the dynamical spectra. Gaps are made to represent gaps in data ≥ 2 d.

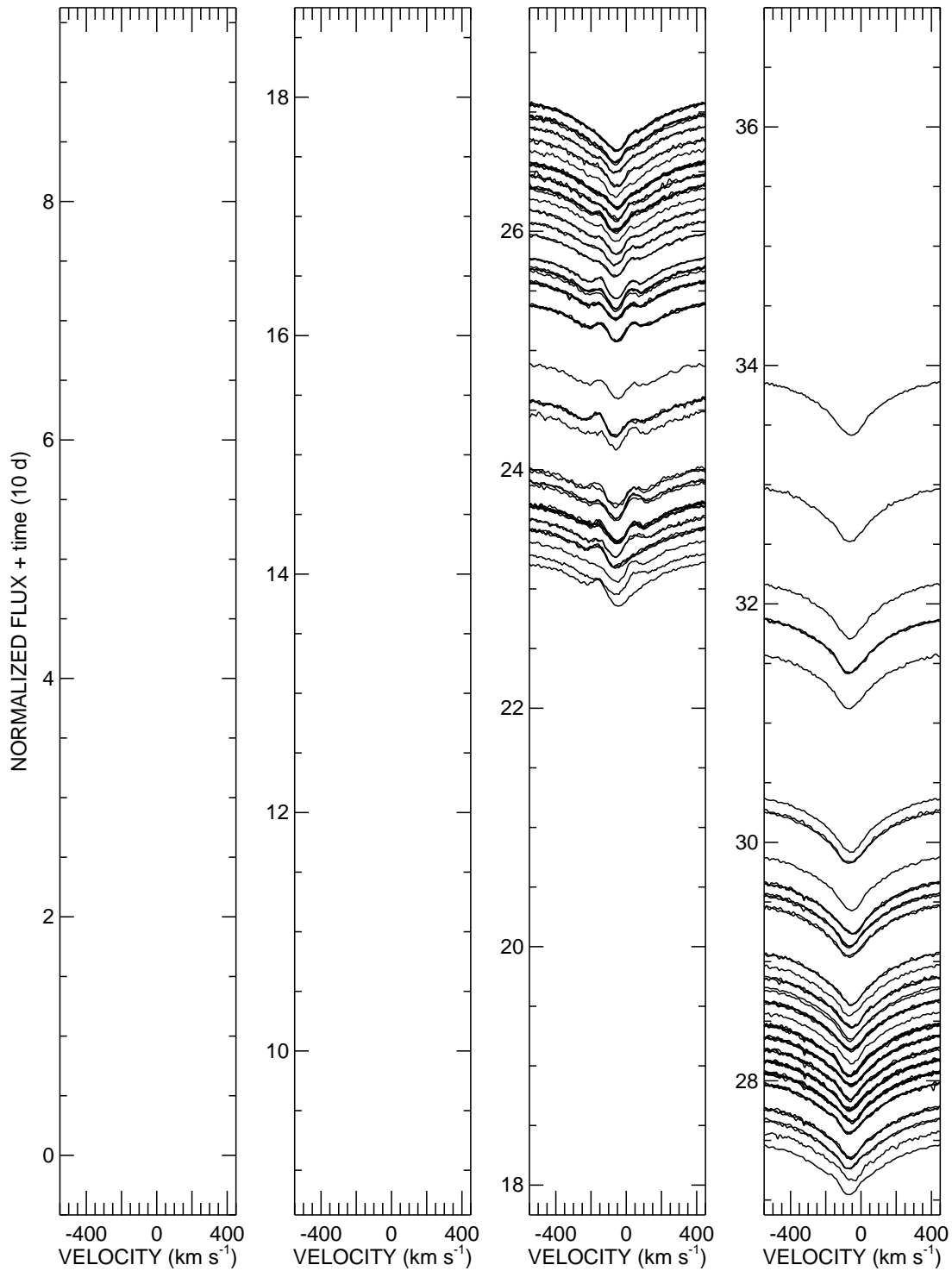


Figure A8. Line profiles of HD 6226 H α profiles spectra during 2017. The offset for the spectra is representative of 10 d per each vertical value of 1. The time point of 0 represents 2017 January 1.

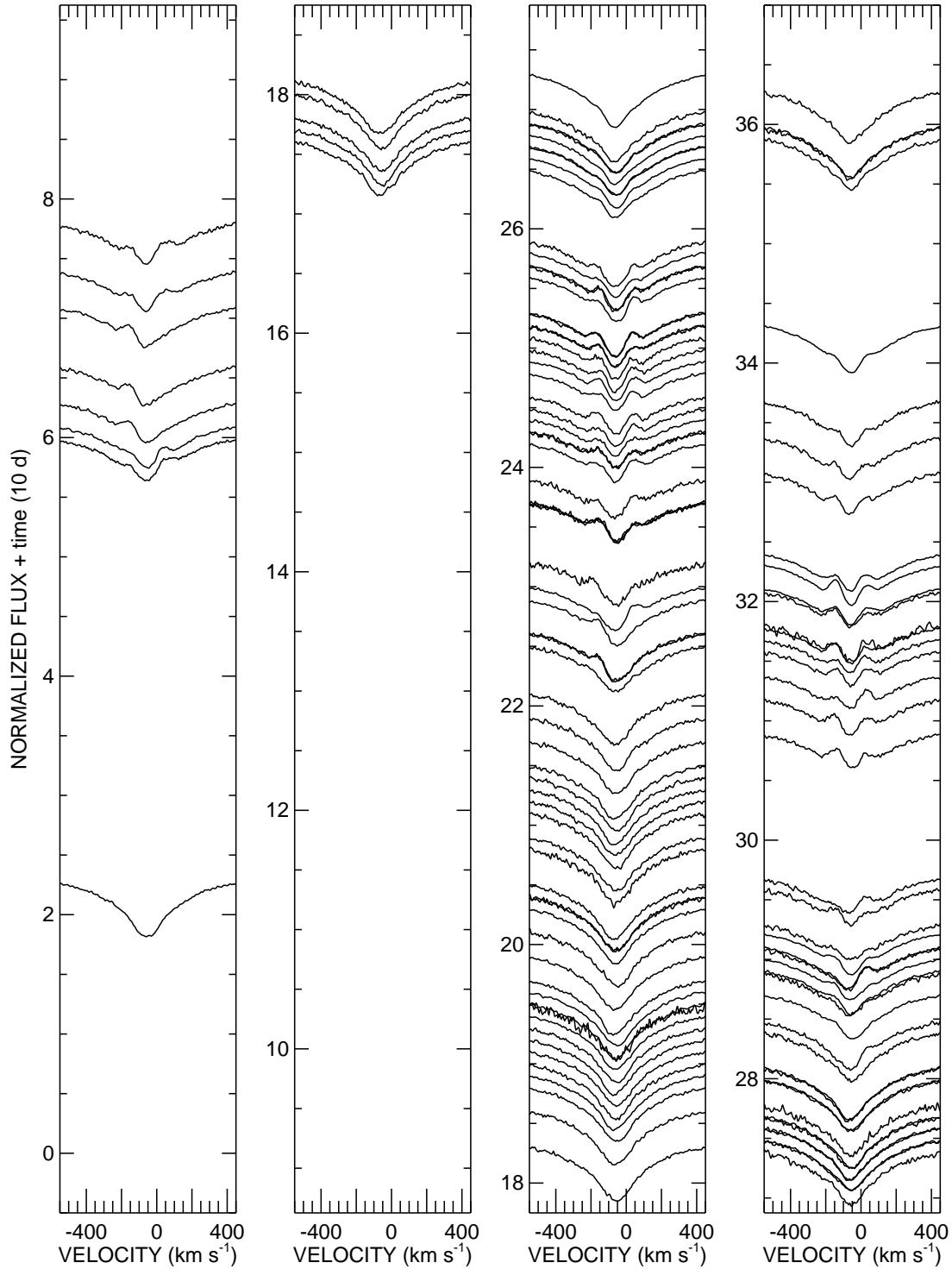


Figure A9. Line profiles of HD 6226 H α profiles spectra during 2018. The offset for the spectra is representative of 10 d per each vertical value of 1. The time point of 0 represents 2018 January 1.

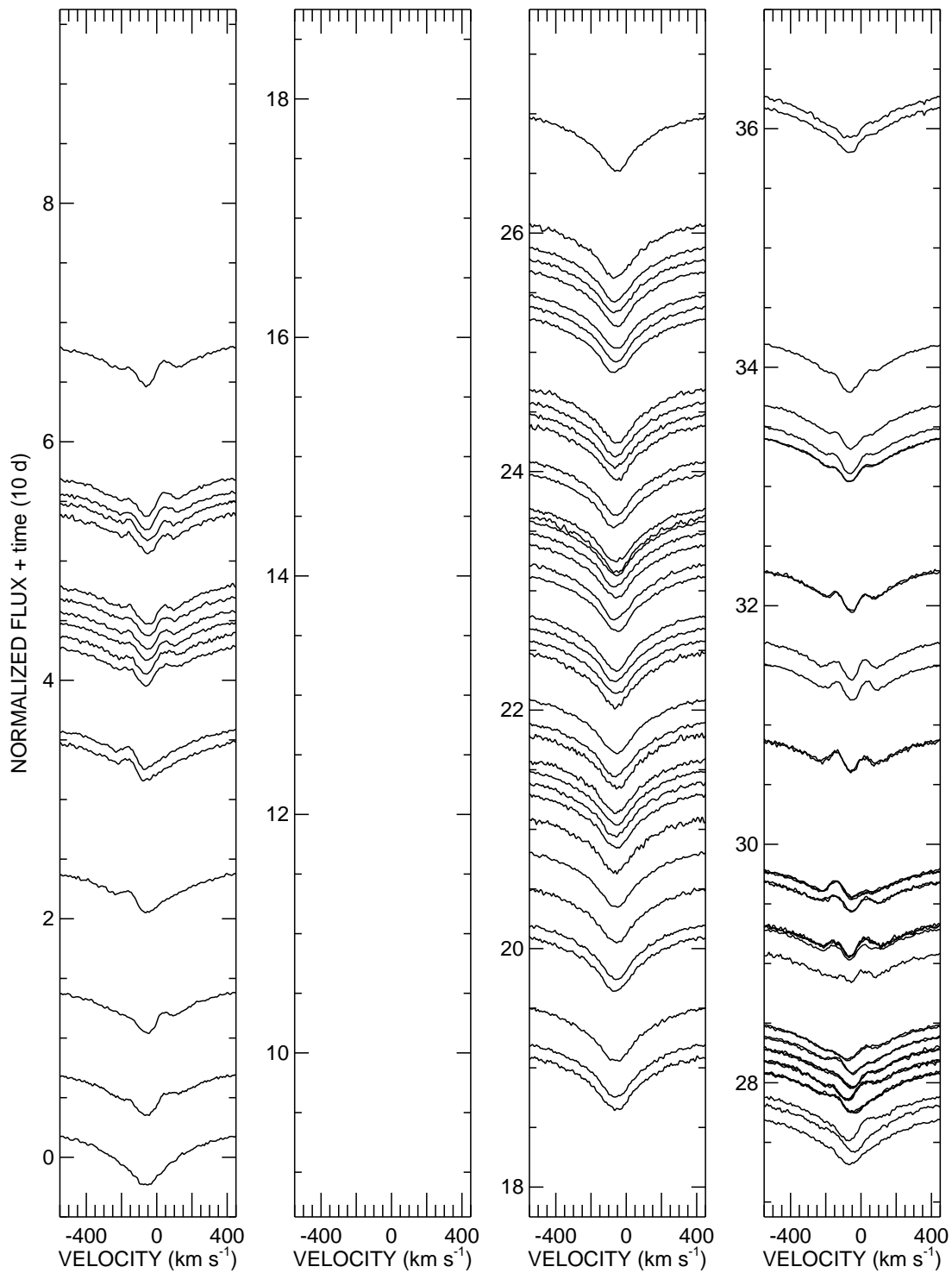


Figure A10. Line profiles of HD 6226 H α profiles spectra during 2019. The offset for the spectra is representative of 10 d per each vertical value of 1. The time point of 0 represents 2019 January 1.

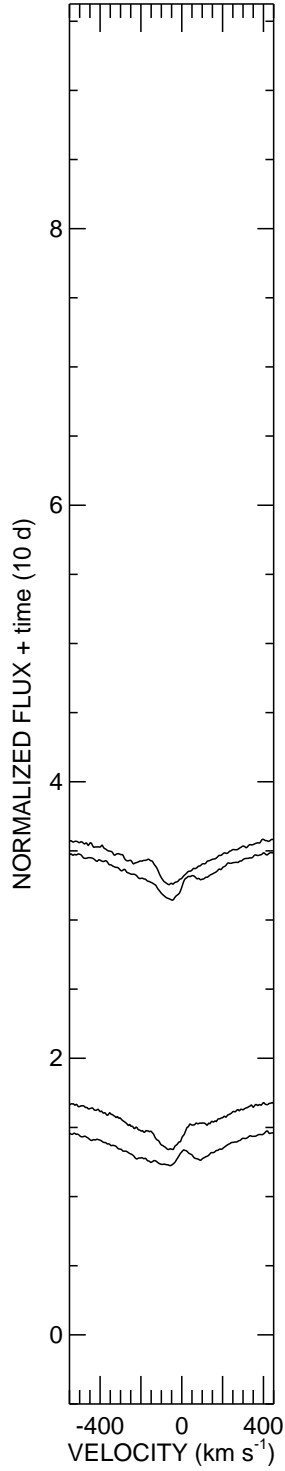


Figure A11. Line profiles of HD 6226 H α profiles spectra during 2020 that were used in this analysis. The offset for the spectra is representative of 10 d per each vertical value of 1. The time point of 0 represents 2020 January 1.

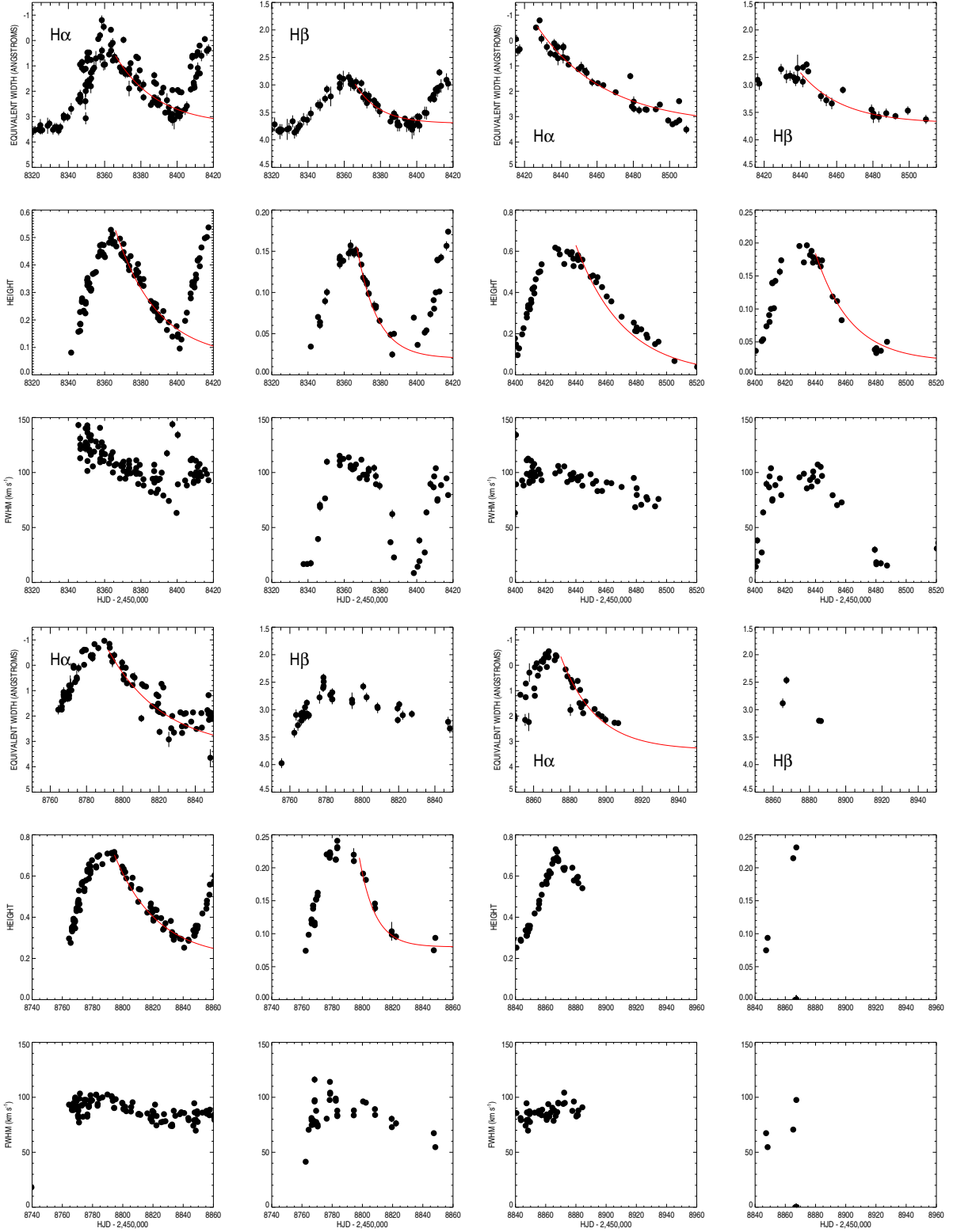


Figure A12. Modeling of the disk dissipation for four additional outbursts seen in our spectroscopic data, in the same format as Fig. 10, with the fit parameters given in Table 5.

APPENDIX B: DATA TABLES

This paper has been typeset from a \TeX/L\AA\TeX file prepared by the author.

Table B1. Radial Velocity Measurements

HJD-2450000	He I 4471	He I 4721	He I 4921	He I 5876	Mg II 4481
7987.5452	-56.13 ± 0.94	-56.20 ± 1.05	-51.78 ± 1.07	-49.96 ± 1.00	-57.55 ± 1.53
7988.4413	-57.60 ± 0.65	-63.27 ± 0.85	-59.11 ± 0.82	...	-65.28 ± 0.98
7989.4361	-59.95 ± 0.80	-52.87 ± 1.02	-54.21 ± 1.26	-55.99 ± 0.92	-49.94 ± 0.97
7990.4747	-59.26 ± 0.87	-60.16 ± 1.03	-56.01 ± 0.95	-53.50 ± 1.34	-60.14 ± 1.33
7990.5549	-58.91 ± 0.83	-57.01 ± 1.32	-55.26 ± 1.12	-53.56 ± 1.49	-65.39 ± 1.54
7990.6008	-58.82 ± 1.09	-61.87 ± 1.27	-58.24 ± 1.20	-56.08 ± 1.20	-66.63 ± 1.41
7991.4147	-60.44 ± 0.71	-55.27 ± 0.75	-55.79 ± 0.87	-57.93 ± 0.74	-61.21 ± 0.79
7991.4571	-60.39 ± 0.76	-59.50 ± 1.13	-53.14 ± 0.87	-57.23 ± 0.72	-64.59 ± 1.37
7992.4143	-60.68 ± 0.79	-55.90 ± 1.02	-55.24 ± 1.35	-54.71 ± 1.01	-49.20 ± 1.54
7992.4566	-60.84 ± 1.02	-58.42 ± 1.22	-58.29 ± 1.31	-54.56 ± 1.11	-48.91 ± 1.14
7992.4990	-58.19 ± 0.90	-57.72 ± 1.26	-56.96 ± 1.44	-56.25 ± 1.18	-58.79 ± 1.19
7992.5414	-62.15 ± 1.23	-60.84 ± 1.52	-56.46 ± 1.26	-56.06 ± 1.15	-53.76 ± 1.42
7992.5840	-60.60 ± 1.11	-54.63 ± 1.69	-57.12 ± 1.47	-59.00 ± 1.00	-59.05 ± 1.71
7992.6265	-61.79 ± 1.30	-59.23 ± 1.22	-61.15 ± 1.30	-57.28 ± 1.13	-54.42 ± 1.71
7994.4410	-56.71 ± 0.73	-53.98 ± 0.87	-53.02 ± 1.01	-53.81 ± 0.76	-60.40 ± 0.89
7994.4835	-55.99 ± 0.64	-51.99 ± 0.79	-52.54 ± 1.10	-54.53 ± 0.71	-59.54 ± 0.75
7994.5486	-60.21 ± 0.80	-50.66 ± 0.97	-50.63 ± 1.05	-56.28 ± 0.68	-56.54 ± 1.00
7995.4308	-61.58 ± 0.94	-61.47 ± 0.92	-60.25 ± 1.26	-57.72 ± 1.25	-61.66 ± 1.45
7995.5660	-66.10 ± 0.90	-65.87 ± 1.03	-61.57 ± 1.22	-62.44 ± 1.06	-57.12 ± 1.97
8000.4166	-64.29 ± 1.37	-65.41 ± 1.63	-58.90 ± 1.25	-62.22 ± 1.09	-62.60 ± 2.05
8001.4203	-62.49 ± 0.85	-60.21 ± 1.13	-59.02 ± 0.95	-58.62 ± 1.23	-62.94 ± 1.36
8001.4630	-62.03 ± 0.77	-60.04 ± 1.09	-58.71 ± 0.96	-59.33 ± 1.14	-63.84 ± 1.20
8001.5059	-61.96 ± 1.00	-64.81 ± 1.19	-58.81 ± 1.11	-61.40 ± 1.24	-61.18 ± 1.72
8004.4185	-52.84 ± 0.63	-52.21 ± 0.83	-51.26 ± 0.68	-51.29 ± 0.68	-52.08 ± 0.82
8009.4014	-58.30 ± 0.61	-59.99 ± 0.91	-57.61 ± 0.74	-62.42 ± 0.69	-57.01 ± 0.87
8009.4070	-65.11 ± 0.73	-64.44 ± 0.82	-62.37 ± 0.68	-59.12 ± 0.70	-68.52 ± 1.06
8009.4496	-64.72 ± 0.73	-64.84 ± 0.92	-58.24 ± 0.97	-62.45 ± 0.74	-66.11 ± 1.42
8009.4922	-66.44 ± 0.71	-62.22 ± 0.79	-59.31 ± 0.80	-61.29 ± 0.52	-65.19 ± 0.99
8011.3676	-65.64 ± 1.14	-64.07 ± 1.14	-59.69 ± 1.18	-64.15 ± 0.80	-65.53 ± 1.36
8011.4101	-66.81 ± 0.90	-65.75 ± 0.88	-62.12 ± 1.06	-64.53 ± 0.70	-72.92 ± 1.48
8011.4527	-67.84 ± 1.06	-65.08 ± 0.99	-62.11 ± 1.10	-65.11 ± 0.80	-72.33 ± 1.71
8011.4954	-65.84 ± 0.85	-63.36 ± 0.87	-60.17 ± 1.11	-64.01 ± 0.75	-68.87 ± 1.29
8012.3550	-61.82 ± 0.53	-56.42 ± 0.75	-55.25 ± 0.71	-58.90 ± 0.45	-58.03 ± 0.93
8012.4830	-58.96 ± 0.64	-55.22 ± 0.74	-53.28 ± 0.85	-56.87 ± 0.50	-57.49 ± 0.90
8013.3595	-58.48 ± 0.79	-53.33 ± 0.78	-53.38 ± 0.88	-55.56 ± 0.57	-56.99 ± 1.43
8013.4023	-58.27 ± 0.81	-55.36 ± 0.71	-53.18 ± 0.89	-55.93 ± 0.65	-54.84 ± 1.30
8015.3894	-58.53 ± 0.69	-52.68 ± 0.91	-49.85 ± 0.87	-52.76 ± 0.61	-52.51 ± 1.19
8015.4320	-58.60 ± 0.83	-50.51 ± 0.83	-49.30 ± 0.94	-51.69 ± 0.64	-50.81 ± 0.88
8016.1413	-66.12 ± 0.81	-64.42 ± 0.87	-60.64 ± 0.87	...	-55.71 ± 0.95
8016.4588	-62.69 ± 1.01	-59.37 ± 0.95	-57.67 ± 0.99	-61.00 ± 0.89	-63.75 ± 1.34
8016.5013	-61.22 ± 1.13	-60.49 ± 0.90	-56.16 ± 0.97	-63.12 ± 0.90	-62.92 ± 1.64
8017.3428	-66.47 ± 0.80	-64.78 ± 0.85	-60.89 ± 0.86	...	-58.31 ± 0.87
8017.4092	-63.06 ± 0.66	-59.54 ± 0.71	-60.12 ± 0.74	-62.30 ± 0.55	-63.71 ± 1.14
8017.4516	-62.36 ± 0.78	-63.85 ± 0.71	-59.08 ± 0.76	-63.42 ± 0.60	-61.34 ± 1.29
8018.4862	-55.27 ± 0.89	-51.03 ± 1.11	-50.37 ± 1.03	-50.88 ± 0.86	-45.22 ± 1.31
8019.3480	-65.00 ± 0.97	-67.05 ± 1.16	-59.96 ± 1.03	-61.48 ± 1.07	-65.08 ± 1.47
8019.3906	-63.90 ± 0.91	-65.51 ± 1.09	-61.70 ± 1.17	-63.47 ± 1.13	-64.50 ± 1.49
8019.4335	-64.32 ± 1.00	-68.10 ± 1.20	-60.41 ± 1.27	-62.73 ± 1.04	-68.02 ± 1.53
8019.4764	-62.59 ± 0.78	-66.14 ± 1.13	-62.15 ± 1.27	-63.19 ± 1.02	-66.92 ± 1.44
8019.5190	-62.77 ± 0.95	-65.27 ± 1.11	-62.31 ± 1.13	-62.59 ± 1.09	-65.57 ± 1.82
8020.3865	-57.83 ± 0.70	-54.84 ± 0.78	-50.65 ± 0.72	-54.10 ± 0.65	-54.55 ± 0.82
8020.4292	-56.73 ± 0.63	-55.04 ± 0.83	-49.13 ± 0.84	-53.21 ± 0.72	-52.89 ± 1.23
8020.4721	-58.78 ± 1.45	-48.40 ± 1.72	-50.01 ± 1.26	-52.77 ± 0.96	-50.99 ± 1.75
8021.3369	-57.01 ± 0.94	-54.34 ± 0.93	-52.72 ± 1.09	-53.94 ± 1.15	-57.14 ± 1.35
8021.3797	-58.91 ± 1.08	-57.07 ± 1.10	-53.41 ± 1.09	-55.90 ± 1.06	-55.98 ± 1.46
8021.4226	-61.18 ± 0.91	-58.57 ± 0.89	-54.39 ± 1.10	-57.62 ± 1.05	-58.98 ± 1.69
8021.4519	-55.79 ± 0.76	-57.99 ± 0.95	-56.23 ± 0.99	...	-56.08 ± 1.37
8021.4655	-59.66 ± 0.91	-60.73 ± 1.12	-55.07 ± 1.19	-60.03 ± 1.06	-58.26 ± 1.57
8021.5084	-61.64 ± 1.03	-61.38 ± 1.21	-56.72 ± 1.35	-59.17 ± 1.18	-58.61 ± 1.51
8022.4587	-62.95 ± 0.95	-62.02 ± 0.82	-57.50 ± 0.96	-62.70 ± 0.87	-62.99 ± 1.63
8023.3396	-54.73 ± 0.97	-45.73 ± 1.32	-50.86 ± 1.12	-48.72 ± 1.06	-53.01 ± 1.31
8023.4082	-46.83 ± 0.61	-44.44 ± 0.94	-45.82 ± 1.09	-49.59 ± 0.81	-43.68 ± 1.00
8024.3935	-65.22 ± 1.13	-65.43 ± 0.92	-59.85 ± 1.01	-63.90 ± 1.21	-64.52 ± 1.34
8024.4651	-65.55 ± 0.97	-66.03 ± 1.38	-61.15 ± 1.15	-66.76 ± 1.14	-65.41 ± 1.48

Table B1 – continued Radial Velocity Measurements

HJD-2450000	He I 4471	He I 4721	He I 4921	He I 5876	Mg II 4481
8025.3454	-60.95 ± 0.73	-60.17 ± 0.88	-56.76 ± 0.88	-56.95 ± 0.71	-62.62 ± 0.96
8025.3880	-61.85 ± 0.82	-60.91 ± 0.82	-55.28 ± 0.88	-58.75 ± 0.65	-60.96 ± 0.98
8025.4309	-60.04 ± 0.74	-58.13 ± 0.77	-53.33 ± 0.92	-54.98 ± 0.63	-60.80 ± 1.05
8025.4739	-59.74 ± 0.85	-58.03 ± 1.16	-53.13 ± 1.14	-55.84 ± 0.61	-56.91 ± 1.34
8026.3308	-55.28 ± 0.89	-55.76 ± 1.23	-48.69 ± 1.14	-48.26 ± 1.02	-53.56 ± 1.88
8026.3733	-55.21 ± 1.04	-57.18 ± 1.33	-47.25 ± 1.19	-48.93 ± 1.02	-50.56 ± 1.47
8026.4026	-46.67 ± 0.68	-47.68 ± 0.82	-49.02 ± 1.11	-50.81 ± 1.01	-45.19 ± 1.19
8026.4160	-56.34 ± 1.08	-55.29 ± 1.14	-49.90 ± 1.28	-47.06 ± 1.06	-54.35 ± 1.42
8030.2831	-64.00 ± 0.52	-66.52 ± 0.60	-65.26 ± 0.90	...	-66.89 ± 0.83
8031.3385	-57.69 ± 1.33	-50.55 ± 1.37	-47.91 ± 1.15	...	-54.95 ± 2.30
8032.3226	-67.90 ± 1.13	-68.60 ± 0.94	-61.54 ± 1.10	-65.86 ± 0.99	-70.08 ± 1.66
8032.4526	-60.75 ± 0.92	-64.41 ± 0.86	-62.41 ± 1.10	...	-64.32 ± 1.25
8033.3153	-61.18 ± 0.83	-61.35 ± 1.01	-56.86 ± 0.76	-56.48 ± 0.56	-65.10 ± 1.13
8033.3578	-61.67 ± 0.77	-62.38 ± 0.88	-55.36 ± 0.80	-56.95 ± 0.53	-61.90 ± 1.46
8033.4005	-61.86 ± 0.81	-59.54 ± 1.01	-55.47 ± 0.83	-55.64 ± 0.66	-61.27 ± 1.38
8035.3558	-66.19 ± 0.92	-68.63 ± 1.04	-62.08 ± 1.05	-64.43 ± 1.03	-73.77 ± 1.57
8035.3985	-67.73 ± 0.91	-68.71 ± 0.96	-60.66 ± 0.81	-64.22 ± 0.86	-70.32 ± 1.22
8035.4401	-58.02 ± 0.70	-61.72 ± 0.89	-60.94 ± 0.99	-65.50 ± 0.79	-61.53 ± 0.95
8035.4416	-66.66 ± 1.05	-68.52 ± 0.97	-61.06 ± 0.81	...	-73.47 ± 1.53
8036.2965	-59.71 ± 0.91	-54.78 ± 1.00	-51.70 ± 1.05	-49.01 ± 0.69	-57.59 ± 1.48
8036.3393	-56.96 ± 0.84	-53.94 ± 1.27	-48.75 ± 1.02	-50.33 ± 0.71	-57.85 ± 1.47
8036.3827	-57.46 ± 0.91	-55.23 ± 1.15	-49.46 ± 1.03	-49.29 ± 0.84	-53.07 ± 1.38
8036.4258	-56.06 ± 1.06	-51.11 ± 1.22	-48.36 ± 0.95	-49.45 ± 0.80	-58.71 ± 1.63
8036.4297	-49.64 ± 0.72	-50.42 ± 0.86	-47.94 ± 1.00	...	-48.49 ± 1.14
8036.4688	-58.34 ± 0.92	-54.68 ± 1.13	-45.28 ± 1.04	-49.64 ± 0.81	-55.20 ± 1.33
8037.2970	-69.01 ± 1.27	-66.62 ± 1.18	-61.56 ± 1.23	-60.40 ± 1.19	-65.45 ± 1.86
8037.3214	-58.31 ± 0.86	-61.55 ± 0.93	-59.01 ± 1.05	-61.82 ± 1.23	-60.38 ± 1.55
8037.3255	-65.07 ± 1.11	-71.27 ± 1.09	-62.58 ± 1.33	...	-65.54 ± 1.95
8037.3684	-67.34 ± 1.03	-67.98 ± 1.30	-63.99 ± 1.22	-64.00 ± 1.14	-71.35 ± 2.13
8037.4113	-65.90 ± 0.89	-68.96 ± 1.37	-64.06 ± 1.08	-66.54 ± 1.10	-71.59 ± 2.06
8037.4543	-66.96 ± 1.19	-66.53 ± 1.34	-62.69 ± 1.11	-65.78 ± 1.22	-69.78 ± 1.68
8038.3054	-63.08 ± 0.84	-63.32 ± 0.87	-60.04 ± 0.89	-59.86 ± 0.62	-64.73 ± 1.13
8038.3484	-61.96 ± 0.96	-64.22 ± 0.77	-58.71 ± 0.72	-61.10 ± 0.60	-59.34 ± 1.31
8038.3913	-62.14 ± 0.69	-60.46 ± 0.73	-56.48 ± 0.68	-59.12 ± 0.69	-59.45 ± 1.19
8038.4343	-61.53 ± 0.82	-60.96 ± 0.82	-53.07 ± 1.98	-57.40 ± 0.58	-61.90 ± 1.29
8039.2924	-59.43 ± 0.98	-51.94 ± 1.03	-51.10 ± 1.06	-50.01 ± 0.88	-49.52 ± 1.34
8039.3352	-57.25 ± 0.93	-52.29 ± 1.17	-52.15 ± 1.15	-50.80 ± 0.96	-53.42 ± 1.57
8039.3782	-59.75 ± 1.02	-55.87 ± 1.19	-53.00 ± 1.16	-50.87 ± 0.90	-54.49 ± 1.20
8039.4211	-56.30 ± 1.09	-54.86 ± 1.06	-52.69 ± 1.02	-52.39 ± 0.88	-54.49 ± 1.45
8039.4641	-55.40 ± 1.08	-57.36 ± 1.19	-52.10 ± 1.23	-51.45 ± 1.09	-47.50 ± 1.60
8040.3018	-68.40 ± 1.16	-69.31 ± 1.22	-64.29 ± 1.02	-65.76 ± 1.02	-67.58 ± 1.55
8040.3305	-57.11 ± 0.95	-59.50 ± 0.93	-58.41 ± 0.93	-62.03 ± 0.94	-61.86 ± 1.46
8040.3446	-68.71 ± 1.19	-68.56 ± 1.28	-63.75 ± 1.12	-65.17 ± 0.93	-73.39 ± 2.00
8040.3612	-61.04 ± 0.85	-61.99 ± 1.18	-61.28 ± 1.17	...	-65.22 ± 1.84
8040.3876	-65.87 ± 0.96	-69.58 ± 1.19	-62.21 ± 1.10	-67.13 ± 0.80	-74.70 ± 1.37
8040.4306	-65.98 ± 0.96	-73.78 ± 1.03	-64.35 ± 1.01	-66.49 ± 0.89	-72.47 ± 1.26
8041.4267	-59.48 ± 0.69	-55.35 ± 0.82	-50.37 ± 0.88	-51.86 ± 0.66	-51.99 ± 1.10
8042.2766	-62.78 ± 1.04	-57.22 ± 1.31	-56.78 ± 1.19	-55.28 ± 0.95	-59.03 ± 2.12
8042.3477	-61.48 ± 1.10	-59.95 ± 1.20	-59.14 ± 1.09	-58.87 ± 1.01	-64.52 ± 1.32
8042.4189	-62.92 ± 1.23	-62.88 ± 1.19	-56.82 ± 1.09	-59.92 ± 0.95	-64.33 ± 1.85
8042.4236	-52.97 ± 0.80	-54.46 ± 0.76	-53.34 ± 1.09	-55.05 ± 1.14	-55.30 ± 1.36
8043.3350	-66.86 ± 0.78	-65.56 ± 0.75	-60.15 ± 0.74	-64.44 ± 0.55	-67.18 ± 1.12
8043.4325	-54.27 ± 0.46	-56.12 ± 0.51	-54.09 ± 0.66	-57.11 ± 0.53	-55.62 ± 0.79
8044.2988	-57.98 ± 0.93	-52.08 ± 1.18	-50.22 ± 1.19	-49.79 ± 0.87	-47.35 ± 1.27
8044.3556	-57.02 ± 1.08	-54.59 ± 1.38	-48.63 ± 1.13	-50.73 ± 0.83	-51.37 ± 1.24
8044.3986	-55.42 ± 0.85	-51.22 ± 1.26	-48.46 ± 1.08	-51.49 ± 0.90	-49.76 ± 1.55
8045.3590	-67.87 ± 1.08	-70.80 ± 1.18	-62.76 ± 1.14	-64.34 ± 1.04	-75.48 ± 1.79
8046.3191	-60.51 ± 0.66	-59.18 ± 0.87	-55.84 ± 0.72	-55.84 ± 0.64	-60.70 ± 1.23
8046.3905	-60.52 ± 0.83	-56.44 ± 1.03	-53.81 ± 0.89	-55.03 ± 0.59	-53.30 ± 1.05
8050.2637	-64.55 ± 1.17	-66.93 ± 1.43	-58.93 ± 1.21	-63.29 ± 1.05	-66.84 ± 1.91
8050.3657	-67.78 ± 1.14	-67.13 ± 1.41	-59.06 ± 1.22	-64.18 ± 0.97	-67.38 ± 2.60
8051.2719	-62.51 ± 0.69	-64.39 ± 0.66	-58.93 ± 0.65	-63.99 ± 0.64	-65.43 ± 0.97
8051.3430	-63.86 ± 0.63	-61.41 ± 0.60	-58.84 ± 0.70	-61.75 ± 0.68	-66.04 ± 0.95
8051.4002	-61.64 ± 0.56	-61.41 ± 0.74	-58.28 ± 0.66	-59.63 ± 0.60	-62.66 ± 1.10

Table B1 – *continued* Radial Velocity Measurements

HJD-2450000	He I 4471	He I 4721	He I 4921	He I 5876	Mg II 4481
8052.2411	-54.99 ± 0.95	-53.72 ± 1.09	-48.33 ± 1.18	-48.21 ± 0.81	-49.34 ± 1.41
8052.3120	-53.27 ± 0.91	-53.50 ± 1.10	-50.35 ± 1.07	-50.65 ± 0.89	-50.67 ± 1.38
8052.3692	-57.33 ± 0.96	-52.93 ± 1.04	-49.92 ± 0.94	-51.71 ± 0.83	-53.33 ± 1.44
8054.4068	-58.92 ± 0.81	-52.71 ± 0.75	-50.31 ± 0.76	-52.70 ± 0.59	-53.45 ± 0.87
8058.2510	-65.43 ± 0.82	-62.68 ± 0.88	-58.21 ± 1.07	-64.66 ± 1.02	-69.12 ± 1.42
8058.3437	-60.29 ± 0.78	-62.82 ± 1.24	-61.02 ± 1.06	-62.34 ± 1.05	-60.70 ± 1.58
8059.3636	-61.54 ± 0.74	-56.23 ± 0.56	-53.77 ± 0.69	-56.82 ± 0.57	-58.45 ± 0.94
8071.3348	-64.24 ± 0.91	-61.73 ± 0.79	-60.23 ± 1.07	-67.09 ± 0.97	-64.51 ± 1.62
8074.3123	-60.31 ± 0.76	-66.06 ± 0.93	-61.96 ± 0.96	-64.17 ± 0.76	-63.36 ± 1.06
8074.3517	-59.81 ± 0.74	-65.87 ± 0.84	-60.89 ± 1.01	-62.90 ± 0.85	-65.47 ± 1.29
8074.4039	-58.39 ± 0.81	-63.72 ± 0.97	-62.45 ± 0.93	-63.01 ± 0.82	-64.16 ± 1.25
8077.2347	-62.51 ± 0.82	-61.62 ± 0.74	-59.65 ± 0.81	-62.29 ± 0.66	-64.85 ± 0.89
8085.3270	-54.37 ± 0.78	-52.06 ± 0.99	-53.36 ± 0.78	-61.07 ± 0.80	-60.50 ± 1.61
8094.2220	-62.64 ± 0.88	-54.48 ± 0.80	-52.62 ± 1.02	-54.92 ± 0.84	-56.62 ± 1.18
8143.2471	-53.94 ± 0.63	-52.02 ± 0.87	-52.32 ± 0.98	-54.11 ± 0.77	-49.19 ± 1.10
8180.2874	-54.62 ± 0.75	-52.98 ± 1.18	-57.51 ± 1.23	-59.47 ± 0.84	-57.07 ± 1.12
8181.2967	-51.68 ± 1.05	-54.57 ± 1.45	-60.53 ± 1.35	-51.03 ± 1.10	-51.31 ± 1.47
8191.2859	-53.38 ± 0.97	-48.11 ± 1.76	-56.65 ± 1.33	-57.06 ± 0.89	-49.24 ± 1.22
8198.3040	-53.65 ± 0.70	-53.96 ± 1.68	-57.93 ± 1.15	-56.75 ± 0.56	-55.49 ± 1.21
8296.6079	-71.56 ± 1.13	-66.36 ± 1.31	-65.85 ± 1.08	-66.95 ± 1.23	-65.74 ± 1.76
8297.6048	-58.21 ± 0.89	-54.15 ± 0.87	-53.23 ± 0.95	-54.74 ± 0.70	-52.25 ± 1.24
8298.5980	-58.72 ± 1.15	-57.16 ± 1.25	-55.54 ± 1.20	-56.41 ± 1.12	-56.39 ± 1.56
8300.5825	-58.15 ± 1.03	-46.69 ± 0.93	-51.49 ± 1.13	-49.12 ± 1.04	-52.83 ± 1.83
8301.5940	-66.93 ± 1.13	-67.08 ± 1.34	-62.60 ± 1.15	-67.98 ± 1.35	-65.14 ± 1.56
8303.5915	-56.15 ± 0.97	-49.14 ± 0.88	-49.80 ± 1.06	-49.88 ± 1.15	-50.96 ± 1.44
8306.6001	-62.38 ± 1.04	-58.21 ± 1.07	-55.27 ± 1.11	-61.82 ± 1.12	-57.44 ± 1.63
8308.5856	-55.94 ± 0.93	-51.67 ± 0.91	-48.44 ± 1.03	-50.71 ± 0.97	-50.38 ± 1.31
8309.5830	-66.59 ± 0.97	-56.09 ± 0.87	-63.71 ± 0.91	-68.22 ± 1.20	-68.25 ± 1.57
8310.5767	-60.34 ± 0.97	-56.29 ± 0.90	-53.15 ± 0.86	-57.88 ± 0.71	-51.42 ± 1.34
8311.5814	-62.07 ± 1.00	-63.30 ± 0.84	-54.67 ± 0.99	-56.00 ± 1.19	-55.77 ± 1.90
8312.5751	-66.53 ± 0.85	-50.31 ± 0.92	-61.47 ± 0.94	-67.93 ± 1.11	-69.15 ± 1.22
8313.5683	-57.98 ± 0.94	-63.02 ± 0.82	-51.94 ± 1.10	-50.24 ± 0.88	-46.16 ± 1.39
8314.5782	-64.24 ± 0.95	-56.58 ± 0.94	-59.42 ± 0.92	-60.36 ± 1.20	-63.03 ± 1.16
8315.5591	-56.93 ± 0.41	-51.46 ± 2.18	-55.95 ± 0.77	-57.32 ± 0.89	-57.40 ± 1.09
8316.5960	-50.85 ± 0.86	-54.79 ± 1.06	-49.76 ± 1.20	-49.76 ± 0.98	-46.41 ± 1.37
8317.5663	-67.13 ± 1.06	-67.59 ± 0.85	-62.81 ± 1.03	-69.41 ± 1.10	-70.50 ± 1.42
8319.5842	-63.84 ± 0.97	-57.24 ± 1.01	-56.57 ± 1.05	-62.41 ± 1.16	-62.95 ± 1.46
8321.5871	-55.94 ± 1.29	-51.86 ± 1.13	-48.86 ± 1.13	-49.75 ± 0.91	-48.84 ± 1.68
8323.5701	-61.67 ± 0.68	-59.10 ± 0.59	-54.92 ± 0.68	-57.32 ± 0.79	-58.97 ± 1.03
8324.5287	-63.07 ± 1.42	-51.69 ± 1.53	-56.53 ± 1.22	-54.53 ± 1.28	-46.72 ± 2.47
8324.6068	-60.01 ± 0.98	-56.89 ± 0.95	-55.76 ± 1.16	-57.66 ± 1.13	-56.24 ± 1.98
8325.5835	-67.27 ± 0.92	-64.55 ± 1.00	-63.35 ± 0.99	-67.53 ± 1.20	-69.87 ± 1.50
8328.5539	-64.40 ± 1.38	-58.95 ± 1.19	-57.53 ± 0.85	-58.59 ± 0.95	-54.96 ± 2.12
8329.5320	-55.05 ± 1.11	-53.59 ± 1.04	-51.22 ± 1.19	-48.02 ± 1.12	-52.83 ± 1.32
8331.5225	-58.55 ± 0.93	-53.00 ± 0.79	-50.43 ± 0.74	-53.39 ± 1.04	-50.44 ± 1.50
8332.5685	-60.35 ± 1.21	-57.18 ± 1.16	-53.98 ± 1.18	-57.90 ± 1.44	-60.23 ± 1.93
8333.5573	-65.18 ± 1.06	-63.91 ± 0.76	-58.55 ± 0.91	-63.70 ± 1.25	-62.99 ± 1.39
8334.5957	-57.36 ± 0.94	-52.95 ± 0.98	-47.27 ± 0.99	-49.64 ± 1.08	-50.32 ± 1.27
8335.5596	-65.71 ± 1.08	-66.10 ± 0.92	-60.90 ± 1.18	-65.41 ± 1.44	-65.38 ± 1.74
8337.5458	-56.93 ± 1.26	-53.96 ± 1.08	-53.06 ± 1.32	-49.32 ± 1.21	-52.58 ± 1.40
8339.5539	-56.34 ± 0.85	-51.93 ± 0.86	-54.38 ± 0.88	-52.70 ± 0.88	-49.62 ± 1.54
8341.5381	-57.71 ± 1.11	-60.34 ± 1.05	-54.39 ± 1.13	-58.67 ± 1.11	-56.39 ± 2.18
8345.5266	-57.80 ± 0.95	-54.76 ± 0.92	-58.37 ± 1.19	-56.58 ± 1.44	-56.30 ± 1.93
8346.5031	-62.16 ± 0.99	-63.45 ± 0.72	...	-58.94 ± 1.18	-65.02 ± 1.69
8346.5752	-57.92 ± 1.00	-59.21 ± 0.90	-58.18 ± 0.97	-58.96 ± 1.06	-62.07 ± 1.48
8346.6401	-57.51 ± 1.14	-60.26 ± 1.14	-56.12 ± 0.97	-57.58 ± 1.07	-58.27 ± 1.45
8347.4832	-49.37 ± 0.65	-46.70 ± 0.90	...	-49.12 ± 0.93	-47.66 ± 1.15
8349.4227	-52.15 ± 0.65	-58.30 ± 0.83	-52.43 ± 0.89	-50.02 ± 1.37	-53.73 ± 1.20
8349.5637	-56.61 ± 1.41	-52.24 ± 1.09	...	-50.04 ± 0.97	-56.43 ± 1.91
8350.4430	-52.02 ± 0.66	-51.08 ± 1.14	-52.45 ± 1.37	-52.50 ± 1.00	-50.70 ± 1.11
8350.4797	-59.79 ± 1.32	-53.06 ± 1.61	...	-56.87 ± 1.14	-53.05 ± 1.70
8350.5061	-54.03 ± 0.64	-50.56 ± 0.98	...	-54.37 ± 0.99	-52.72 ± 1.12
8350.5689	-53.93 ± 0.68	-50.17 ± 1.08	...	-55.97 ± 0.96	-52.93 ± 1.26
8351.5541	-67.65 ± 0.98	-63.46 ± 0.83	...	-62.88 ± 1.25	-65.83 ± 1.37

Table B1 – continued Radial Velocity Measurements

HJD-2450000	He I 4471	He I 4721	He I 4921	He I 5876	Mg II 4481
8352.4421	-50.81 ± 0.60	-54.42 ± 1.06	...	-45.54 ± 1.13	-51.53 ± 1.11
8352.5396	-46.92 ± 1.69	-52.17 ± 1.55	-48.07 ± 1.53	-45.26 ± 1.39	-63.12 ± 2.15
8353.4969	-60.32 ± 0.69	-63.61 ± 1.30	...	-62.97 ± 1.15	-63.72 ± 1.59
8357.4494	-51.11 ± 0.49	-53.00 ± 0.87	-54.25 ± 0.79	-50.70 ± 0.64	-52.38 ± 0.85
8357.5413	-54.69 ± 0.83	-52.82 ± 0.95	-52.33 ± 1.00	-50.63 ± 0.69	-53.58 ± 1.48
8357.5837	-56.57 ± 1.10	-49.23 ± 1.02	-48.12 ± 0.98	-48.97 ± 0.77	-45.06 ± 1.39
8358.4607	-57.64 ± 0.84	-54.81 ± 0.74	...	-52.86 ± 0.76	-55.82 ± 1.37
8358.5246	-57.44 ± 0.78	-50.79 ± 0.79	...	-54.72 ± 0.90	-66.70 ± 1.43
8359.4581	-70.77 ± 1.19	-66.01 ± 1.48	-69.47 ± 0.94	-72.64 ± 1.23	-68.26 ± 2.01
8362.4822	-58.72 ± 0.54	-61.06 ± 0.71	-61.75 ± 0.82	-64.45 ± 0.65	-57.12 ± 1.00
8363.4887	-58.53 ± 1.13	-52.30 ± 1.16	-51.42 ± 1.28	-50.98 ± 1.13	-58.02 ± 1.58
8363.5459	-58.44 ± 1.19	-54.88 ± 1.52	-54.00 ± 1.25	-53.00 ± 0.81	-56.57 ± 1.54
8364.5478	-60.47 ± 0.87	-67.68 ± 0.95	-63.02 ± 1.17	-65.50 ± 0.83	-63.08 ± 1.32
8365.4541	-61.65 ± 0.68	-52.59 ± 0.83	-54.30 ± 0.84	-56.20 ± 0.57	-57.08 ± 1.03
8366.4522	-54.77 ± 0.75	-60.10 ± 1.16	-57.07 ± 1.10	-54.07 ± 1.03	-57.18 ± 1.03
8368.4562	-51.74 ± 0.70	-49.34 ± 0.74	-48.61 ± 1.25	-51.23 ± 0.74	-50.12 ± 1.01
8369.4500	-56.97 ± 0.74	-61.05 ± 0.71	-58.81 ± 0.97	-59.12 ± 0.88	-63.13 ± 1.22
8370.4549	-64.72 ± 0.62	-58.78 ± 0.70	-59.28 ± 0.88	-63.72 ± 0.70	-57.99 ± 1.15
8371.4276	-53.98 ± 0.86	-58.09 ± 1.72	-55.17 ± 1.52	-54.42 ± 1.02	-45.19 ± 1.39
8372.4785	-58.35 ± 0.70	-61.71 ± 0.95	-59.95 ± 1.05	-59.19 ± 1.07	-65.39 ± 1.25
8372.4872	-66.88 ± 0.89	-64.08 ± 0.96	-61.41 ± 0.89	-63.61 ± 1.00	-68.46 ± 1.38
8373.4747	-61.26 ± 0.67	-53.97 ± 0.90	-52.20 ± 1.00	-60.11 ± 0.72	-56.95 ± 1.04
8373.5119	-52.06 ± 0.56	-54.84 ± 1.00	-54.96 ± 0.90	-55.22 ± 0.62	-48.95 ± 1.08
8376.4731	-53.22 ± 0.73	-50.06 ± 0.89	-49.18 ± 1.07	-53.94 ± 0.71	-48.66 ± 1.09
8377.4148	-65.97 ± 1.33	-63.44 ± 0.91	-60.40 ± 1.05	-63.72 ± 1.05	-63.55 ± 1.95
8377.4921	-59.04 ± 0.63	-62.82 ± 0.98	-59.11 ± 1.00	-63.79 ± 0.75	-66.21 ± 1.16
8378.5057	-52.10 ± 0.43	-53.41 ± 0.56	-53.26 ± 0.89	-53.40 ± 0.63	-50.75 ± 0.78
8379.5082	-60.93 ± 0.90	-57.37 ± 1.13	-56.86 ± 1.09	-59.71 ± 0.97	-56.65 ± 1.86
8385.5020	-60.37 ± 0.73	-65.06 ± 0.76	-60.37 ± 1.06	-62.98 ± 0.78	-62.83 ± 1.41
8386.4720	-53.91 ± 0.46	-53.61 ± 0.72	-51.80 ± 0.78	-55.10 ± 0.60	-54.49 ± 0.83
8387.4332	-55.06 ± 0.68	-58.61 ± 0.90	-53.56 ± 1.10	-57.06 ± 0.92	-54.76 ± 1.17
8387.4548	-52.02 ± 0.81	-53.89 ± 0.99	-51.46 ± 1.06	...	-50.91 ± 1.60
8388.4121	-58.53 ± 0.57	-57.31 ± 0.87	-57.06 ± 0.85	-61.84 ± 0.85	-62.30 ± 1.12
8389.4065	-49.95 ± 0.58	-53.04 ± 0.91	-48.05 ± 0.98	-50.76 ± 0.97	-48.49 ± 1.15
8389.4521	-58.23 ± 1.04	-52.53 ± 1.08	-50.76 ± 1.01	-55.87 ± 0.75	-54.54 ± 1.30
8390.4486	-65.69 ± 1.02	-63.92 ± 0.91	-61.58 ± 1.30	-65.17 ± 1.06	-62.42 ± 1.57
8393.4286	-59.45 ± 0.71	-62.41 ± 0.81	-60.00 ± 1.10	-63.38 ± 0.76	-64.03 ± 1.13
8394.3794	-64.96 ± 1.24	-59.25 ± 1.06	-53.17 ± 1.08	-52.99 ± 0.94	-61.53 ± 2.06
8395.4098	-55.27 ± 0.70	-57.23 ± 0.98	-58.23 ± 1.13	-53.83 ± 1.07	-54.39 ± 1.38
8395.4192	-61.69 ± 0.94	-58.00 ± 0.75	-55.98 ± 1.15	-58.75 ± 0.84	-59.54 ± 1.57
8396.4035	-58.47 ± 0.43	-61.47 ± 0.63	-58.12 ± 0.74	-63.23 ± 0.75	-59.45 ± 0.96
8396.4498	-64.34 ± 0.79	-59.91 ± 0.75	-59.13 ± 0.88	-61.38 ± 0.72	-65.33 ± 1.45
8397.4057	-50.10 ± 0.53	-53.37 ± 0.76	-50.84 ± 0.99	-51.84 ± 1.01	-47.78 ± 1.03
8397.4305	-59.49 ± 1.40	-56.32 ± 1.08	-56.68 ± 1.08	-50.62 ± 0.82	-57.55 ± 1.91
8398.3767	-65.48 ± 1.69	-63.36 ± 1.61	-60.12 ± 1.39	-62.87 ± 1.20	-65.29 ± 2.67
8400.3886	-60.00 ± 0.88	-50.64 ± 1.08	-54.46 ± 1.17	-55.08 ± 1.04	-58.43 ± 1.58
8400.4563	-53.87 ± 0.61	-57.45 ± 0.83	-55.94 ± 1.02	-55.30 ± 1.02	-49.57 ± 1.03
8401.4382	-68.15 ± 1.21	-62.28 ± 0.92	-64.82 ± 1.11	-67.40 ± 1.11	-67.87 ± 2.00
8401.4578	-60.38 ± 0.68	-62.30 ± 0.91	-60.64 ± 0.91	-62.70 ± 0.96	-61.93 ± 1.25
8404.4002	-58.07 ± 1.19	-59.17 ± 0.93	-58.09 ± 0.91	-57.58 ± 0.98	-64.68 ± 1.34
8405.3428	-59.00 ± 1.34	-50.92 ± 0.91	-51.14 ± 1.21	-51.28 ± 1.05	-54.34 ± 1.43
8407.5264	-50.57 ± 0.54	-54.72 ± 0.84	-53.65 ± 0.92	-44.94 ± 0.96	-52.34 ± 1.08
8409.3058	-69.22 ± 1.52	-63.65 ± 1.20	-66.54 ± 1.23	-65.43 ± 1.09	-67.42 ± 2.48
8409.5829	-57.76 ± 0.54	-62.12 ± 0.89	-58.72 ± 0.67	-58.98 ± 0.97	-57.68 ± 1.10
8410.4964	-50.42 ± 0.56	-54.96 ± 0.74	-49.32 ± 1.09	-45.30 ± 0.94	-52.33 ± 1.01
8411.3838	-68.74 ± 1.04	-65.25 ± 1.15	-62.75 ± 1.27	-65.21 ± 0.86	-62.32 ± 1.74
8411.4720	-61.35 ± 0.70	-62.06 ± 1.07	-62.26 ± 1.08	-68.25 ± 0.77	-63.68 ± 1.26
8412.4934	-54.64 ± 0.44	-55.02 ± 0.64	-54.55 ± 0.76	-56.70 ± 0.49	-52.31 ± 1.06
8413.4110	-55.79 ± 1.50	-52.82 ± 1.05	-52.98 ± 0.95	-50.94 ± 0.72	-61.15 ± 1.29
8416.4004	-59.95 ± 1.17	-58.66 ± 1.03	-58.28 ± 1.15	-53.96 ± 0.84	-69.16 ± 1.80
8417.3037	-65.66 ± 0.81	-61.80 ± 0.94	-67.30 ± 1.01	-68.72 ± 0.81	-67.54 ± 1.31
8429.3295	-58.30 ± 1.31	-53.15 ± 1.11	-54.86 ± 1.09	-54.96 ± 0.87	-54.71 ± 1.32
8432.2991	-61.03 ± 1.24	-59.81 ± 1.00	-56.88 ± 1.35	-55.19 ± 1.07	-59.37 ± 1.53
8434.2726	-64.25 ± 0.93	-54.62 ± 1.00	-55.63 ± 1.47	-58.54 ± 0.85	-54.19 ± 1.22
8436.3603	-62.94 ± 0.68	-52.72 ± 0.86	-53.65 ± 0.92	-55.89 ± 0.83	-54.60 ± 1.22

Table B1 – *continued* Radial Velocity Measurements

HJD-2450000	He I 4471	He I 4721	He I 4921	He I 5876	Mg II 4481
8437.3468	-63.77 ± 0.97	-55.30 ± 1.05	-58.69 ± 1.20	-62.00 ± 0.89	-62.63 ± 1.33
8438.3249	-60.60 ± 0.75	-60.70 ± 0.85	-59.04 ± 1.01	-56.58 ± 0.86	-60.99 ± 1.13
8438.4520	-52.80 ± 1.91	-56.86 ± 1.78	-56.99 ± 1.26	-57.27 ± 1.07	-63.54 ± 2.05
8441.2979	-59.39 ± 0.92	-56.51 ± 0.83	-54.77 ± 0.85	-53.84 ± 0.77	-57.97 ± 1.33
8441.4473	-50.76 ± 0.38	-54.93 ± 0.56	-52.27 ± 0.88	-52.98 ± 0.49	-52.57 ± 0.71
8443.4107	-59.65 ± 0.60	-63.28 ± 1.06	-58.90 ± 0.95	-62.40 ± 0.55	-61.31 ± 1.36
8444.3055	-51.97 ± 0.44	-55.46 ± 0.93	-49.62 ± 1.01	-53.77 ± 0.45	-49.79 ± 0.81
8451.3159	-66.29 ± 0.81	-62.58 ± 0.94	-61.25 ± 0.94	-63.34 ± 0.87	-64.27 ± 1.41
8454.2752	-68.39 ± 1.01	-61.29 ± 0.74	-58.85 ± 0.88	-60.97 ± 0.61	-64.40 ± 1.58
8457.3021	-60.43 ± 0.78	-53.97 ± 0.88	-54.71 ± 0.95	-57.04 ± 0.69	-59.18 ± 1.46
8463.4456	-52.82 ± 0.61	-54.47 ± 1.11	-52.63 ± 1.10	-53.08 ± 0.97	-49.41 ± 1.10
8479.2329	-49.81 ± 1.02	-57.84 ± 1.17	-57.20 ± 1.23	-57.78 ± 0.95	-51.58 ± 1.55
8480.2246	-63.05 ± 0.89	-61.30 ± 1.13	-60.59 ± 1.16	-63.47 ± 0.74	-66.66 ± 1.60
8480.2827	-53.77 ± 0.52	-59.06 ± 0.82	-55.89 ± 1.05	-59.95 ± 0.59	-57.75 ± 1.70
8483.2416	-59.67 ± 0.99	-56.03 ± 1.08	-54.60 ± 0.82	-57.08 ± 0.76	-58.85 ± 1.50
8487.3411	-57.64 ± 0.92	-62.33 ± 1.40	-59.60 ± 1.17	-63.39 ± 0.90	-62.69 ± 1.72
8492.4135	-56.94 ± 0.79	-58.14 ± 1.05	-55.83 ± 1.21	-60.80 ± 0.90	-59.22 ± 1.30
8499.2476	-50.02 ± 0.61	-52.19 ± 0.80	-49.46 ± 0.82	-50.92 ± 0.63	-49.66 ± 1.05
8509.2493	-54.48 ± 0.67	-57.00 ± 0.83	-55.45 ± 0.82	-58.33 ± 0.43	-57.10 ± 0.98
8520.2811	-50.83 ± 1.06	-49.23 ± 1.31	-52.12 ± 1.38	-50.01 ± 0.77	-52.40 ± 1.32
8521.2674	-58.94 ± 1.00	-59.49 ± 1.73	-62.03 ± 1.14	-64.50 ± 0.98	-59.82 ± 2.04
8528.2736	-50.71 ± 0.61	-45.71 ± 1.16	-49.73 ± 0.97	-47.21 ± 0.86	-49.21 ± 1.07
8529.2945	-65.68 ± 0.93	-61.77 ± 1.26	-67.72 ± 1.03	-69.48 ± 0.92	-70.65 ± 1.47
8530.2771	-49.53 ± 0.63	-48.80 ± 0.77	-48.68 ± 0.84	-50.14 ± 0.49	-51.57 ± 0.97
8531.2738	-47.52 ± 0.88	-46.40 ± 1.28	-49.15 ± 1.39	-49.38 ± 0.94	-48.67 ± 1.71
8532.2693	-62.84 ± 0.77	-65.10 ± 1.29	-65.35 ± 0.92	-65.46 ± 0.68	-66.12 ± 1.10
8533.2702	-56.21 ± 0.70	-54.98 ± 0.97	-52.82 ± 0.86	-54.39 ± 0.69	-54.41 ± 0.91
8539.3181	-56.42 ± 0.78	-59.72 ± 0.93	-56.63 ± 1.38	-55.94 ± 0.98	-58.39 ± 1.27
8540.3253	-59.41 ± 0.51	-61.04 ± 0.62	-59.61 ± 0.96	-62.63 ± 0.58	-60.08 ± 1.03
8541.3233	-48.24 ± 0.72	-49.74 ± 0.80	-47.28 ± 1.02	-50.41 ± 0.79	-47.14 ± 0.85
8542.3143	-61.07 ± 0.91	-62.91 ± 1.22	-60.00 ± 1.21	-63.01 ± 0.99	-66.47 ± 1.70
8553.3259	-59.48 ± 0.62	-64.83 ± 0.94	-58.27 ± 0.79	-60.63 ± 0.81	-61.00 ± 1.32
8676.5924	-61.64 ± 0.83	-52.58 ± 1.04	-55.87 ± 0.84	-58.36 ± 1.13	-59.45 ± 1.74
8677.5842	-59.10 ± 0.88	-54.74 ± 0.93	-52.15 ± 1.15	-55.15 ± 1.06	-53.62 ± 1.54
8680.6004	-61.91 ± 0.91	-58.51 ± 1.11	-56.03 ± 1.23	-59.21 ± 1.09	-61.19 ± 1.46
8686.5961	-63.37 ± 0.77	-59.57 ± 0.96	-57.74 ± 1.14	-61.68 ± 1.19	-64.06 ± 1.49
8687.5859	-56.90 ± 0.76	-52.52 ± 0.74	-50.76 ± 0.85	-51.87 ± 0.87	-51.77 ± 1.10
8690.6078	-56.41 ± 0.98	-49.67 ± 0.97	-50.82 ± 0.97	-52.01 ± 1.13	-51.51 ± 1.40
8693.5849	-54.73 ± 0.70	-55.14 ± 0.98	-54.40 ± 1.14	-54.88 ± 0.98	-52.95 ± 1.10
8696.6177	-63.87 ± 1.21	-59.62 ± 1.38	-56.73 ± 1.18	-60.82 ± 1.31	-58.74 ± 2.09
8698.5910	-57.99 ± 0.95	-52.22 ± 0.83	-51.89 ± 0.98	-54.24 ± 1.01	-54.96 ± 1.42
8699.5915	-63.00 ± 0.99	-59.66 ± 1.10	-59.03 ± 0.99	-65.08 ± 1.04	-62.90 ± 1.55
8700.5591	-58.32 ± 0.73	-52.58 ± 0.69	-49.67 ± 0.93	-53.73 ± 0.92	-51.77 ± 1.16
8701.5719	-64.30 ± 1.21	-58.77 ± 1.00	-54.92 ± 1.05	-59.02 ± 1.31	-57.47 ± 1.57
8703.5938	-61.97 ± 1.71	-46.99 ± 1.37	-47.71 ± 1.22	-50.93 ± 1.08	-51.01 ± 1.93
8704.5909	-60.56 ± 1.07	-62.23 ± 0.86	-57.28 ± 1.02	-63.02 ± 1.33	-60.58 ± 1.49
8706.5683	-58.82 ± 0.92	-55.22 ± 0.85	-53.39 ± 1.14	-53.91 ± 1.29	-52.31 ± 1.36
8710.5353	-63.55 ± 1.23	-58.72 ± 1.18	-56.40 ± 0.96	-60.65 ± 0.96	-60.94 ± 1.96
8711.5316	-57.61 ± 0.96	-51.39 ± 0.87	-51.81 ± 1.02	-52.54 ± 0.87	-54.63 ± 1.36
8712.5425	-63.81 ± 1.04	-62.62 ± 1.04	-60.04 ± 0.97	-64.98 ± 1.06	-66.21 ± 1.39
8713.5377	-60.12 ± 0.62	-56.83 ± 0.59	-55.68 ± 0.88	-58.16 ± 0.69	-59.15 ± 1.04
8716.6439	-50.09 ± 0.68	-53.03 ± 0.87	-49.11 ± 0.91	-49.14 ± 0.86	-49.49 ± 1.24
8717.6205	-58.34 ± 0.86	-60.60 ± 1.12	-58.38 ± 1.17	-63.24 ± 1.07	-62.50 ± 1.48
8719.5512	-57.29 ± 0.95	-53.29 ± 0.98	-55.39 ± 1.24	-54.35 ± 1.09	-58.82 ± 1.52
8720.4803	-65.57 ± 0.92	-63.48 ± 0.85	-60.19 ± 0.97	-66.91 ± 0.97	-65.15 ± 1.49
8721.5096	-58.91 ± 0.66	-52.46 ± 0.75	-51.76 ± 0.99	-54.37 ± 0.66	-54.69 ± 0.98
8721.6073	-50.33 ± 0.78	-56.78 ± 1.95	-48.79 ± 1.01	-50.68 ± 0.96	-52.69 ± 1.21
8722.5356	-64.17 ± 1.05	-58.15 ± 0.93	-56.64 ± 0.95	-60.46 ± 1.17	-57.29 ± 1.64
8725.4894	-64.17 ± 0.92	-62.29 ± 0.87	-61.95 ± 1.00	-63.79 ± 1.34	-65.40 ± 1.38
8726.4970	-59.41 ± 0.83	-56.88 ± 0.73	-54.40 ± 0.87	-55.43 ± 0.91	-56.76 ± 1.49
8729.4954	-61.56 ± 0.94	-51.40 ± 0.92	-52.19 ± 1.16	-53.41 ± 0.91	-54.08 ± 1.25
8730.5079	-68.22 ± 1.16	-57.15 ± 1.05	-61.14 ± 0.99	-60.62 ± 1.32	-58.18 ± 2.07
8731.4839	-64.60 ± 0.75	-59.14 ± 0.65	-57.84 ± 0.97	-61.06 ± 0.85	-60.55 ± 1.03
8732.5264	-56.58 ± 1.15	-53.32 ± 1.15	-51.49 ± 1.17	-52.24 ± 1.11	-51.26 ± 1.66
8738.4556	-67.34 ± 0.94	-61.34 ± 0.93	-63.69 ± 1.06	-67.59 ± 1.30	-67.60 ± 1.63

Table B1 – continued Radial Velocity Measurements

HJD-2450000	He I 4471	He I 4721	He I 4921	He I 5876	Mg II 4481
8739.4935	-60.49 ± 0.68	-56.86 ± 0.64	-53.48 ± 0.84	-59.61 ± 0.66	-58.26 ± 0.89
8740.4619	-59.24 ± 0.94	-52.40 ± 0.87	-52.70 ± 1.06	-54.79 ± 0.93	-53.06 ± 1.18
8742.4559	-58.87 ± 0.67	-53.84 ± 0.67	-51.67 ± 0.91	-53.43 ± 0.78	-52.47 ± 0.82
8743.4694	-63.36 ± 1.04	-60.62 ± 0.90	-58.40 ± 1.02	-61.40 ± 1.13	-60.70 ± 1.64
8744.4488	-64.31 ± 0.77	-60.98 ± 0.66	-58.33 ± 0.74	-64.26 ± 0.83	-64.45 ± 0.93
8746.4304	-64.14 ± 1.23	-65.46 ± 1.25	-62.37 ± 1.09	-63.96 ± 1.26	-65.45 ± 1.89
8755.4179	-59.12 ± 0.79	-52.74 ± 0.67	-51.58 ± 0.93	-54.99 ± 0.73	-54.21 ± 1.15
8762.4578	-69.92 ± 0.97	-66.25 ± 0.93	-65.11 ± 0.84	-69.45 ± 0.78	-65.83 ± 1.48
8763.4293	-47.39 ± 0.66	-51.71 ± 1.11	-50.16 ± 1.49	-45.14 ± 0.87	-47.92 ± 1.50
8764.4331	-66.22 ± 0.91	-60.82 ± 1.03	-59.94 ± 0.94	-62.96 ± 0.80	-60.35 ± 1.47
8766.3172	-49.41 ± 0.64	-52.01 ± 0.93	-49.28 ± 1.34	-44.89 ± 0.87	-50.91 ± 1.27
8766.3652	-50.96 ± 0.80	-50.60 ± 1.23	-49.33 ± 1.19	-46.26 ± 0.83	-52.50 ± 1.25
8766.4357	-56.33 ± 1.05	-53.18 ± 0.90	-51.43 ± 1.19	-48.63 ± 0.93	-53.83 ± 1.25
8767.3710	-68.45 ± 1.02	-63.17 ± 0.90	-64.60 ± 1.06	-69.49 ± 0.81	-67.73 ± 1.13
8767.3740	-62.31 ± 0.96	-66.68 ± 1.00	-63.69 ± 1.03	-70.98 ± 0.87	-67.65 ± 1.42
8767.4553	-68.93 ± 1.13	-66.34 ± 1.15	-63.56 ± 1.01	-69.30 ± 0.72	-66.64 ± 1.40
8768.3466	-62.02 ± 0.73	-54.97 ± 0.72	-57.30 ± 0.97	-58.91 ± 0.65	-54.29 ± 0.89
8768.3660	-54.75 ± 0.70	-56.34 ± 1.06	-55.60 ± 1.10	-54.11 ± 0.98	-52.88 ± 1.16
8768.4380	-60.06 ± 0.90	-52.48 ± 0.85	-53.35 ± 0.96	-55.93 ± 0.63	-54.65 ± 0.79
8769.3668	-50.04 ± 0.84	-54.92 ± 1.29	-54.23 ± 1.10	-43.37 ± 1.38	-61.49 ± 1.42
8769.3947	-57.77 ± 1.08	-56.58 ± 0.86	-54.80 ± 1.13	-50.01 ± 1.29	-60.98 ± 1.32
8770.3383	-71.19 ± 0.95	-66.96 ± 0.76	-68.31 ± 0.87	-71.77 ± 0.91	-68.63 ± 1.07
8770.4298	-71.10 ± 0.78	-64.55 ± 0.67	-66.15 ± 0.82	-70.33 ± 0.80	-66.37 ± 0.90
8776.3572	-63.69 ± 1.17	-57.49 ± 1.00	-56.13 ± 1.33	-60.21 ± 1.01	-51.65 ± 1.37
8778.3498	-58.76 ± 0.61	-58.54 ± 1.11	-61.70 ± 0.72	-57.98 ± 0.73	-62.98 ± 0.76
8778.5186	-56.30 ± 0.61	-55.38 ± 0.67	-62.74 ± 1.40	-61.25 ± 0.61	-57.79 ± 0.73
8778.6023	-58.22 ± 0.66	-53.59 ± 1.30	-58.02 ± 1.07	-60.21 ± 0.69	-54.31 ± 0.78
8778.6642	-59.03 ± 0.79	-60.86 ± 1.57	-56.80 ± 1.80	-59.10 ± 1.04	-55.81 ± 1.56
8782.3610	-60.60 ± 1.26	-56.92 ± 0.97	-59.44 ± 1.48	-56.22 ± 0.78	-53.14 ± 1.38
8782.4243	-61.98 ± 1.13	-58.28 ± 0.86	-58.04 ± 1.41	-58.15 ± 0.90	-55.87 ± 1.28
8783.3183	-62.84 ± 1.06	-65.89 ± 0.91	-62.10 ± 0.95	-56.59 ± 1.05	-60.84 ± 1.33
8783.3724	-58.27 ± 0.68	-62.90 ± 0.98	-59.95 ± 1.05	-52.94 ± 1.03	-62.87 ± 1.10
8783.4027	-62.37 ± 1.05	-63.85 ± 0.83	-61.09 ± 0.91	-57.79 ± 0.88	-67.10 ± 1.17
8794.2807	-57.88 ± 1.12	-58.95 ± 0.67	-55.81 ± 0.91	-54.58 ± 0.74	-55.20 ± 1.39
8794.3721	-62.64 ± 0.82	-56.06 ± 0.82	-52.92 ± 0.83	-54.25 ± 0.65	-54.95 ± 1.18
8800.4499	-51.56 ± 0.71	-49.19 ± 0.81	-48.68 ± 0.86	-52.65 ± 0.56	-52.14 ± 1.34
8802.3081	-54.58 ± 0.47	-53.36 ± 0.79	-55.49 ± 0.80	-54.26 ± 0.54	-56.03 ± 1.09
8808.2901	-50.97 ± 0.69	-52.85 ± 1.15	-50.52 ± 1.18	-51.35 ± 0.67	-52.83 ± 1.29
8808.4162	-51.08 ± 0.86	-53.20 ± 1.64	-50.25 ± 1.27	-52.60 ± 0.68	-46.18 ± 1.18
8819.4005	-57.48 ± 0.84	-63.89 ± 0.90	-58.23 ± 1.01	-61.44 ± 0.88	-62.84 ± 1.51
8819.5133	-57.54 ± 0.85	-64.26 ± 0.99	-60.80 ± 1.13	-62.34 ± 0.83	-63.26 ± 1.40
8820.3363	-56.47 ± 0.32	-59.48 ± 0.57	-55.27 ± 0.75	-58.45 ± 0.40	-55.14 ± 0.97
8822.2635	-61.48 ± 0.89	-64.45 ± 1.10	-62.46 ± 1.25	-62.28 ± 0.91	-68.54 ± 1.20
8827.2875	-60.76 ± 0.72	-63.95 ± 1.08	-64.31 ± 1.30	-62.47 ± 0.83	-65.57 ± 1.40
8847.2837	-48.17 ± 0.70	-51.55 ± 0.81	-46.30 ± 1.02	-51.08 ± 0.90	-53.53 ± 1.20
8848.2818	-64.35 ± 0.92	-63.35 ± 0.97	-61.65 ± 1.03	-65.60 ± 0.83	-67.35 ± 1.40
8865.2392	-58.35 ± 0.60	-57.28 ± 0.74	-58.07 ± 1.14	-61.00 ± 0.82	-52.51 ± 1.04
8867.2999	-56.75 ± 0.53	-59.00 ± 0.80	-57.92 ± 1.03	-58.47 ± 0.43	-57.10 ± 0.77
8885.2973	-58.89 ± 0.71	-61.67 ± 0.92	-60.04 ± 0.91	-60.59 ± 0.59	-63.72 ± 1.08
8886.2977	-52.92 ± 0.57	-51.03 ± 0.77	-49.42 ± 0.89	-53.77 ± 0.57	-50.14 ± 0.74

Table B2. H α Equivalent Widths. The HJD columns are HJD–2,450,000.

HJD	W_λ (Å)	HJD	W_λ (Å)	HJD	W_λ (Å)	HJD	W_λ (Å)	HJD	W_λ (Å)
7770.5334	1.22 ± 0.04	8009.4070	0.75 ± 0.12	8021.4226	1.94 ± 0.13	8042.3477	2.56 ± 0.14	8180.6390	0.41 ± 0.16
7777.6348	1.51 ± 0.16	8009.4350	1.00 ± 0.15	8021.4655	1.99 ± 0.14	8042.4189	2.64 ± 0.13	8181.2967	0.11 ± 0.09
7802.2705	2.66 ± 0.11	8009.4496	0.79 ± 0.17	8021.5084	2.11 ± 0.14	8043.3350	2.79 ± 0.12	8181.5151	-0.13 ± 0.11
7804.2711	2.82 ± 0.09	8009.4922	0.64 ± 0.14	8022.4587	2.05 ± 0.14	8044.2988	2.78 ± 0.12	8181.5399	-0.22 ± 0.13
7811.3601	2.81 ± 0.16	8009.5823	0.73 ± 0.08	8023.3396	2.19 ± 0.21	8044.3433	3.24 ± 0.12	8181.5640	-0.30 ± 0.10
7956.5319	2.94 ± 0.35	8010.0691	1.01 ± 0.30	8023.3975	2.44 ± 0.13	8044.3556	2.74 ± 0.14	8181.5879	-0.33 ± 0.12
7962.5612	3.14 ± 0.38	8010.1136	0.57 ± 0.24	8024.3935	2.04 ± 0.14	8044.3556	2.67 ± 0.14	8182.5423	-0.42 ± 0.14
7965.5511	3.24 ± 0.48	8010.1596	0.61 ± 0.25	8024.4651	2.07 ± 0.14	8044.3986	2.74 ± 0.15	8182.5653	-0.32 ± 0.14
7987.5452	1.35 ± 0.12	8010.2013	1.52 ± 0.23	8025.3454	2.26 ± 0.14	8044.3986	2.77 ± 0.15	8182.5869	-0.30 ± 0.13
7988.4413	1.23 ± 0.14	8010.2544	0.67 ± 0.23	8025.3745	2.55 ± 0.10	8045.2430	2.86 ± 0.12	8183.6155	-0.04 ± 0.08
7989.4361	1.02 ± 0.12	8010.2962	0.93 ± 0.31	8025.3880	2.11 ± 0.13	8045.3590	2.76 ± 0.14	8188.5727	-0.84 ± 0.12
7990.4747	0.91 ± 0.13	8010.3788	1.04 ± 0.12	8025.4309	2.06 ± 0.14	8045.5903	2.45 ± 0.10	8189.5427	-0.85 ± 0.17
7990.5549	0.91 ± 0.14	8011.3676	1.15 ± 0.14	8025.4739	2.01 ± 0.16	8046.3191	2.81 ± 0.14	8189.5649	-0.75 ± 0.17
7990.6008	0.90 ± 0.13	8011.4101	1.03 ± 0.12	8026.3308	2.34 ± 0.13	8046.3905	2.83 ± 0.14	8190.6213	-0.14 ± 0.14
7991.4147	0.63 ± 0.13	8011.4527	0.99 ± 0.13	8026.3733	2.16 ± 0.14	8047.4221	3.20 ± 0.13	8191.2859	-0.45 ± 0.16
7991.4571	0.81 ± 0.20	8011.4954	0.88 ± 0.12	8026.4012	2.42 ± 0.11	8049.0674	2.80 ± 0.29	8192.5247	-0.35 ± 0.11
7992.4143	0.54 ± 0.12	8012.3550	1.25 ± 0.11	8026.4026	2.26 ± 0.09	8049.4690	3.24 ± 0.12	8193.5283	-0.67 ± 0.08
7992.4566	0.41 ± 0.14	8012.3977	1.19 ± 0.12	8026.4160	2.16 ± 0.14	8050.0804	2.52 ± 0.23	8197.6118	0.34 ± 0.27
7992.4990	0.45 ± 0.15	8012.4403	1.15 ± 0.11	8029.6129	2.39 ± 0.08	8050.1716	2.95 ± 0.17	8198.3040	-0.22 ± 0.10
7992.5414	0.44 ± 0.15	8012.4830	1.08 ± 0.11	8030.4232	3.14 ± 0.14	8050.2637	2.66 ± 0.16	8199.3425	1.08 ± 0.15
7992.5840	0.48 ± 0.20	8013.3595	1.43 ± 0.14	8031.3385	2.58 ± 0.17	8050.3657	2.68 ± 0.16	8201.5293	0.49 ± 0.08
7992.6265	0.39 ± 0.17	8013.4023	1.28 ± 0.11	8032.3226	2.49 ± 0.13	8051.2719	3.07 ± 0.12	8208.5546	0.50 ± 0.14
7993.4328	0.68 ± 0.24	8014.1424	1.84 ± 0.26	8032.4242	2.97 ± 0.11	8051.3430	3.09 ± 0.12	8296.6079	3.38 ± 0.18
7994.4410	0.52 ± 0.13	8014.1842	1.20 ± 0.18	8033.3153	2.69 ± 0.13	8051.4002	3.16 ± 0.12	8297.6048	3.23 ± 0.18
7994.4835	0.26 ± 0.13	8015.3894	1.53 ± 0.12	8033.3578	2.73 ± 0.13	8051.4800	2.75 ± 0.19	8298.5980	3.45 ± 0.19
7994.5486	0.35 ± 0.14	8015.4320	1.45 ± 0.13	8033.3604	2.93 ± 0.11	8052.2411	3.01 ± 0.13	8300.5825	3.68 ± 0.18
7995.4308	0.26 ± 0.14	8015.4335	2.01 ± 0.10	8033.4005	2.52 ± 0.14	8052.3120	2.95 ± 0.15	8301.5940	3.57 ± 0.17
7995.4688	0.05 ± 0.14	8016.0403	1.50 ± 0.16	8035.3558	2.64 ± 0.13	8052.3692	2.91 ± 0.13	8303.5915	3.56 ± 0.16
7995.5660	0.11 ± 0.18	8016.0820	1.90 ± 0.14	8035.3985	2.59 ± 0.14	8053.3807	3.96 ± 0.12	8306.6001	3.45 ± 0.16
7997.4510	0.59 ± 0.24	8016.1238	1.33 ± 0.21	8035.4213	2.78 ± 0.11	8054.4068	3.20 ± 0.12	8308.5856	3.47 ± 0.13
7998.4580	0.80 ± 0.19	8016.1655	1.26 ± 0.16	8035.4416	2.61 ± 0.14	8054.4276	3.31 ± 0.14	8309.5830	3.52 ± 0.14
7998.4767	0.99 ± 0.25	8016.3622	1.95 ± 0.12	8036.2965	2.72 ± 0.14	8055.2738	3.18 ± 0.09	8310.5767	3.44 ± 0.16
7998.7549	0.43 ± 0.29	8016.4588	1.46 ± 0.13	8036.3393	2.70 ± 0.14	8055.3599	4.03 ± 0.11	8311.5814	3.20 ± 0.16
7999.4398	0.65 ± 0.18	8016.5013	1.44 ± 0.13	8036.3518	3.01 ± 0.10	8056.3719	3.54 ± 0.08	8312.5751	3.46 ± 0.13
7999.4594	0.46 ± 0.13	8017.0372	2.14 ± 0.30	8036.3827	2.53 ± 0.14	8057.4159	2.37 ± 0.18	8313.5683	3.78 ± 0.15
8000.1570	0.35 ± 0.25	8017.0789	2.00 ± 0.33	8036.4258	2.54 ± 0.14	8058.2510	3.13 ± 0.10	8314.5782	3.59 ± 0.12
8000.1987	0.07 ± 0.25	8017.1207	1.79 ± 0.33	8036.4688	2.45 ± 0.16	8058.3437	3.38 ± 0.13	8315.5591	3.34 ± 0.13
8000.2411	0.05 ± 0.26	8017.2360	1.62 ± 0.21	8037.2970	2.68 ± 0.14	8058.4695	3.55 ± 0.15	8316.5960	3.45 ± 0.13
8000.4166	0.25 ± 0.22	8017.2777	1.71 ± 0.25	8037.3066	2.84 ± 0.09	8059.3636	3.45 ± 0.11	8317.5663	3.69 ± 0.13
8001.4153	0.94 ± 0.13	8017.3816	2.14 ± 0.14	8037.3255	2.72 ± 0.15	8059.4184	3.54 ± 0.16	8319.5842	3.65 ± 0.13
8001.4203	0.36 ± 0.16	8017.4092	1.62 ± 0.14	8037.3684	2.47 ± 0.15	8065.1310	3.04 ± 0.19	8321.5871	3.53 ± 0.16
8001.4630	0.17 ± 0.21	8017.4124	1.70 ± 0.12	8037.4113	2.39 ± 0.16	8065.1310	3.32 ± 0.18	8323.5701	3.50 ± 0.12
8001.5059	-0.02 ± 0.22	8017.4516	1.42 ± 0.14	8037.4543	2.45 ± 0.16	8065.4242	3.99 ± 0.15	8324.5287	3.34 ± 0.24
8002.3950	0.31 ± 0.12	8018.3424	1.54 ± 0.08	8038.3054	2.70 ± 0.14	8067.3819	3.54 ± 0.11	8324.6068	3.55 ± 0.15
8003.0934	0.52 ± 0.30	8018.4112	1.84 ± 0.28	8038.3484	2.60 ± 0.15	8071.3348	3.30 ± 0.14	8325.5835	3.53 ± 0.16
8003.1351	0.65 ± 0.26	8018.4862	1.64 ± 0.14	8038.3913	2.66 ± 0.14	8074.3123	3.38 ± 0.14	8328.5539	3.36 ± 0.32
8003.1768	0.69 ± 0.28	8018.4862	1.69 ± 0.15	8038.4343	2.55 ± 0.14	8074.3517	3.39 ± 0.13	8329.5320	3.27 ± 0.17
8003.2186	0.47 ± 0.28	8019.0403	1.87 ± 0.31	8038.4528	2.84 ± 0.19	8074.4039	3.38 ± 0.12	8331.5225	3.52 ± 0.19
8004.4058	1.23 ± 0.13	8019.0820	2.19 ± 0.27	8039.2924	2.90 ± 0.14	8077.2347	3.46 ± 0.12	8332.5685	3.42 ± 0.17
8004.4185	0.44 ± 0.13	8019.1238	1.91 ± 0.26	8039.3352	2.83 ± 0.14	8085.3270	3.36 ± 0.13	8333.5573	3.42 ± 0.17
8005.4141	0.83 ± 0.16	8019.1655	1.86 ± 0.23	8039.3782	2.82 ± 0.14	8090.0433	2.73 ± 0.34	8334.5957	3.56 ± 0.18
8006.5533	0.31 ± 0.11	8019.2443	1.88 ± 0.26	8039.4211	2.70 ± 0.14	8094.2220	3.50 ± 0.12	8335.5596	3.42 ± 0.17
8006.5762	0.42 ± 0.10	8019.2860	1.87 ± 0.24	8039.4641	2.85 ± 0.17	8104.5126	3.53 ± 0.26	8337.4220	2.96 ± 0.16
8007.0402	0.35 ± 0.21	8019.3278	1.67 ± 0.24	8040.3018	2.72 ± 0.16	8106.4177	3.19 ± 0.22	8337.5458	3.05 ± 0.18
8007.1411	0.62 ± 0.38	8019.3480	1.94 ± 0.14	8040.3305	2.67 ± 0.12	8134.5832	3.15 ± 0.07	8339.5539	3.02 ± 0.16
8007.3813	0.23 ± 0.11	8019.3906	1.84 ± 0.14	8040.3424	2.56 ± 0.12	8143.2471	3.49 ± 0.09	8341.5381	2.69 ± 0.23
8007.5085	0.21 ± 0.13	8019.4335	1.70 ± 0.14	8040.3446	2.65 ± 0.17	8175.5618	0.51 ± 0.06	8345.5266	2.32 ± 0.15
8008.0459	0.47 ± 0.32	8019.4764	1.72 ± 0.16	8040.3876	2.65 ± 0.14	8176.5078	0.19 ± 0.07	8346.4356	0.94 ± 0.10
8008.0917	-0.33 ± 0.33	8019.5190	1.70 ± 0.16	8040.4296	2.99 ± 0.12	8176.5764	0.37 ± 0.07	8346.4918	2.14 ± 0.19
8008.1374	0.68 ± 0.36	8020.3865	1.96 ± 0.14	8040.4306	2.62 ± 0.14	8180.2561	0.14 ± 0.08	8346.5031	2.42 ± 0.15
8008.4270	0.73 ± 0.10	8020.4292	1.81 ± 0.14	8041.3689	3.05 ± 0.31	8180.2874	-0.41 ± 0.08	8346.5752	2.27 ± 0.15
8008.5496	0.63 ± 0.11	8020.4721	1.64 ± 0.28	8041.4267	2.65 ± 0.15	8180.5154	-0.36 ± 0.14	8346.6401	2.23 ± 0.22
8009.4014	0.51 ± 0.09	8021.3369	2.08 ± 0.13	8041.4549	3.02 ± 0.13	8180.5386	-0.17 ± 0.11	8347.4435	0.85 ± 0.13
8009.4014	0.61 ± 0.09	8021.3797	2.07 ± 0.14	8042.2766	2.53 ± 0.14	8180.5607	0.24 ± 0.07	8347.4832	1.08 ± 0.15

Table B2 – continued H α Equivalent Widths. The HJD columns are HJD–2,450,000.

HJD	W_λ (Å)	HJD	W_λ (Å)	HJD	W_λ (Å)	HJD	W_λ (Å)	HJD	W_λ (Å)
8347.5657	0.87 ± 0.16	8385.5020	2.54 ± 0.11	8441.4463	0.24 ± 0.13	8720.4803	3.61 ± 0.14	8812.8332	0.84 ± 0.09
8348.4560	1.16 ± 0.15	8386.4720	2.43 ± 0.09	8441.4473	0.68 ± 0.10	8721.5096	3.68 ± 0.14	8816.2459	1.62 ± 0.08
8349.3928	2.39 ± 0.33	8387.3004	1.64 ± 0.11	8443.4107	0.71 ± 0.07	8721.6073	3.91 ± 0.23	8818.3911	1.63 ± 0.10
8349.4227	1.75 ± 0.12	8387.3740	1.37 ± 0.14	8444.3055	0.95 ± 0.09	8722.3977	4.41 ± 0.13	8818.6059	1.16 ± 0.11
8349.5208	1.11 ± 0.10	8387.4332	2.24 ± 0.09	8449.7260	1.13 ± 0.10	8722.5356	3.76 ± 0.19	8819.4005	1.80 ± 0.09
8349.5560	3.07 ± 0.24	8387.4548	2.42 ± 0.11	8451.3159	1.03 ± 0.19	8725.4398	3.53 ± 0.14	8819.5133	1.51 ± 0.09
8349.5637	1.99 ± 0.23	8388.3864	1.71 ± 0.08	8453.3599	1.19 ± 0.09	8725.4894	3.95 ± 0.16	8819.6248	1.22 ± 0.08
8350.4430	0.80 ± 0.14	8388.4121	2.47 ± 0.07	8454.2752	1.28 ± 0.22	8726.4255	3.76 ± 0.27	8820.3047	2.63 ± 0.13
8350.4797	1.81 ± 0.24	8389.4065	2.54 ± 0.12	8457.3021	1.64 ± 0.16	8726.4970	3.70 ± 0.18	8820.3363	1.85 ± 0.09
8350.4903	0.47 ± 0.11	8389.4521	2.34 ± 0.18	8460.4178	1.68 ± 0.10	8726.7754	3.57 ± 0.15	8821.3717	0.73 ± 0.09
8350.5061	0.67 ± 0.12	8390.4486	2.50 ± 0.18	8463.4456	1.76 ± 0.12	8764.4331	1.75 ± 0.18	8822.2635	1.91 ± 0.11
8350.5475	1.61 ± 0.16	8391.4717	2.05 ± 0.08	8470.2521	2.04 ± 0.11	8766.3172	1.75 ± 0.09	8822.3857	0.87 ± 0.08
8350.5689	0.79 ± 0.13	8392.3825	1.87 ± 0.11	8478.3307	1.41 ± 0.12	8766.3652	1.63 ± 0.12	8825.3976	2.92 ± 0.30
8351.4384	0.47 ± 0.10	8393.4286	2.84 ± 0.09	8479.2329	2.60 ± 0.15	8766.4357	1.43 ± 0.13	8826.7112	2.48 ± 0.10
8351.5391	1.58 ± 0.12	8394.3794	2.35 ± 0.28	8480.2246	2.41 ± 0.21	8767.3710	1.16 ± 0.15	8827.2875	2.00 ± 0.12
8351.5541	1.60 ± 0.16	8395.4098	2.63 ± 0.11	8480.2827	2.69 ± 0.15	8767.3740	1.06 ± 0.19	8828.2416	2.65 ± 0.13
8352.4009	1.80 ± 0.28	8395.4192	2.83 ± 0.15	8483.2416	2.75 ± 0.16	8767.4553	1.23 ± 0.16	8831.8150	1.86 ± 0.11
8352.4389	0.77 ± 0.11	8396.4035	3.03 ± 0.11	8486.7017	2.71 ± 0.10	8768.3466	1.33 ± 0.14	8832.6416	2.41 ± 0.07
8352.4421	1.27 ± 0.14	8396.4498	3.09 ± 0.16	8487.3411	2.73 ± 0.12	8768.4380	1.29 ± 0.12	8832.7319	2.67 ± 0.09
8352.5396	1.49 ± 0.29	8397.3892	1.95 ± 0.10	8492.4135	2.71 ± 0.11	8769.3668	1.09 ± 0.10	8833.7596	1.92 ± 0.09
8353.4969	1.15 ± 0.14	8397.4057	2.91 ± 0.14	8494.6523	2.53 ± 0.08	8769.3878	1.09 ± 0.17	8834.6751	2.39 ± 0.07
8354.2001	1.08 ± 0.27	8397.4305	3.14 ± 0.22	8499.2476	3.15 ± 0.12	8769.3947	1.21 ± 0.13	8834.7817	1.89 ± 0.09
8355.1780	0.71 ± 0.29	8398.3767	3.11 ± 0.39	8501.6196	3.30 ± 0.08	8769.6369	1.22 ± 0.23	8837.7508	2.22 ± 0.06
8356.4734	-0.06 ± 0.09	8399.6737	2.72 ± 0.13	8503.5913	3.23 ± 0.08	8770.3383	1.30 ± 0.14	8838.7555	1.86 ± 0.10
8357.4494	-0.20 ± 0.14	8400.3271	1.95 ± 0.11	8505.2566	2.39 ± 0.09	8770.4203	0.80 ± 0.06	8840.6453	2.51 ± 0.09
8357.5413	0.64 ± 0.22	8400.3886	2.73 ± 0.16	8505.3366	3.15 ± 0.13	8770.4298	1.19 ± 0.11	8843.3750	1.89 ± 0.10
8357.5837	0.63 ± 0.24	8400.4207	2.90 ± 0.13	8509.2493	3.51 ± 0.16	8770.7000	1.00 ± 0.08	8843.6294	2.46 ± 0.08
8358.4326	-0.80 ± 0.18	8400.4563	2.98 ± 0.11	8520.2811	2.74 ± 0.16	8771.0380	0.79 ± 0.39	8846.7118	1.77 ± 0.11
8358.4607	0.66 ± 0.16	8401.4106	2.03 ± 0.08	8521.2674	2.90 ± 0.13	8771.3032	0.78 ± 0.25	8847.2837	1.92 ± 0.13
8358.5246	0.39 ± 0.16	8401.4382	2.99 ± 0.19	8521.3599	3.29 ± 0.26	8771.6480	0.98 ± 0.09	8847.3196	1.18 ± 0.10
8359.4581	0.96 ± 0.23	8401.4578	2.96 ± 0.09	8523.3681	3.68 ± 0.12	8772.8639	0.03 ± 0.07	8847.5933	2.15 ± 0.09
8359.4907	-0.54 ± 0.16	8402.3614	2.04 ± 0.11	8526.3670	3.14 ± 0.34	8772.9158	0.10 ± 0.07	8848.2818	1.86 ± 0.11
8360.1777	0.95 ± 0.20	8402.4273	2.79 ± 0.10	8528.2736	3.01 ± 0.13	8773.6991	0.66 ± 0.09	8848.3080	3.65 ± 0.34
8362.4822	0.55 ± 0.11	8404.4002	2.71 ± 0.22	8533.2702	3.78 ± 0.13	8774.6085	0.48 ± 0.27	8848.3183	2.01 ± 0.17
8363.4630	-0.42 ± 0.11	8405.3428	2.58 ± 0.18	8539.3181	3.86 ± 0.11	8774.6842	0.54 ± 0.07	8849.2524	1.97 ± 0.18
8363.4887	0.17 ± 0.20	8407.4325	1.03 ± 0.10	8540.3253	3.74 ± 0.09	8775.6183	0.11 ± 0.17	8849.3407	2.11 ± 0.11
8363.5459	0.40 ± 0.22	8407.5264	1.93 ± 0.13	8541.3233	3.60 ± 0.11	8777.6303	-0.55 ± 0.07	8849.6030	2.08 ± 0.08
8364.4272	0.09 ± 0.19	8408.3608	0.66 ± 0.16	8542.3143	3.79 ± 0.12	8778.6482	-0.61 ± 0.07	8852.6931	1.16 ± 0.08
8364.5478	0.79 ± 0.11	8408.4154	0.60 ± 0.09	8553.3259	3.64 ± 0.12	8778.6800	-0.02 ± 0.07	8855.3400	2.15 ± 0.23
8365.4541	0.64 ± 0.17	8409.1540	1.66 ± 0.16	8676.5924	3.63 ± 0.22	8779.6359	-0.60 ± 0.08	8855.6228	1.26 ± 0.08
8366.4522	0.76 ± 0.14	8409.3058	1.75 ± 0.24	8677.5842	3.71 ± 0.17	8782.3610	-0.35 ± 0.15	8855.7246	0.72 ± 0.08
8368.4562	1.06 ± 0.11	8409.5829	1.86 ± 0.12	8680.6004	3.55 ± 0.18	8782.4243	-0.39 ± 0.14	8857.3505	2.24 ± 0.36
8369.1768	1.11 ± 0.17	8410.3355	0.60 ± 0.13	8684.4613	4.30 ± 0.16	8783.3183	-0.28 ± 0.15	8857.6647	0.29 ± 0.37
8369.4500	1.23 ± 0.11	8410.4964	1.43 ± 0.11	8687.5859	3.76 ± 0.16	8783.4027	-0.39 ± 0.14	8860.3785	0.91 ± 0.10
8370.1537	1.16 ± 0.12	8411.3265	0.46 ± 0.09	8690.6078	4.03 ± 0.20	8784.4023	-0.83 ± 0.06	8860.6762	1.20 ± 0.09
8370.4057	-0.02 ± 0.13	8411.3838	1.09 ± 0.22	8693.5849	3.86 ± 0.16	8786.5178	-0.68 ± 0.13	8860.7032	0.08 ± 0.10
8370.4549	1.15 ± 0.16	8411.4720	1.30 ± 0.09	8696.6177	3.41 ± 0.25	8789.8308	-0.96 ± 0.09	8861.6973	-0.08 ± 0.09
8371.4276	1.31 ± 0.17	8412.3715	0.20 ± 0.08	8698.5910	3.51 ± 0.17	8792.6222	-0.84 ± 0.08	8862.3654	0.41 ± 0.09
8372.4785	1.20 ± 0.15	8412.4934	1.30 ± 0.08	8699.5915	3.32 ± 0.19	8792.8348	-0.69 ± 0.09	8863.4157	0.14 ± 0.15
8372.4872	1.28 ± 0.19	8413.4110	0.60 ± 0.21	8700.5591	3.70 ± 0.15	8793.4263	-0.37 ± 0.09	8864.3923	-0.16 ± 0.09
8373.4747	1.11 ± 0.16	8415.2834	-0.05 ± 0.12	8701.5719	3.45 ± 0.25	8794.2807	-0.14 ± 0.22	8865.2392	-0.14 ± 0.13
8373.4764	1.16 ± 0.09	8416.4004	0.40 ± 0.20	8703.4454	3.51 ± 0.09	8794.3721	-0.17 ± 0.18	8865.6929	-0.26 ± 0.08
8373.4894	1.89 ± 0.31	8417.3037	0.34 ± 0.19	8703.5938	3.45 ± 0.28	8795.3236	-0.40 ± 0.15	8866.6311	-0.44 ± 0.08
8373.5119	1.32 ± 0.10	8426.3364	-0.51 ± 0.11	8704.5909	3.65 ± 0.17	8799.6288	-0.10 ± 0.15	8867.2999	0.07 ± 0.11
8374.3180	0.89 ± 0.12	8428.3085	-0.79 ± 0.10	8705.5038	3.49 ± 0.21	8799.8145	0.08 ± 0.09	8867.6440	-0.42 ± 0.08
8376.4731	1.61 ± 0.11	8429.3295	-0.07 ± 0.19	8706.5683	3.88 ± 0.18	8800.4499	0.56 ± 0.10	8868.2618	-0.31 ± 0.11
8377.4148	1.46 ± 0.19	8432.2991	0.25 ± 0.19	8710.5353	3.60 ± 0.23	8800.6136	0.38 ± 0.13	8868.3617	-0.55 ± 0.08
8377.4630	0.64 ± 0.10	8434.2726	0.51 ± 0.15	8711.5316	3.62 ± 0.14	8801.6310	0.10 ± 0.12	8871.6549	-0.20 ± 0.08
8377.4921	1.69 ± 0.09	8436.3603	0.11 ± 0.17	8712.5425	3.86 ± 0.14	8802.3081	0.71 ± 0.09	8872.2378	-0.39 ± 0.11
8378.3923	0.69 ± 0.10	8436.7523	0.56 ± 0.09	8713.5377	3.73 ± 0.13	8805.3849	0.78 ± 0.06	8872.6572	-0.35 ± 0.07
8378.5057	1.64 ± 0.10	8437.3468	0.29 ± 0.18	8713.6439	4.47 ± 0.20	8805.6111	0.43 ± 0.09	8877.6509	0.16 ± 0.09
8379.3695	1.18 ± 0.11	8438.3249	0.25 ± 0.17	8716.6439	3.71 ± 0.14	8806.4968	0.49 ± 0.21	8878.6466	0.44 ± 0.10
8379.5082	1.90 ± 0.16	8438.4520	0.70 ± 0.28	8717.6205	3.52 ± 0.14	8810.2402	2.09 ± 0.14	8880.3072	1.76 ± 0.23
8381.3982	1.73 ± 0.19	8441.2923	0.66 ± 0.25	8718.4373	3.77 ± 0.34	8810.6246	0.75 ± 0.11	8880.6416	0.57 ± 0.08
8381.4493	2.24 ± 0.14	8441.2979	0.28 ± 0.20	8719.5512	3.63 ± 0.16	8811.6303	0.82 ± 0.09	8881.3059	0.69 ± 0.11

Table B2 – *continued* H α Equivalent Widths. The HJD columns are HJD–2,450,000.

HJD	W_λ (Å)	HJD	W_λ (Å)	HJD	W_λ (Å)	HJD	W_λ (Å)	HJD	W_λ (Å)
8881.6346	0.87 ± 0.08	8885.6416	0.97 ± 0.11	8887.6513	1.52 ± 0.09	8895.6481	1.93 ± 0.09	8904.6433	2.26 ± 0.11
8884.2778	0.62 ± 0.09	8886.2977	1.66 ± 0.08	8888.6345	1.43 ± 0.08	8897.6450	2.01 ± 0.12	8906.6573	2.28 ± 0.10
8885.2973	1.49 ± 0.08	8887.3368	1.89 ± 0.08	8893.6390	1.73 ± 0.08	8899.6473	2.15 ± 0.16		

Table B3. $H\beta$ Equivalent Widths. The HJD column is HJD - 2,450,000.

HJD	W_λ (Å)	HJD	W_λ (Å)	HJD	W_λ (Å)	HJD	W_λ (Å)	HJD	W_λ (Å)
7987.5452	2.63 ± 0.08	8025.3454	3.61 ± 0.09	8052.2411	3.72 ± 0.08	8362.4822	2.86 ± 0.09	8454.2752	3.28 ± 0.11
7988.4413	2.80 ± 0.08	8025.3880	3.58 ± 0.10	8052.3120	3.80 ± 0.08	8363.4887	2.92 ± 0.10	8457.3021	3.34 ± 0.10
7989.4361	2.75 ± 0.07	8025.4309	3.55 ± 0.09	8052.3692	3.78 ± 0.07	8363.5459	2.98 ± 0.13	8463.4456	3.09 ± 0.06
7990.4747	2.85 ± 0.08	8025.4739	3.60 ± 0.11	8054.4068	3.73 ± 0.08	8364.5478	2.99 ± 0.06	8479.2329	3.45 ± 0.09
7990.5549	2.97 ± 0.09	8026.3308	3.53 ± 0.07	8058.2510	3.81 ± 0.06	8365.4541	3.03 ± 0.08	8480.2246	3.58 ± 0.12
7990.6008	2.84 ± 0.08	8026.3733	3.53 ± 0.09	8058.3437	3.69 ± 0.08	8366.4522	2.94 ± 0.08	8480.2827	3.52 ± 0.09
7991.4147	2.86 ± 0.08	8026.4026	3.57 ± 0.06	8059.3636	3.81 ± 0.07	8368.4562	3.10 ± 0.06	8483.2416	3.58 ± 0.10
7991.4571	2.74 ± 0.12	8026.4160	3.56 ± 0.09	8071.3348	3.78 ± 0.07	8369.4500	2.97 ± 0.07	8487.3411	3.52 ± 0.09
7992.4143	2.70 ± 0.08	8030.2831	3.65 ± 0.05	8074.3123	3.75 ± 0.06	8370.4549	3.23 ± 0.09	8492.4135	3.57 ± 0.06
7992.4566	2.71 ± 0.08	8031.3385	3.60 ± 0.12	8074.3517	3.69 ± 0.08	8371.4276	3.17 ± 0.11	8499.2476	3.47 ± 0.08
7992.4990	2.52 ± 0.10	8032.3226	3.59 ± 0.08	8074.4039	3.78 ± 0.07	8372.4872	3.33 ± 0.10	8509.2493	3.63 ± 0.08
7992.5414	2.49 ± 0.10	8032.4526	3.63 ± 0.06	8077.2347	3.73 ± 0.07	8372.4785	3.28 ± 0.09	8520.2811	3.63 ± 0.11
7992.5840	2.58 ± 0.12	8033.3153	3.57 ± 0.10	8085.3270	3.75 ± 0.10	8373.4747	3.28 ± 0.09	8521.2674	3.59 ± 0.09
7992.6265	2.48 ± 0.10	8033.3578	3.62 ± 0.08	8094.2220	3.70 ± 0.06	8373.5119	3.20 ± 0.08	8528.2736	3.57 ± 0.10
7994.4410	2.84 ± 0.08	8033.4005	3.62 ± 0.09	8143.2471	3.74 ± 0.07	8376.4731	3.28 ± 0.06	8529.2945	3.53 ± 0.09
7994.4835	2.44 ± 0.09	8035.3558	3.61 ± 0.08	8180.2874	2.66 ± 0.09	8377.4148	3.38 ± 0.10	8530.2771	3.61 ± 0.09
7994.5486	2.62 ± 0.08	8035.3985	3.61 ± 0.09	8181.2967	2.71 ± 0.13	8377.4921	3.34 ± 0.08	8531.2738	3.54 ± 0.12
7995.4308	2.71 ± 0.07	8035.4401	3.71 ± 0.09	8183.3031	10.60 ± 0.77	8378.5057	3.37 ± 0.07	8532.2693	3.65 ± 0.08
7995.5660	2.57 ± 0.10	8035.4416	3.66 ± 0.09	8186.3662	7.01 ± 0.45	8379.5082	3.48 ± 0.11	8533.2702	3.72 ± 0.09
8000.4166	2.86 ± 0.11	8036.2965	3.60 ± 0.09	8191.2859	2.78 ± 0.10	8385.5020	3.66 ± 0.06	8539.3181	3.68 ± 0.06
8001.4203	2.91 ± 0.08	8036.3393	3.67 ± 0.10	8198.3040	2.86 ± 0.13	8386.4720	3.58 ± 0.06	8540.3253	3.35 ± 0.07
8001.4630	2.80 ± 0.10	8036.3827	3.62 ± 0.08	8296.6079	3.81 ± 0.10	8387.4332	3.59 ± 0.05	8541.3233	3.79 ± 0.06
8001.5059	2.95 ± 0.13	8036.4258	3.63 ± 0.10	8297.6048	3.83 ± 0.10	8387.4548	3.52 ± 0.07	8542.3143	3.67 ± 0.07
8004.4185	2.78 ± 0.09	8036.4297	3.66 ± 0.06	8298.5980	3.82 ± 0.10	8388.4121	3.57 ± 0.06	8553.3259	3.63 ± 0.07
8009.4014	2.96 ± 0.07	8036.4688	3.65 ± 0.10	8300.5825	3.78 ± 0.11	8389.4065	3.68 ± 0.09	8676.5924	3.91 ± 0.11
8009.4070	2.93 ± 0.07	8037.2970	3.56 ± 0.10	8301.5940	3.71 ± 0.10	8389.4521	3.73 ± 0.11	8677.5842	3.84 ± 0.09
8009.4496	2.91 ± 0.09	8037.3214	3.65 ± 0.06	8303.5915	3.77 ± 0.10	8390.4486	3.74 ± 0.11	8680.6004	3.83 ± 0.09
8009.4922	2.97 ± 0.08	8037.3255	3.64 ± 0.09	8306.6001	3.81 ± 0.09	8393.4286	3.61 ± 0.06	8686.5961	3.88 ± 0.09
8011.3676	3.16 ± 0.09	8037.3684	3.64 ± 0.10	8308.5856	3.80 ± 0.10	8394.3794	3.72 ± 0.14	8687.5859	3.86 ± 0.08
8011.4101	3.23 ± 0.09	8037.4113	3.65 ± 0.10	8309.5830	3.81 ± 0.08	8395.4098	3.68 ± 0.07	8690.6078	3.85 ± 0.10
8011.4527	3.20 ± 0.08	8037.4543	3.61 ± 0.09	8310.5767	3.91 ± 0.09	8395.4192	3.74 ± 0.09	8693.5849	3.75 ± 0.07
8011.4954	3.22 ± 0.08	8038.3054	3.64 ± 0.09	8311.5814	3.81 ± 0.08	8396.4035	3.76 ± 0.07	8696.6177	3.97 ± 0.16
8012.3550	3.17 ± 0.07	8038.3484	3.65 ± 0.08	8312.5751	3.85 ± 0.08	8396.4498	3.71 ± 0.09	8698.5910	3.83 ± 0.09
8012.3977	2.80 ± 0.07	8038.3913	3.72 ± 0.09	8313.5683	3.81 ± 0.10	8397.4057	3.65 ± 0.07	8699.5915	3.91 ± 0.11
8012.4403	3.09 ± 0.07	8038.4343	3.69 ± 0.09	8314.5782	3.78 ± 0.09	8397.4305	3.82 ± 0.17	8700.5591	3.89 ± 0.08
8012.4830	3.03 ± 0.07	8039.2924	3.61 ± 0.09	8315.5591	3.72 ± 0.09	8398.3767	3.74 ± 0.18	8701.5719	4.11 ± 0.13
8013.3595	3.15 ± 0.07	8039.3352	3.61 ± 0.08	8316.5960	3.77 ± 0.08	8400.3886	3.69 ± 0.11	8703.5938	3.82 ± 0.16
8013.4023	3.21 ± 0.06	8039.3782	3.64 ± 0.09	8317.5663	3.85 ± 0.08	8400.4563	3.58 ± 0.07	8704.5909	3.91 ± 0.09
8015.3894	3.38 ± 0.07	8039.4211	3.63 ± 0.09	8319.5842	3.82 ± 0.09	8401.4382	3.74 ± 0.12	8706.5683	3.99 ± 0.09
8015.4320	3.36 ± 0.08	8039.4641	3.69 ± 0.11	8321.5871	3.72 ± 0.13	8401.4578	3.58 ± 0.07	8710.5353	4.02 ± 0.13
8016.4588	3.43 ± 0.08	8040.3018	3.57 ± 0.10	8323.5701	3.83 ± 0.08	8404.4002	3.51 ± 0.11	8711.5316	3.95 ± 0.08
8016.5013	3.40 ± 0.09	8040.3305	3.59 ± 0.10	8324.5287	3.85 ± 0.14	8405.3428	3.51 ± 0.12	8712.5425	3.94 ± 0.08
8017.4092	3.47 ± 0.08	8040.3446	3.63 ± 0.11	8324.6068	3.81 ± 0.10	8407.5264	3.25 ± 0.08	8713.5377	3.90 ± 0.07
8017.4516	3.47 ± 0.08	8040.3612	3.59 ± 0.11	8325.5835	3.82 ± 0.11	8409.3058	3.18 ± 0.13	8716.6439	3.47 ± 0.07
8018.4862	3.43 ± 0.09	8040.3876	3.63 ± 0.09	8328.5539	3.81 ± 0.19	8409.5829	3.26 ± 0.06	8717.6205	3.46 ± 0.07
8019.3480	3.48 ± 0.07	8040.4306	3.64 ± 0.08	8329.5320	3.79 ± 0.10	8410.4964	3.08 ± 0.07	8719.5512	3.94 ± 0.09
8019.3906	3.46 ± 0.08	8041.4267	3.70 ± 0.08	8331.5225	3.66 ± 0.11	8411.3838	3.11 ± 0.11	8720.4803	3.89 ± 0.08
8019.4335	3.47 ± 0.10	8042.2766	3.62 ± 0.09	8332.5685	3.87 ± 0.11	8411.4720	3.06 ± 0.06	8721.5096	3.97 ± 0.08
8019.4764	3.51 ± 0.09	8042.3477	3.65 ± 0.08	8333.5573	3.84 ± 0.10	8412.4934	2.77 ± 0.06	8721.6073	3.61 ± 0.12
8019.5190	3.48 ± 0.11	8042.4189	3.68 ± 0.09	8334.5957	3.77 ± 0.12	8413.4110	3.02 ± 0.12	8722.5356	3.87 ± 0.10
8020.3865	3.58 ± 0.08	8042.4236	3.64 ± 0.06	8335.5596	3.74 ± 0.10	8416.4004	2.91 ± 0.12	8725.4894	3.95 ± 0.08
8020.4292	3.57 ± 0.10	8043.3350	3.63 ± 0.07	8337.5458	3.62 ± 0.11	8417.3037	2.98 ± 0.12	8726.4970	3.87 ± 0.08
8020.4721	3.54 ± 0.17	8043.4325	3.53 ± 0.04	8339.5539	3.64 ± 0.10	8429.3295	2.71 ± 0.10	8729.4954	3.85 ± 0.10
8021.3369	3.56 ± 0.08	8044.2988	3.67 ± 0.09	8341.5381	3.52 ± 0.12	8432.2991	2.85 ± 0.12	8730.5079	3.94 ± 0.11
8021.3797	3.57 ± 0.08	8044.3556	3.66 ± 0.09	8345.5266	3.36 ± 0.09	8434.2726	2.83 ± 0.09	8731.4839	3.92 ± 0.10
8021.4226	3.55 ± 0.08	8044.3986	3.60 ± 0.08	8346.5752	3.38 ± 0.09	8436.3603	2.86 ± 0.10	8732.5264	3.81 ± 0.11
8021.4519	3.47 ± 0.06	8045.3590	3.65 ± 0.09	8346.6401	3.37 ± 0.11	8437.3468	2.93 ± 0.09	8738.4556	3.91 ± 0.08
8021.4655	3.55 ± 0.08	8046.3191	3.65 ± 0.08	8349.4227	3.25 ± 0.08	8438.3249	2.89 ± 0.08	8739.4935	3.95 ± 0.08
8021.5084	3.58 ± 0.09	8046.3905	3.70 ± 0.08	8350.4430	3.08 ± 0.08	8438.4520	2.70 ± 0.25	8740.4619	3.90 ± 0.07
8022.4587	3.52 ± 0.09	8050.2637	3.69 ± 0.09	8352.5396	3.21 ± 0.18	8441.2979	2.94 ± 0.10	8742.4559	3.90 ± 0.08
8023.3396	3.54 ± 0.14	8050.3657	3.68 ± 0.08	8357.4494	2.86 ± 0.07	8441.4473	2.68 ± 0.06	8743.4694	3.95 ± 0.08
8023.4082	3.56 ± 0.07	8051.2719	3.75 ± 0.07	8357.5413	3.05 ± 0.12	8443.4107	2.63 ± 0.06	8744.4488	3.92 ± 0.08
8024.3935	3.51 ± 0.11	8051.3430	3.74 ± 0.07	8357.5837	2.98 ± 0.13	8444.3055	2.75 ± 0.05	8746.4304	4.00 ± 0.12
8024.4651	3.57 ± 0.09	8051.4002	3.76 ± 0.08	8359.4581	2.89 ± 0.15	8451.3159	3.21 ± 0.10	8755.4179	3.97 ± 0.09

Table B3 – *continued* H β Equivalent Widths. The HJD column is HJD - 2,450,000.

HJD	W_{λ} (Å)	HJD	W_{λ} (Å)	HJD	W_{λ} (Å)	HJD	W_{λ} (Å)	HJD	W_{λ} (Å)
8762.4578	3.42 ± 0.09	8768.3466	3.13 ± 0.08	8778.5186	2.41 ± 0.07	8794.3721	2.87 ± 0.11	8827.2875	3.08 ± 0.07
8763.4293	3.10 ± 0.10	8768.3660	2.96 ± 0.08	8778.6023	2.57 ± 0.09	8800.4499	2.58 ± 0.07	8847.2837	3.22 ± 0.09
8764.4331	3.28 ± 0.10	8768.4380	3.13 ± 0.08	8778.6642	2.49 ± 0.13	8802.3081	2.77 ± 0.08	8848.2818	3.34 ± 0.09
8766.3172	3.07 ± 0.07	8769.3947	3.07 ± 0.07	8782.3610	2.74 ± 0.08	8808.2901	2.95 ± 0.08	8865.2392	2.88 ± 0.09
8766.3652	3.11 ± 0.08	8769.3668	2.87 ± 0.06	8782.4243	2.73 ± 0.09	8808.4162	2.97 ± 0.10	8867.2999	2.46 ± 0.07
8766.4357	3.20 ± 0.09	8770.3383	3.11 ± 0.08	8783.3183	2.81 ± 0.09	8819.4005	2.98 ± 0.07	8885.2973	3.20 ± 0.05
8767.3710	3.07 ± 0.08	8770.4298	3.10 ± 0.07	8783.3724	2.69 ± 0.07	8819.5133	3.19 ± 0.06	8886.2977	3.21 ± 0.05
8767.3740	3.06 ± 0.11	8776.3572	2.78 ± 0.11	8783.4027	2.81 ± 0.09	8820.3363	2.90 ± 0.07		
8767.4553	3.11 ± 0.09	8778.3498	2.61 ± 0.07	8794.2807	2.82 ± 0.13	8822.2635	3.10 ± 0.08		

Table B4. H α Gaussian Parameters for Excess Emission. The HJD column is HJD - 2,450,000.

HJD	FWHM (km s ⁻¹)	Center (km s ⁻¹)	Height (Norm. Flux)	HJD	FWHM (km s ⁻¹)	Center (km s ⁻¹)	Height (Norm. Flux)
7770.5334	90.79 ± 0.96	-51.61 ± 0.96	0.4294 ± 0.0040	8010.0691	87.70 ± 1.35	-58.03 ± 1.35	0.5309 ± 0.0071
7777.6348	88.78 ± 1.22	-58.97 ± 1.22	0.3583 ± 0.0042	8010.1136	88.21 ± 1.13	-59.86 ± 1.13	0.5458 ± 0.0060
7802.2705	76.18 ± 1.08	-19.72 ± 1.08	0.1705 ± 0.0021	8010.1596	90.32 ± 1.23	-59.66 ± 1.23	0.5382 ± 0.0063
7987.5452	112.29 ± 1.32	-82.76 ± 1.32	0.3056 ± 0.0031	8010.2013	84.41 ± 1.03	-57.95 ± 1.03	0.5094 ± 0.0053
7988.4413	107.97 ± 1.20	-28.86 ± 1.20	0.3412 ± 0.0033	8010.2544	88.47 ± 1.07	-60.07 ± 1.07	0.5346 ± 0.0057
7989.4361	98.24 ± 1.28	-47.13 ± 1.28	0.3789 ± 0.0043	8010.2962	91.17 ± 1.15	-59.89 ± 1.15	0.5278 ± 0.0058
7990.4747	110.45 ± 1.18	-71.94 ± 1.18	0.3688 ± 0.0034	8010.3788	86.44 ± 0.86	-63.32 ± 0.86	0.5329 ± 0.0045
7990.5549	110.65 ± 1.28	-71.66 ± 1.28	0.3775 ± 0.0038	8011.3676	87.19 ± 0.77	-60.22 ± 0.77	0.4874 ± 0.0037
7990.6008	112.15 ± 1.30	-69.17 ± 1.30	0.3781 ± 0.0038	8011.4101	87.12 ± 0.79	-60.33 ± 0.79	0.4810 ± 0.0038
7991.4147	102.50 ± 0.97	-41.70 ± 0.97	0.4413 ± 0.0036	8011.4527	86.46 ± 0.71	-60.24 ± 0.71	0.4875 ± 0.0035
7991.4571	101.65 ± 1.15	-45.17 ± 1.15	0.4309 ± 0.0042	8011.4954	87.66 ± 0.74	-60.05 ± 0.74	0.4877 ± 0.0036
7992.4143	109.26 ± 1.27	-59.27 ± 1.27	0.4322 ± 0.0044	8012.3550	88.20 ± 0.89	-57.22 ± 0.89	0.4670 ± 0.0041
7992.4566	109.95 ± 1.32	-61.36 ± 1.32	0.4347 ± 0.0045	8012.3977	86.60 ± 0.92	-56.05 ± 0.92	0.4582 ± 0.0042
7992.4990	111.01 ± 1.29	-64.77 ± 1.29	0.4411 ± 0.0044	8012.4403	89.28 ± 0.89	-56.00 ± 0.89	0.4614 ± 0.0040
7992.5414	111.85 ± 1.29	-64.39 ± 1.29	0.4333 ± 0.0043	8012.4830	89.78 ± 0.89	-55.47 ± 0.89	0.4539 ± 0.0039
7992.5840	109.17 ± 1.22	-66.31 ± 1.22	0.4303 ± 0.0041	8013.3595	92.43 ± 1.33	-63.95 ± 1.33	0.4299 ± 0.0054
7992.6265	113.43 ± 1.28	-67.51 ± 1.28	0.4246 ± 0.0041	8013.4023	93.07 ± 1.21	-63.55 ± 1.21	0.4405 ± 0.0050
7993.4328	93.03 ± 1.64	-80.48 ± 1.64	0.3842 ± 0.0058	8014.1424	83.77 ± 1.36	-62.59 ± 1.36	0.4270 ± 0.0059
7994.4410	103.72 ± 0.90	-41.18 ± 0.90	0.4801 ± 0.0036	8014.1842	86.75 ± 1.10	-61.06 ± 1.10	0.4556 ± 0.0050
7994.4835	105.66 ± 0.98	-40.21 ± 0.98	0.4852 ± 0.0039	8015.3894	80.49 ± 0.69	-42.71 ± 0.69	0.4218 ± 0.0031
7994.5486	104.02 ± 1.02	-38.30 ± 1.02	0.4890 ± 0.0041	8015.4320	82.38 ± 0.75	-42.42 ± 0.75	0.4273 ± 0.0034
7995.4308	113.23 ± 1.38	-59.85 ± 1.38	0.4487 ± 0.0047	8015.4335	75.93 ± 1.04	-42.70 ± 1.04	0.4060 ± 0.0048
7995.4688	118.82 ± 1.34	-61.14 ± 1.34	0.4524 ± 0.0044	8016.0403	82.17 ± 1.08	-38.31 ± 1.08	0.4136 ± 0.0047
7995.5660	114.60 ± 1.34	-65.34 ± 1.34	0.4484 ± 0.0046	8016.0820	77.44 ± 1.04	-36.13 ± 1.04	0.4154 ± 0.0048
7997.4510	89.63 ± 1.12	-48.77 ± 1.12	0.4971 ± 0.0053	8016.1238	82.40 ± 1.08	-35.92 ± 1.08	0.4122 ± 0.0047
7998.4580	106.84 ± 1.26	-64.86 ± 1.26	0.5016 ± 0.0051	8016.1655	82.60 ± 1.01	-41.47 ± 1.01	0.4207 ± 0.0045
7998.4767	101.84 ± 1.14	-68.55 ± 1.14	0.5031 ± 0.0049	8016.3622	78.33 ± 1.29	-41.87 ± 1.29	0.3833 ± 0.0055
7998.7549	120.77 ± 2.21	-101.85 ± 2.21	0.4654 ± 0.0074	8016.4588	85.44 ± 1.06	-43.94 ± 1.06	0.3918 ± 0.0042
7999.4398	101.31 ± 0.84	-49.94 ± 0.84	0.5108 ± 0.0037	8016.5013	85.12 ± 1.02	-42.65 ± 1.02	0.3879 ± 0.0040
7999.4594	96.00 ± 1.00	-60.79 ± 1.00	0.4947 ± 0.0044	8017.0372	89.18 ± 2.35	-50.15 ± 2.35	0.3543 ± 0.0081
8000.1570	101.87 ± 1.13	-44.42 ± 1.13	0.5257 ± 0.0051	8017.0789	86.95 ± 1.95	-50.07 ± 1.95	0.3464 ± 0.0068
8000.1987	103.09 ± 1.01	-41.66 ± 1.01	0.5309 ± 0.0045	8017.1207	90.72 ± 1.78	-43.01 ± 1.78	0.3825 ± 0.0065
8000.2411	105.85 ± 1.44	-39.77 ± 1.44	0.5193 ± 0.0061	8017.2360	92.64 ± 1.57	-51.20 ± 1.57	0.3694 ± 0.0054
8000.4166	102.93 ± 1.04	-48.12 ± 1.04	0.5327 ± 0.0047	8017.2777	87.11 ± 1.42	-48.80 ± 1.42	0.3681 ± 0.0053
8001.4153	99.06 ± 1.15	-64.62 ± 1.15	0.4790 ± 0.0048	8017.3816	79.37 ± 1.33	-55.46 ± 1.33	0.3479 ± 0.0050
8001.4203	103.59 ± 1.03	-63.15 ± 1.03	0.4975 ± 0.0043	8017.4092	86.23 ± 0.94	-56.52 ± 0.94	0.3616 ± 0.0034
8001.4630	106.14 ± 1.13	-63.04 ± 1.13	0.4911 ± 0.0045	8017.4124	84.26 ± 0.61	-58.25 ± 0.61	0.3721 ± 0.0023
8001.5059	107.47 ± 1.17	-64.31 ± 1.17	0.4919 ± 0.0047	8017.4516	86.16 ± 1.56	-56.78 ± 1.56	0.3676 ± 0.0058
8002.3950	109.33 ± 1.12	-59.49 ± 1.12	0.5105 ± 0.0045	8018.3424	80.92 ± 0.92	-49.60 ± 0.92	0.3798 ± 0.0038
8003.0934	101.27 ± 1.17	-50.01 ± 1.17	0.5189 ± 0.0052	8018.4112	77.76 ± 1.54	-45.71 ± 1.54	0.3518 ± 0.0060
8003.1351	102.00 ± 0.99	-51.33 ± 0.99	0.5271 ± 0.0044	8018.4862	82.88 ± 0.87	-56.19 ± 0.87	0.3795 ± 0.0034
8003.1768	107.05 ± 1.25	-51.89 ± 1.25	0.5020 ± 0.0051	8018.4862	80.52 ± 0.74	-52.19 ± 0.74	0.3709 ± 0.0029
8003.2186	102.66 ± 1.15	-52.05 ± 1.15	0.5178 ± 0.0050	8019.0403	93.17 ± 1.54	-50.94 ± 1.54	0.3305 ± 0.0047
8004.4058	92.23 ± 0.86	-66.03 ± 0.86	0.5170 ± 0.0042	8019.0820	84.03 ± 1.69	-52.03 ± 1.69	0.3245 ± 0.0056
8004.4185	95.57 ± 0.71	-54.40 ± 0.71	0.5416 ± 0.0035	8019.1238	89.61 ± 1.48	-51.31 ± 1.48	0.3224 ± 0.0046
8005.4141	92.16 ± 1.31	-41.51 ± 1.31	0.5020 ± 0.0062	8019.1655	90.93 ± 1.27	-48.25 ± 1.27	0.3185 ± 0.0039
8006.5533	101.20 ± 0.92	-64.91 ± 0.92	0.5409 ± 0.0043	8019.2443	94.78 ± 1.42	-47.51 ± 1.42	0.3146 ± 0.0041
8006.5762	102.18 ± 0.94	-69.54 ± 0.94	0.5291 ± 0.0042	8019.2860	89.86 ± 1.32	-49.98 ± 1.32	0.3241 ± 0.0042
8007.0402	99.95 ± 1.13	-58.73 ± 1.13	0.5170 ± 0.0051	8019.3278	92.14 ± 1.30	-45.78 ± 1.30	0.3327 ± 0.0041
8007.1411	94.17 ± 1.36	-63.02 ± 1.36	0.5236 ± 0.0066	8019.3480	88.22 ± 1.14	-49.59 ± 1.14	0.3154 ± 0.0035
8007.3813	97.17 ± 0.85	-64.55 ± 0.85	0.5439 ± 0.0041	8019.3906	89.57 ± 1.00	-48.77 ± 1.00	0.3267 ± 0.0032
8007.5085	99.45 ± 1.30	-86.76 ± 1.30	0.5116 ± 0.0058	8019.4335	88.61 ± 1.00	-46.72 ± 1.00	0.3223 ± 0.0031
8008.0459	87.72 ± 0.94	-48.01 ± 0.94	0.5704 ± 0.0053	8019.4764	90.15 ± 1.01	-47.20 ± 1.01	0.3273 ± 0.0032
8008.0917	88.74 ± 1.01	-51.27 ± 1.01	0.5851 ± 0.0058	8019.5190	90.40 ± 1.04	-45.90 ± 1.04	0.3296 ± 0.0033
8008.1374	88.90 ± 0.99	-49.03 ± 0.99	0.5680 ± 0.0055	8020.3865	80.36 ± 1.02	-36.64 ± 1.02	0.3429 ± 0.0038
8008.4270	89.49 ± 1.07	-48.97 ± 1.07	0.5495 ± 0.0057	8020.4292	80.07 ± 0.88	-39.50 ± 0.88	0.3528 ± 0.0033
8008.5496	101.37 ± 1.37	-68.83 ± 1.37	0.5377 ± 0.0063	8020.4721	81.28 ± 1.13	-36.89 ± 1.13	0.3478 ± 0.0042
8009.4014	96.40 ± 0.81	-54.24 ± 0.81	0.5256 ± 0.0038	8021.3369	75.86 ± 0.78	-54.53 ± 0.78	0.3217 ± 0.0028
8009.4014	94.04 ± 0.74	-45.99 ± 0.74	0.5120 ± 0.0035	8021.3797	75.53 ± 0.74	-56.19 ± 0.74	0.3243 ± 0.0028
8009.4070	95.30 ± 0.79	-56.52 ± 0.79	0.5137 ± 0.0037	8021.4226	77.70 ± 0.66	-55.07 ± 0.66	0.3207 ± 0.0024
8009.4350	88.14 ± 1.18	-55.43 ± 1.18	0.4851 ± 0.0056	8021.4655	76.79 ± 0.68	-54.87 ± 0.68	0.3262 ± 0.0025
8009.4496	93.13 ± 0.83	-56.69 ± 0.83	0.5086 ± 0.0039	8021.5084	74.53 ± 0.71	-57.52 ± 0.71	0.3211 ± 0.0026
8009.4922	93.91 ± 0.84	-58.08 ± 0.84	0.5118 ± 0.0039	8022.4587	75.25 ± 0.70	-64.78 ± 0.70	0.3076 ± 0.0024
8009.5823	98.75 ± 1.32	-84.42 ± 1.32	0.4917 ± 0.0057	8023.3396	86.44 ± 1.65	-59.07 ± 1.65	0.2893 ± 0.0047

Table B4 – *continued* H α Gaussian Parameters for Excess Emission. The HJD column is HJD - 2,450,000.

HJD	FWHM (km s ⁻¹)	Center (km s ⁻¹)	Height (Norm. Flux)	HJD	FWHM (km s ⁻¹)	Center (km s ⁻¹)	Height (Norm. Flux)
8023.3975	80.70 ± 1.87	-56.59 ± 1.87	0.2667 ± 0.0055	8180.6390	98.62 ± 0.67	-63.28 ± 0.67	0.5474 ± 0.0032
8024.3935	84.62 ± 1.20	-47.65 ± 1.20	0.2990 ± 0.0036	8181.2967	102.23 ± 0.65	-61.22 ± 0.65	0.5463 ± 0.0030
8024.4651	82.67 ± 1.06	-48.12 ± 1.06	0.3019 ± 0.0034	8181.5151	104.28 ± 0.65	-49.01 ± 0.65	0.5378 ± 0.0029
8025.3454	71.55 ± 0.87	-40.39 ± 0.87	0.3224 ± 0.0034	8181.5399	100.77 ± 0.50	-47.49 ± 0.50	0.5350 ± 0.0023
8025.3745	66.27 ± 1.06	-42.03 ± 1.06	0.3135 ± 0.0044	8181.5640	102.85 ± 0.52	-46.98 ± 0.52	0.5357 ± 0.0023
8025.3880	71.35 ± 0.85	-37.83 ± 0.85	0.3204 ± 0.0033	8181.5879	103.40 ± 0.50	-45.86 ± 0.50	0.5331 ± 0.0022
8025.4309	72.41 ± 0.83	-39.87 ± 0.83	0.3152 ± 0.0031	8182.5423	104.44 ± 0.60	-33.70 ± 0.60	0.5236 ± 0.0026
8025.4739	74.41 ± 0.95	-38.77 ± 0.95	0.3083 ± 0.0034	8182.5653	106.06 ± 0.64	-33.12 ± 0.64	0.5306 ± 0.0028
8026.3308	72.73 ± 0.78	-31.84 ± 0.78	0.2968 ± 0.0028	8182.5869	105.59 ± 0.63	-32.21 ± 0.63	0.5235 ± 0.0027
8026.3733	74.21 ± 0.82	-31.00 ± 0.82	0.3027 ± 0.0029	8183.6155	99.14 ± 0.60	-66.40 ± 0.60	0.5830 ± 0.0031
8026.4012	66.77 ± 1.24	-29.02 ± 1.24	0.2672 ± 0.0044	8188.5727	104.58 ± 0.72	-30.53 ± 0.72	0.6275 ± 0.0037
8026.4026	73.68 ± 0.83	-28.47 ± 0.83	0.2881 ± 0.0028	8189.5427	105.29 ± 0.50	-43.62 ± 0.50	0.6082 ± 0.0025
8026.4160	73.68 ± 0.78	-28.74 ± 0.78	0.2976 ± 0.0027	8189.5649	106.47 ± 0.38	-45.06 ± 0.38	0.6042 ± 0.0019
8029.6129	70.81 ± 1.12	-60.70 ± 1.12	0.2675 ± 0.0037	8190.6213	95.17 ± 0.51	-52.30 ± 0.51	0.6773 ± 0.0031
8031.3385	83.57 ± 1.18	-37.52 ± 1.18	0.2152 ± 0.0026	8191.2859	95.74 ± 0.53	-46.77 ± 0.53	0.6760 ± 0.0032
8032.3226	69.47 ± 0.86	-40.84 ± 0.86	0.2332 ± 0.0025	8192.5247	99.87 ± 0.48	-43.79 ± 0.48	0.6420 ± 0.0027
8033.3153	77.75 ± 1.12	-41.76 ± 1.12	0.1928 ± 0.0024	8193.5283	102.45 ± 0.87	-43.73 ± 0.87	0.6613 ± 0.0048
8033.3578	75.45 ± 1.09	-41.02 ± 1.09	0.1883 ± 0.0024	8197.6118	88.72 ± 0.84	-61.79 ± 0.84	0.6691 ± 0.0054
8033.4005	85.37 ± 1.16	-38.90 ± 1.16	0.1922 ± 0.0023	8198.3040	90.87 ± 0.45	-51.93 ± 0.45	0.6683 ± 0.0029
8035.3558	82.90 ± 1.22	-47.23 ± 1.22	0.1963 ± 0.0025	8199.3425	91.10 ± 0.86	-39.98 ± 0.86	0.5767 ± 0.0047
8035.3985	81.40 ± 1.22	-41.38 ± 1.22	0.1932 ± 0.0025	8201.5293	88.57 ± 0.35	-47.31 ± 0.35	0.6006 ± 0.0021
8035.4416	85.01 ± 1.27	-46.73 ± 1.27	0.1938 ± 0.0025	8208.5546	82.92 ± 0.46	-50.32 ± 0.46	0.5494 ± 0.0026
8036.2965	73.82 ± 1.12	-45.03 ± 1.12	0.1908 ± 0.0025	8341.5381	223.03 ± 6.66	29.95 ± 6.61	0.0811 ± 0.0021
8036.3393	76.75 ± 1.08	-46.18 ± 1.08	0.1910 ± 0.0023	8345.5266	143.20 ± 2.88	-53.25 ± 2.88	0.1568 ± 0.0028
8036.3827	77.27 ± 1.24	-44.54 ± 1.24	0.1944 ± 0.0027	8346.4356	175.96 ± 2.19	-66.60 ± 2.19	0.2288 ± 0.0025
8036.4258	77.93 ± 1.27	-42.29 ± 1.27	0.1925 ± 0.0027	8346.4918	130.94 ± 4.16	-71.42 ± 4.16	0.1602 ± 0.0045
8036.4688	80.76 ± 1.45	-45.45 ± 1.45	0.1859 ± 0.0029	8346.5031	113.03 ± 2.54	-94.23 ± 2.54	0.1854 ± 0.0036
8037.2970	84.60 ± 1.35	-42.24 ± 1.35	0.1864 ± 0.0026	8346.5752	125.23 ± 2.73	-86.57 ± 2.73	0.1843 ± 0.0035
8037.3255	82.10 ± 1.37	-33.80 ± 1.37	0.1786 ± 0.0026	8346.6401	121.51 ± 2.80	-81.51 ± 2.80	0.1853 ± 0.0037
8037.3684	89.10 ± 1.70	-33.78 ± 1.70	0.1818 ± 0.0030	8347.4435	158.45 ± 2.10	-34.53 ± 2.10	0.2656 ± 0.0030
8037.4113	85.74 ± 1.65	-30.90 ± 1.65	0.1859 ± 0.0031	8347.4832	170.15 ± 3.57	-7.97 ± 3.57	0.2713 ± 0.0050
8037.4543	82.28 ± 1.51	-31.26 ± 1.51	0.1794 ± 0.0029	8347.5657	122.76 ± 2.03	-10.99 ± 2.03	0.2785 ± 0.0040
8038.3054	82.36 ± 1.32	-31.20 ± 1.32	0.1731 ± 0.0024	8348.4560	169.96 ± 3.36	-60.37 ± 3.36	0.2335 ± 0.0040
8038.3484	76.97 ± 1.16	-32.40 ± 1.16	0.1767 ± 0.0023	8349.3928	121.69 ± 3.47	-69.46 ± 3.47	0.2241 ± 0.0056
8038.3913	79.06 ± 1.33	-33.39 ± 1.33	0.1757 ± 0.0026	8349.4227	124.77 ± 2.27	-77.40 ± 2.27	0.2614 ± 0.0041
8038.4343	83.80 ± 1.26	-33.96 ± 1.26	0.1739 ± 0.0023	8349.5208	140.16 ± 2.63	-76.24 ± 2.63	0.2656 ± 0.0044
8039.4211	75.05 ± 1.16	-45.69 ± 1.16	0.1783 ± 0.0024	8349.5637	127.40 ± 2.06	-70.03 ± 2.06	0.2592 ± 0.0036
8040.3018	98.75 ± 1.93	-39.49 ± 1.93	0.1450 ± 0.0025	8350.4430	142.88 ± 2.70	-17.72 ± 2.70	0.3452 ± 0.0057
8040.3305	95.37 ± 2.11	-36.42 ± 2.11	0.1313 ± 0.0025	8350.4797	101.46 ± 1.53	-18.94 ± 1.53	0.3257 ± 0.0043
8040.3424	99.35 ± 2.73	-38.26 ± 2.73	0.1290 ± 0.0031	8350.4903	125.04 ± 1.97	-19.50 ± 1.97	0.3439 ± 0.0047
8040.3446	99.35 ± 2.07	-37.71 ± 2.07	0.1470 ± 0.0027	8350.5061	139.99 ± 2.64	-18.82 ± 2.64	0.3466 ± 0.0057
8040.3876	99.84 ± 2.19	-35.06 ± 2.19	0.1440 ± 0.0027	8350.5475	110.48 ± 1.69	-17.04 ± 1.69	0.3360 ± 0.0045
8040.4306	99.85 ± 2.02	-36.32 ± 2.02	0.1406 ± 0.0025	8350.5689	136.25 ± 2.63	-18.99 ± 2.63	0.3525 ± 0.0060
8041.4267	84.21 ± 1.38	-41.30 ± 1.38	0.1610 ± 0.0023	8351.4384	132.62 ± 1.63	-60.30 ± 1.63	0.3334 ± 0.0035
8042.2766	81.14 ± 1.25	-37.14 ± 1.25	0.1627 ± 0.0022	8351.5391	119.56 ± 1.49	-67.05 ± 1.49	0.3332 ± 0.0036
8042.3477	86.28 ± 1.53	-36.52 ± 1.53	0.1610 ± 0.0025	8351.5541	120.86 ± 1.22	-71.41 ± 1.22	0.3145 ± 0.0027
8042.4189	80.49 ± 1.42	-36.42 ± 1.42	0.1658 ± 0.0025	8352.4009	116.13 ± 1.96	-77.45 ± 1.96	0.3065 ± 0.0044
8044.3556	89.86 ± 1.45	-46.86 ± 1.45	0.1451 ± 0.0020	8352.4389	129.67 ± 1.62	-64.66 ± 1.62	0.3129 ± 0.0034
8044.3556	88.64 ± 1.45	-44.50 ± 1.45	0.1452 ± 0.0021	8352.4421	133.91 ± 1.79	-65.91 ± 1.79	0.3136 ± 0.0036
8044.3986	92.65 ± 1.56	-48.15 ± 1.56	0.1447 ± 0.0021	8352.5396	129.21 ± 2.03	-55.86 ± 2.03	0.3103 ± 0.0042
8045.5903	96.06 ± 3.32	-33.18 ± 3.32	0.3240 ± 0.0099	8353.4969	105.59 ± 1.37	-10.24 ± 1.37	0.3673 ± 0.0041
8050.0804	73.44 ± 2.89	-17.69 ± 2.89	0.1272 ± 0.0044	8354.2001	119.04 ± 1.62	-30.17 ± 1.62	0.3702 ± 0.0043
8050.2637	68.30 ± 1.78	-13.22 ± 1.78	0.1431 ± 0.0032	8355.1780	128.17 ± 1.73	-51.85 ± 1.73	0.3743 ± 0.0044
8050.3657	68.49 ± 1.80	-10.19 ± 1.80	0.1413 ± 0.0031	8356.4734	123.70 ± 1.73	-31.03 ± 1.73	0.4312 ± 0.0052
8051.4800	71.95 ± 2.36	-9.74 ± 2.36	0.1153 ± 0.0034	8357.4494	140.66 ± 2.23	-61.21 ± 2.23	0.4709 ± 0.0064
8057.4159	24.26 ± 2.44	-49.44 ± 2.44	0.0724 ± 0.0060	8357.5413	109.41 ± 1.09	-64.02 ± 1.09	0.4449 ± 0.0038
8090.0433	12.47 ± 1.59	403.33 ± 1.59	0.1338 ± 0.0142	8357.5837	112.29 ± 1.18	-64.43 ± 1.18	0.4487 ± 0.0041
8175.5618	126.63 ± 1.87	-94.97 ± 1.87	0.3968 ± 0.0051	8358.4326	127.43 ± 1.42	-45.38 ± 1.41	0.4741 ± 0.0045
8176.5078	115.80 ± 1.49	-31.39 ± 1.49	0.4719 ± 0.0053	8358.4607	116.69 ± 0.96	-46.18 ± 0.96	0.4372 ± 0.0031
8176.5764	99.12 ± 0.68	-38.84 ± 0.68	0.4457 ± 0.0026	8358.5246	118.95 ± 1.06	-44.71 ± 1.06	0.4463 ± 0.0034
8180.2561	101.77 ± 0.68	-43.30 ± 0.68	0.5445 ± 0.0032	8359.4581	110.49 ± 1.30	-37.83 ± 1.30	0.4384 ± 0.0045
8180.2874	104.82 ± 0.79	-52.11 ± 0.79	0.5602 ± 0.0036	8359.4907	123.41 ± 1.50	-41.04 ± 1.50	0.4722 ± 0.0050
8180.5154	104.53 ± 0.76	-51.84 ± 0.76	0.5190 ± 0.0032	8360.1777	116.69 ± 1.31	-61.47 ± 1.31	0.4287 ± 0.0042
8180.5386	105.40 ± 0.82	-50.60 ± 0.82	0.5141 ± 0.0034	8362.4822	108.19 ± 0.97	-41.88 ± 0.97	0.4810 ± 0.0037
8180.5607	97.82 ± 0.55	-53.45 ± 0.55	0.5406 ± 0.0026	8363.4630	115.39 ± 1.20	-55.69 ± 1.20	0.5279 ± 0.0047

Table B4 – continued H α Gaussian Parameters for Excess Emission. The HJD column is HJD - 2,450,000.

HJD	FWHM (km s ⁻¹)	Center (km s ⁻¹)	Height (Norm. Flux)	HJD	FWHM (km s ⁻¹)	Center (km s ⁻¹)	Height (Norm. Flux)
8363.4887	112.55 ± 1.09	-56.35 ± 1.09	0.4968 ± 0.0042	8411.3838	96.49 ± 1.29	-21.23 ± 1.29	0.4171 ± 0.0049
8363.5459	112.85 ± 1.09	-58.10 ± 1.09	0.4867 ± 0.0040	8411.4720	92.56 ± 0.97	-21.61 ± 0.97	0.4178 ± 0.0038
8364.4272	118.51 ± 1.50	-40.44 ± 1.50	0.5119 ± 0.0056	8412.3715	107.74 ± 1.35	-46.92 ± 1.35	0.4249 ± 0.0046
8364.5478	100.07 ± 0.53	-44.82 ± 0.53	0.4773 ± 0.0022	8412.4934	100.16 ± 0.75	-52.13 ± 0.75	0.3953 ± 0.0026
8365.4541	106.45 ± 0.93	-46.99 ± 0.93	0.4833 ± 0.0036	8413.4110	96.75 ± 1.09	-50.58 ± 1.09	0.4637 ± 0.0045
8366.4522	107.63 ± 0.94	-52.43 ± 0.94	0.4676 ± 0.0036	8415.2834	102.59 ± 1.22	-54.02 ± 1.22	0.4973 ± 0.0051
8368.4562	94.63 ± 0.77	-44.10 ± 0.77	0.4958 ± 0.0035	8416.4004	98.64 ± 0.96	-58.76 ± 0.96	0.5017 ± 0.0042
8369.1768	105.80 ± 1.09	-40.82 ± 1.09	0.4398 ± 0.0039	8417.3037	92.98 ± 0.91	-37.84 ± 0.91	0.5367 ± 0.0045
8369.4500	107.65 ± 1.17	-41.11 ± 1.17	0.4357 ± 0.0041	8426.3364	99.24 ± 0.96	-52.15 ± 0.96	0.6174 ± 0.0051
8370.1537	105.98 ± 1.45	-41.84 ± 1.45	0.4314 ± 0.0051	8428.3085	105.96 ± 1.05	-43.89 ± 1.05	0.6095 ± 0.0052
8370.4057	109.84 ± 1.65	-45.83 ± 1.65	0.4767 ± 0.0062	8429.3295	101.36 ± 0.78	-63.07 ± 0.78	0.5848 ± 0.0039
8370.4549	101.48 ± 1.29	-47.98 ± 1.29	0.4466 ± 0.0049	8432.2991	105.59 ± 0.93	-52.00 ± 0.93	0.5381 ± 0.0041
8371.4276	94.39 ± 1.15	-54.41 ± 1.15	0.4235 ± 0.0044	8434.2726	91.36 ± 0.65	-40.94 ± 0.65	0.5981 ± 0.0037
8372.4785	98.66 ± 1.15	-48.48 ± 1.15	0.4153 ± 0.0042	8436.3603	98.07 ± 0.80	-51.40 ± 0.80	0.5849 ± 0.0041
8372.4872	101.14 ± 1.13	-52.35 ± 1.13	0.4192 ± 0.0040	8436.7523	93.69 ± 0.65	-51.46 ± 0.65	0.5852 ± 0.0035
8373.4747	110.81 ± 1.69	-50.93 ± 1.69	0.3949 ± 0.0053	8437.3468	93.92 ± 0.77	-49.51 ± 0.77	0.5955 ± 0.0042
8373.4764	107.48 ± 0.86	-55.70 ± 0.86	0.3970 ± 0.0028	8438.3249	99.59 ± 0.81	-53.50 ± 0.81	0.5638 ± 0.0040
8373.4894	103.50 ± 1.78	-47.19 ± 1.78	0.3815 ± 0.0057	8438.4520	94.86 ± 0.80	-55.01 ± 0.80	0.5281 ± 0.0038
8373.5119	104.29 ± 1.46	-44.85 ± 1.46	0.3955 ± 0.0048	8441.2923	92.89 ± 0.83	-56.61 ± 0.83	0.5613 ± 0.0043
8374.3180	99.34 ± 1.40	-57.04 ± 1.40	0.4322 ± 0.0053	8441.2979	94.15 ± 0.77	-52.33 ± 0.77	0.5811 ± 0.0041
8376.4731	100.59 ± 1.37	-36.32 ± 1.37	0.3614 ± 0.0043	8441.4463	95.77 ± 0.79	-51.07 ± 0.79	0.5774 ± 0.0041
8377.4148	104.07 ± 1.81	-54.32 ± 1.81	0.3670 ± 0.0054	8441.4473	93.41 ± 0.48	-48.58 ± 0.48	0.5575 ± 0.0025
8377.4630	111.16 ± 1.96	-52.02 ± 1.96	0.3825 ± 0.0059	8443.4107	96.67 ± 0.89	-56.84 ± 0.89	0.5246 ± 0.0042
8377.4921	98.78 ± 1.34	-53.27 ± 1.34	0.3651 ± 0.0043	8444.3055	88.03 ± 0.53	-50.04 ± 0.53	0.5590 ± 0.0029
8378.3923	99.44 ± 1.28	-50.52 ± 1.28	0.4034 ± 0.0045	8449.7260	98.43 ± 1.32	-57.70 ± 1.32	0.4758 ± 0.0055
8378.5057	89.60 ± 0.81	-48.13 ± 0.81	0.3734 ± 0.0029	8451.3159	89.86 ± 0.99	-52.88 ± 0.99	0.4821 ± 0.0046
8379.3695	107.01 ± 1.84	-38.08 ± 1.84	0.3501 ± 0.0052	8453.3599	92.28 ± 1.37	-47.99 ± 1.37	0.4498 ± 0.0057
8379.5082	98.74 ± 1.57	-36.91 ± 1.57	0.3323 ± 0.0046	8454.2752	83.13 ± 0.88	-53.63 ± 0.88	0.4740 ± 0.0044
8381.3982	93.91 ± 1.36	-44.85 ± 1.36	0.3487 ± 0.0044	8457.3021	83.23 ± 0.88	-54.98 ± 0.88	0.4261 ± 0.0039
8381.4493	88.28 ± 1.30	-42.65 ± 1.30	0.3238 ± 0.0041	8460.4178	91.04 ± 1.56	-54.79 ± 1.56	0.3805 ± 0.0056
8385.5020	82.30 ± 0.84	-52.20 ± 0.84	0.2687 ± 0.0024	8463.4456	90.31 ± 0.83	-44.73 ± 0.83	0.3567 ± 0.0028
8386.4720	94.24 ± 1.20	-48.97 ± 1.20	0.2398 ± 0.0026	8470.2521	86.88 ± 1.36	-41.80 ± 1.36	0.2821 ± 0.0038
8387.3004	101.28 ± 1.60	-46.93 ± 1.60	0.2487 ± 0.0034	8478.3307	95.06 ± 2.08	-51.08 ± 2.08	0.2537 ± 0.0048
8387.3740	107.09 ± 1.95	-43.66 ± 1.95	0.2608 ± 0.0041	8479.2329	68.48 ± 1.66	-51.61 ± 1.66	0.2135 ± 0.0046
8387.4332	94.13 ± 1.12	-47.66 ± 1.12	0.2452 ± 0.0025	8480.2246	85.74 ± 1.52	-49.23 ± 1.52	0.2302 ± 0.0035
8387.4548	90.88 ± 1.45	-46.93 ± 1.45	0.2325 ± 0.0033	8480.2827	79.58 ± 1.32	-53.50 ± 1.32	0.2122 ± 0.0030
8388.3864	94.68 ± 1.77	-52.37 ± 1.77	0.2572 ± 0.0041	8483.2416	70.69 ± 1.11	-51.56 ± 1.11	0.2210 ± 0.0030
8388.4121	81.39 ± 0.84	-47.02 ± 0.84	0.2453 ± 0.0022	8486.7017	77.60 ± 1.34	-51.72 ± 1.34	0.1949 ± 0.0029
8389.4065	84.49 ± 1.08	-49.55 ± 1.08	0.2074 ± 0.0023	8487.3411	75.42 ± 0.87	-59.36 ± 0.87	0.1803 ± 0.0018
8389.4521	93.10 ± 1.41	-45.55 ± 1.41	0.2204 ± 0.0029	8492.4135	69.25 ± 1.19	-49.00 ± 1.19	0.1495 ± 0.0022
8390.4486	94.28 ± 1.54	-38.87 ± 1.54	0.1984 ± 0.0028	8494.6523	75.94 ± 1.77	-77.82 ± 1.77	0.1610 ± 0.0032
8391.4717	99.88 ± 1.95	-35.13 ± 1.95	0.2075 ± 0.0035	8505.2566	287.50 ± 9.86	-86.86 ± 9.25	0.0675 ± 0.0020
8392.3825	79.08 ± 1.85	-40.39 ± 1.85	0.2323 ± 0.0046	8520.2811	952.35 ± 156.79	-63.98 ± 54.96	0.0386 ± 0.0010
8394.3794	117.49 ± 3.19	-62.62 ± 3.19	0.1635 ± 0.0039	8764.4331	93.31 ± 1.49	-11.22 ± 1.49	0.2966 ± 0.0041
8395.4098	74.17 ± 1.04	-52.14 ± 1.04	0.1918 ± 0.0023	8766.3172	91.15 ± 0.74	-72.15 ± 0.74	0.3465 ± 0.0024
8397.3892	143.92 ± 3.57	-63.03 ± 3.57	0.1394 ± 0.0030	8766.3652	88.38 ± 0.63	-70.35 ± 0.63	0.3363 ± 0.0021
8399.6737	63.25 ± 1.28	-33.50 ± 1.28	0.1772 ± 0.0030	8766.4357	92.97 ± 1.02	-67.17 ± 1.02	0.3512 ± 0.0033
8400.3271	134.25 ± 3.58	-53.65 ± 3.58	0.1389 ± 0.0033	8767.3710	94.11 ± 0.84	-33.81 ± 0.84	0.3918 ± 0.0030
8400.3886	89.27 ± 2.14	-51.85 ± 2.14	0.1477 ± 0.0031	8767.3740	88.45 ± 0.84	-25.84 ± 0.84	0.3834 ± 0.0032
8401.4106	256.09 ± 6.78	-45.92 ± 6.58	0.0960 ± 0.0022	8767.4553	94.71 ± 1.02	-34.92 ± 1.02	0.3919 ± 0.0037
8402.3614	169.28 ± 3.96	-18.66 ± 3.96	0.1288 ± 0.0027	8768.3466	95.05 ± 0.80	-51.52 ± 0.80	0.3851 ± 0.0028
8404.4002	92.75 ± 1.45	-64.66 ± 1.45	0.1968 ± 0.0026	8768.4380	98.52 ± 0.71	-56.52 ± 0.71	0.3785 ± 0.0023
8405.3428	88.27 ± 1.19	-20.01 ± 1.19	0.2263 ± 0.0026	8769.3668	96.32 ± 1.06	-65.54 ± 1.06	0.4344 ± 0.0041
8407.4325	111.21 ± 1.91	-74.30 ± 1.91	0.2963 ± 0.0044	8769.3878	92.51 ± 1.10	-62.08 ± 1.10	0.4437 ± 0.0045
8407.5264	98.82 ± 0.99	-70.26 ± 0.99	0.2786 ± 0.0024	8769.3947	90.48 ± 0.76	-68.75 ± 0.76	0.4299 ± 0.0031
8408.3608	112.59 ± 1.78	-23.22 ± 1.78	0.3257 ± 0.0045	8769.6369	90.39 ± 0.91	-64.15 ± 0.91	0.4380 ± 0.0038
8408.4154	111.68 ± 1.82	-23.45 ± 1.82	0.3377 ± 0.0048	8770.3383	83.54 ± 0.66	-44.80 ± 0.66	0.4655 ± 0.0032
8409.1540	90.50 ± 1.30	-45.73 ± 1.30	0.3291 ± 0.0041	8770.4203	88.95 ± 0.74	-41.53 ± 0.74	0.4730 ± 0.0034
8409.3058	91.98 ± 1.19	-49.54 ± 1.19	0.3380 ± 0.0037	8770.4298	82.34 ± 0.58	-43.07 ± 0.58	0.4747 ± 0.0029
8409.5829	97.11 ± 0.94	-60.36 ± 0.94	0.3185 ± 0.0027	8770.7000	81.32 ± 0.75	-37.95 ± 0.75	0.4840 ± 0.0038
8410.3355	110.74 ± 1.44	-59.32 ± 1.44	0.3651 ± 0.0041	8771.0380	77.13 ± 1.23	-39.26 ± 1.23	0.5290 ± 0.0072
8410.4964	100.26 ± 0.84	-52.57 ± 0.84	0.3505 ± 0.0025	8771.3032	98.76 ± 1.26	-49.30 ± 1.26	0.4644 ± 0.0051
8411.3265	105.30 ± 1.57	-22.14 ± 1.57	0.4163 ± 0.0054	8771.6480	103.41 ± 0.86	-60.82 ± 0.86	0.4341 ± 0.0031

Table B4 – *continued* H α Gaussian Parameters for Excess Emission. The HJD column is HJD - 2,450,000.

HJD	FWHM (km s ⁻¹)	Center (km s ⁻¹)	Height (Norm. Flux)	HJD	FWHM (km s ⁻¹)	Center (km s ⁻¹)	Height (Norm. Flux)
8772.8639	92.95 ± 0.87	-52.88 ± 0.87	0.5580 ± 0.0045	8848.2818	79.60 ± 0.62	-38.90 ± 0.62	0.3463 ± 0.0023
8772.9158	92.50 ± 0.82	-51.86 ± 0.82	0.5670 ± 0.0043	8848.3183	77.83 ± 0.73	-36.81 ± 0.73	0.3586 ± 0.0029
8773.6991	82.31 ± 0.61	-46.58 ± 0.61	0.5716 ± 0.0036	8849.2524	87.28 ± 0.84	-75.06 ± 0.84	0.3437 ± 0.0029
8774.6085	97.70 ± 1.01	-56.33 ± 1.01	0.5268 ± 0.0047	8849.3407	84.72 ± 0.67	-70.49 ± 0.67	0.3464 ± 0.0024
8774.6842	94.22 ± 0.61	-55.84 ± 0.61	0.5386 ± 0.0030	8849.6030	77.59 ± 0.56	-67.39 ± 0.56	0.3581 ± 0.0022
8775.6183	97.63 ± 0.76	-46.97 ± 0.76	0.5788 ± 0.0039	8852.6931	86.04 ± 0.82	-50.43 ± 0.82	0.4181 ± 0.0035
8777.6303	91.71 ± 0.80	-56.52 ± 0.80	0.6565 ± 0.0049	8855.3400	87.51 ± 0.54	-63.69 ± 0.54	0.4413 ± 0.0023
8778.6482	101.86 ± 0.80	-42.69 ± 0.80	0.6464 ± 0.0044	8855.6228	85.09 ± 0.67	-58.89 ± 0.67	0.4646 ± 0.0032
8778.6800	96.34 ± 0.53	-43.33 ± 0.53	0.6253 ± 0.0029	8855.7246	87.41 ± 0.84	-52.61 ± 0.84	0.4804 ± 0.0040
8779.6359	97.26 ± 0.72	-56.28 ± 0.72	0.6765 ± 0.0043	8857.3505	83.69 ± 0.49	-50.88 ± 0.49	0.5091 ± 0.0026
8782.3610	102.47 ± 0.68	-57.03 ± 0.68	0.6471 ± 0.0037	8857.6647	88.73 ± 1.10	-55.99 ± 1.10	0.5582 ± 0.0060
8782.4243	102.14 ± 0.68	-60.19 ± 0.68	0.6411 ± 0.0037	8860.3785	81.99 ± 0.38	-55.71 ± 0.38	0.5742 ± 0.0023
8783.3183	92.29 ± 0.70	-66.78 ± 0.70	0.6945 ± 0.0045	8860.6762	79.46 ± 0.34	-56.28 ± 0.34	0.5614 ± 0.0021
8783.4027	94.02 ± 0.67	-64.37 ± 0.67	0.6938 ± 0.0043	8860.7032	84.39 ± 0.70	-55.39 ± 0.70	0.6031 ± 0.0043
8784.4023	98.85 ± 0.61	-34.76 ± 0.61	0.7008 ± 0.0037	8861.6973	93.78 ± 0.84	-40.44 ± 0.84	0.5936 ± 0.0046
8786.5178	99.96 ± 0.34	-60.17 ± 0.34	0.6576 ± 0.0020	8862.3654	82.40 ± 0.55	-42.42 ± 0.55	0.6236 ± 0.0036
8789.8308	102.54 ± 0.87	-45.25 ± 0.87	0.7088 ± 0.0052	8863.4157	86.13 ± 0.59	-54.76 ± 0.59	0.6133 ± 0.0036
8792.6222	101.06 ± 0.79	-44.13 ± 0.79	0.7121 ± 0.0048	8864.3923	90.51 ± 0.64	-39.52 ± 0.64	0.6593 ± 0.0040
8792.8348	100.03 ± 0.79	-46.86 ± 0.79	0.7089 ± 0.0049	8865.2392	78.59 ± 0.52	-39.90 ± 0.52	0.6815 ± 0.0039
8793.4263	96.79 ± 0.55	-54.72 ± 0.55	0.6799 ± 0.0033	8865.6929	88.12 ± 0.67	-48.30 ± 0.67	0.6760 ± 0.0044
8794.2807	90.37 ± 0.57	-59.60 ± 0.57	0.7099 ± 0.0039	8866.6311	83.06 ± 0.69	-60.68 ± 0.69	0.7298 ± 0.0052
8794.3721	90.23 ± 0.46	-57.45 ± 0.46	0.7165 ± 0.0032	8867.2999	86.24 ± 0.47	-50.80 ± 0.47	0.6896 ± 0.0033
8795.3236	98.27 ± 0.83	-37.14 ± 0.83	0.6946 ± 0.0050	8867.6440	86.56 ± 0.61	-46.66 ± 0.61	0.7172 ± 0.0044
8799.6288	95.02 ± 0.89	-50.64 ± 0.89	0.6458 ± 0.0052	8868.2618	95.01 ± 0.78	-52.65 ± 0.78	0.6812 ± 0.0048
8799.8145	94.44 ± 0.91	-53.40 ± 0.91	0.6352 ± 0.0053	8868.3617	94.42 ± 0.87	-52.57 ± 0.87	0.6722 ± 0.0053
8800.4499	89.62 ± 0.68	-53.69 ± 0.68	0.6155 ± 0.0040	8871.6549	93.98 ± 0.73	-54.52 ± 0.73	0.6380 ± 0.0043
8800.6136	89.03 ± 0.86	-55.43 ± 0.86	0.6345 ± 0.0053	8872.2378	104.22 ± 1.12	-59.02 ± 1.12	0.6293 ± 0.0058
8801.6310	91.29 ± 0.91	-47.24 ± 0.91	0.6192 ± 0.0053	8872.6572	94.87 ± 0.75	-52.54 ± 0.75	0.6392 ± 0.0044
8802.3081	87.34 ± 0.73	-48.88 ± 0.73	0.5885 ± 0.0043	8877.6509	87.64 ± 0.58	-55.37 ± 0.58	0.6401 ± 0.0037
8805.3849	87.06 ± 0.61	-42.77 ± 0.61	0.5419 ± 0.0033	8878.6466	96.14 ± 0.78	-41.23 ± 0.78	0.5782 ± 0.0041
8805.6111	91.22 ± 1.11	-43.59 ± 1.11	0.5563 ± 0.0059	8880.3072	82.58 ± 0.49	-60.64 ± 0.49	0.5833 ± 0.0030
8806.4968	95.46 ± 1.11	-42.29 ± 1.11	0.5915 ± 0.0060	8880.6416	83.83 ± 0.44	-55.21 ± 0.44	0.5912 ± 0.0027
8810.2402	84.48 ± 1.08	-55.27 ± 1.08	0.4748 ± 0.0053	8881.3059	83.65 ± 0.61	-41.92 ± 0.61	0.5960 ± 0.0038
8810.6246	84.97 ± 0.99	-56.21 ± 0.99	0.5366 ± 0.0054	8881.6346	87.98 ± 0.62	-42.09 ± 0.62	0.5648 ± 0.0034
8811.6303	84.02 ± 0.91	-54.79 ± 0.91	0.5344 ± 0.0050	8884.2778	90.88 ± 0.76	-39.68 ± 0.76	0.5408 ± 0.0039
8812.8332	87.11 ± 0.98	-49.34 ± 0.98	0.5170 ± 0.0050	8885.2973	84.90 ± 0.55	-51.12 ± 0.55	0.4749 ± 0.0027
8816.2459	85.36 ± 0.65	-48.82 ± 0.65	0.4225 ± 0.0028	8885.6416	90.31 ± 0.86	-50.73 ± 0.86	0.4785 ± 0.0040
8818.3911	80.34 ± 0.81	-47.93 ± 0.81	0.4493 ± 0.0039	8886.2977	90.76 ± 0.72	-55.53 ± 0.72	0.4438 ± 0.0030
8818.6059	81.97 ± 0.88	-46.56 ± 0.88	0.4665 ± 0.0043	8887.3368	78.42 ± 0.54	-65.67 ± 0.54	0.4310 ± 0.0026
8819.4005	77.92 ± 0.58	-43.78 ± 0.58	0.4222 ± 0.0027	8887.6513	76.67 ± 0.72	-65.12 ± 0.72	0.4598 ± 0.0037
8819.5133	82.39 ± 0.66	-44.21 ± 0.66	0.4252 ± 0.0029	8888.6345	81.99 ± 0.61	-50.48 ± 0.61	0.4196 ± 0.0027
8819.6248	87.63 ± 0.94	-45.58 ± 0.94	0.4336 ± 0.0040	8893.6390	83.75 ± 0.90	-48.33 ± 0.90	0.3468 ± 0.0032
8820.3047	84.46 ± 1.00	-51.04 ± 1.00	0.3833 ± 0.0040	8895.6481	83.99 ± 0.87	-44.74 ± 0.87	0.3056 ± 0.0027
8820.3363	86.54 ± 0.83	-49.49 ± 0.83	0.3935 ± 0.0033	8897.6450	68.52 ± 0.81	-56.15 ± 0.81	0.3354 ± 0.0034
8821.3717	93.33 ± 1.32	-55.26 ± 1.32	0.4370 ± 0.0053	8899.6473	89.32 ± 1.25	-65.58 ± 1.25	0.2432 ± 0.0029
8822.2635	74.45 ± 0.64	-60.99 ± 0.64	0.3991 ± 0.0030	8904.6433	77.94 ± 1.14	-47.11 ± 1.14	0.2524 ± 0.0032
8822.3857	82.99 ± 1.06	-57.78 ± 1.06	0.4348 ± 0.0048	8906.6573	85.41 ± 1.26	-47.50 ± 1.26	0.2283 ± 0.0029
8826.7112	77.85 ± 1.06	-35.38 ± 1.06	0.3400 ± 0.0040				
8827.2875	84.66 ± 0.73	-36.62 ± 0.73	0.3459 ± 0.0026				
8828.2416	78.27 ± 0.73	-51.17 ± 0.73	0.3707 ± 0.0030				
8831.8150	74.03 ± 0.79	-61.50 ± 0.79	0.3819 ± 0.0035				
8832.6416	75.22 ± 0.83	-57.21 ± 0.83	0.3277 ± 0.0032				
8832.7319	73.79 ± 0.97	-55.49 ± 0.97	0.3107 ± 0.0036				
8833.7596	87.73 ± 1.22	-62.26 ± 1.22	0.2907 ± 0.0035				
8834.6751	83.98 ± 0.97	-59.35 ± 0.97	0.2893 ± 0.0029				
8834.7817	83.18 ± 1.15	-63.35 ± 1.15	0.3109 ± 0.0037				
8837.7508	84.65 ± 0.76	-41.93 ± 0.76	0.2968 ± 0.0023				
8838.7555	86.37 ± 1.09	-50.72 ± 1.09	0.2941 ± 0.0032				
8840.6453	85.68 ± 0.89	-47.67 ± 0.89	0.2522 ± 0.0023				
8843.3750	81.11 ± 1.00	-60.12 ± 1.00	0.2910 ± 0.0031				
8843.6294	79.19 ± 0.82	-58.63 ± 0.82	0.2856 ± 0.0025				
8846.7118	74.19 ± 0.89	-62.68 ± 0.89	0.3368 ± 0.0035				
8847.2837	79.12 ± 0.77	-37.23 ± 0.77	0.3109 ± 0.0026				
8847.3196	94.56 ± 1.36	-37.28 ± 1.36	0.3327 ± 0.0041				
8847.5933	86.25 ± 0.83	-28.52 ± 0.83	0.3101 ± 0.0026				

Table B5. H β Gaussian Parameters for Excess Emission. The HJD column is HJD - 2,450,000.

HJD	FWHM (km s ⁻¹)	Center (km s ⁻¹)	Height (Norm. Flux)	HJD	FWHM (km s ⁻¹)	Center (km s ⁻¹)	Height (Norm. Flux)
7987.5452	107.95 ± 4.20	-103.93 ± 4.20	0.1232 ± 0.0043	8026.3733	30.18 ± 2.21	-44.47 ± 2.21	0.0466 ± 0.0031
7988.4413	119.90 ± 2.73	-12.40 ± 2.73	0.1075 ± 0.0021	8026.4026	23.57 ± 1.43	-53.75 ± 1.43	0.0524 ± 0.0027
7989.4361	139.79 ± 3.78	-42.80 ± 3.78	0.1092 ± 0.0026	8026.4160	31.84 ± 2.31	-46.20 ± 2.31	0.0432 ± 0.0028
7990.4747	108.54 ± 2.39	-81.45 ± 2.39	0.1279 ± 0.0024	8032.3226	22.51 ± 1.92	-31.91 ± 1.92	0.0449 ± 0.0027
7990.5549	106.35 ± 2.32	-77.11 ± 2.32	0.1315 ± 0.0025	8033.3153	4.89 ± 1.00	-310.56 ± 1.01	-0.0370 ± 0.0063
7990.6008	119.97 ± 3.10	-72.90 ± 3.10	0.1277 ± 0.0028	8036.2965	17.23 ± 1.71	-55.31 ± 1.71	0.0370 ± 0.0035
7991.4147	112.91 ± 1.91	-27.30 ± 1.91	0.1401 ± 0.0020	8037.2970	3.00 ± 1.41	-307.36 ± 1.41	-0.0423 ± 0.0067
7991.4571	112.23 ± 2.34	-19.91 ± 2.34	0.1393 ± 0.0025	8040.3018	15.94 ± 2.39	-99.62 ± 2.39	-0.0324 ± 0.0036
7992.4143	125.17 ± 2.79	-55.56 ± 2.79	0.1396 ± 0.0027	8040.3305	19.23 ± 2.96	165.30 ± 2.96	-0.0269 ± 0.0039
7992.4566	114.31 ± 2.34	-51.48 ± 2.34	0.1354 ± 0.0024	8040.3612	17.05 ± 2.36	-97.95 ± 2.36	-0.0398 ± 0.0052
7992.4990	148.38 ± 3.74	-57.14 ± 3.74	0.1354 ± 0.0029	8043.4325	23.28 ± 3.50	35.68 ± 3.50	-0.0280 ± 0.0038
7992.5414	142.52 ± 3.86	-57.66 ± 3.86	0.1345 ± 0.0032	8180.2874	94.56 ± 1.79	-46.32 ± 1.79	0.1927 ± 0.0031
7992.5840	124.70 ± 2.97	-60.11 ± 2.97	0.1359 ± 0.0028	8181.2967	99.22 ± 1.69	-61.63 ± 1.69	0.1911 ± 0.0028
7992.6265	141.00 ± 3.81	-64.67 ± 3.81	0.1391 ± 0.0032	8191.2859	89.43 ± 1.01	-39.65 ± 1.01	0.2203 ± 0.0021
7994.4410	108.09 ± 1.75	-26.87 ± 1.75	0.1492 ± 0.0021	8337.5458	16.73 ± 2.00	22.97 ± 2.00	-0.0490 ± 0.0049
7994.4835	133.36 ± 3.22	-27.64 ± 3.22	0.1550 ± 0.0033	8339.5539	16.78 ± 2.54	-106.34 ± 2.54	-0.0354 ± 0.0045
7994.5486	126.16 ± 2.89	-25.41 ± 2.89	0.1557 ± 0.0031	8341.5381	17.46 ± 3.06	-40.73 ± 3.06	0.0343 ± 0.0057
7995.4308	124.84 ± 2.50	-57.32 ± 2.50	0.1470 ± 0.0025	8345.5266	39.53 ± 2.65	-42.22 ± 2.65	0.0702 ± 0.0040
7995.5660	130.74 ± 3.11	-62.69 ± 3.11	0.1503 ± 0.0031	8346.5752	70.46 ± 3.86	-123.92 ± 3.86	0.0603 ± 0.0029
8000.4166	95.90 ± 1.69	-33.92 ± 1.69	0.1570 ± 0.0024	8346.6401	68.55 ± 3.78	-118.15 ± 3.78	0.0640 ± 0.0030
8001.4203	107.01 ± 2.01	-59.94 ± 2.01	0.1494 ± 0.0024	8349.4227	76.45 ± 2.29	-112.63 ± 2.29	0.0895 ± 0.0024
8001.4630	105.07 ± 1.97	-60.77 ± 1.97	0.1582 ± 0.0026	8350.4430	109.81 ± 3.00	7.56 ± 3.00	0.1003 ± 0.0024
8001.5059	94.87 ± 1.99	-65.14 ± 1.99	0.1490 ± 0.0027	8357.4494	115.19 ± 2.27	-67.77 ± 2.27	0.1404 ± 0.0024
8004.4185	98.70 ± 1.75	-62.28 ± 1.75	0.1693 ± 0.0026	8357.5413	110.62 ± 2.14	-67.24 ± 2.14	0.1339 ± 0.0023
8009.4014	94.80 ± 1.78	-49.98 ± 1.78	0.1515 ± 0.0025	8357.5837	106.62 ± 2.10	-67.85 ± 2.10	0.1433 ± 0.0025
8009.4070	94.53 ± 1.68	-40.70 ± 1.68	0.1497 ± 0.0023	8359.4581	112.43 ± 2.44	-20.41 ± 2.44	0.1385 ± 0.0025
8009.4496	94.74 ± 1.80	-43.89 ± 1.80	0.1533 ± 0.0025	8362.4822	113.78 ± 1.92	-34.72 ± 1.92	0.1474 ± 0.0021
8009.4922	92.94 ± 1.57	-45.73 ± 1.57	0.1501 ± 0.0022	8363.4887	104.39 ± 1.64	-53.60 ± 1.64	0.1571 ± 0.0021
8011.3676	79.90 ± 1.31	-50.12 ± 1.31	0.1265 ± 0.0018	8363.5459	106.47 ± 1.76	-52.60 ± 1.76	0.1500 ± 0.0021
8011.4101	75.09 ± 1.42	-41.64 ± 1.42	0.1292 ± 0.0021	8364.5478	102.87 ± 1.40	-36.79 ± 1.40	0.1497 ± 0.0018
8011.4527	76.96 ± 1.27	-45.80 ± 1.27	0.1267 ± 0.0018	8365.4541	103.69 ± 1.86	-36.39 ± 1.86	0.1469 ± 0.0023
8011.4954	78.68 ± 1.18	-44.07 ± 1.18	0.1311 ± 0.0017	8366.4522	107.33 ± 2.08	-54.03 ± 2.08	0.1514 ± 0.0025
8012.3550	81.08 ± 1.58	-43.14 ± 1.58	0.1140 ± 0.0020	8368.4562	94.93 ± 1.59	-44.96 ± 1.59	0.1456 ± 0.0021
8012.3977	95.74 ± 2.69	-42.30 ± 2.70	0.1303 ± 0.0032	8369.4500	111.68 ± 2.43	-44.45 ± 2.43	0.1338 ± 0.0025
8012.4403	106.95 ± 3.43	-45.20 ± 3.43	0.1282 ± 0.0035	8370.4549	97.99 ± 2.33	-32.90 ± 2.33	0.1180 ± 0.0025
8012.4830	93.17 ± 2.19	-47.07 ± 2.19	0.1209 ± 0.0024	8371.4276	97.95 ± 2.51	-55.60 ± 2.51	0.1151 ± 0.0025
8013.3595	85.96 ± 1.93	-56.59 ± 1.93	0.1151 ± 0.0023	8372.4785	97.47 ± 2.28	-51.39 ± 2.28	0.1102 ± 0.0022
8013.4023	83.03 ± 1.82	-59.17 ± 1.82	0.1132 ± 0.0021	8372.4872	93.84 ± 2.23	-45.81 ± 2.23	0.1120 ± 0.0023
8015.3894	72.19 ± 1.45	-24.42 ± 1.45	0.0877 ± 0.0015	8373.4747	103.24 ± 3.17	-34.35 ± 3.17	0.0983 ± 0.0027
8015.4320	69.72 ± 1.25	-29.76 ± 1.25	0.0887 ± 0.0014	8373.5119	101.36 ± 3.38	-42.50 ± 3.38	0.0988 ± 0.0028
8016.4588	68.90 ± 1.68	-30.08 ± 1.68	0.0819 ± 0.0018	8376.4731	104.16 ± 3.27	-41.41 ± 3.27	0.0843 ± 0.0023
8016.5013	69.39 ± 2.30	-31.37 ± 2.30	0.0750 ± 0.0021	8377.4148	96.78 ± 3.66	-47.62 ± 3.66	0.0814 ± 0.0027
8017.4092	72.07 ± 2.18	-41.16 ± 2.18	0.0697 ± 0.0018	8377.4921	89.38 ± 2.52	-48.35 ± 2.52	0.0835 ± 0.0020
8017.4516	70.14 ± 1.86	-46.02 ± 1.86	0.0737 ± 0.0017	8379.5082	87.91 ± 3.87	-33.94 ± 3.87	0.0657 ± 0.0024
8018.4862	57.80 ± 1.94	-53.05 ± 1.94	0.0729 ± 0.0020	8385.5020	36.60 ± 1.81	-37.23 ± 1.81	0.0487 ± 0.0021
8019.3480	58.06 ± 4.08	-50.31 ± 4.08	0.0526 ± 0.0028	8386.4720	62.23 ± 4.08	-65.57 ± 4.08	0.0248 ± 0.0014
8019.3906	74.92 ± 2.46	-50.22 ± 2.46	0.0594 ± 0.0016	8387.4332	22.75 ± 1.40	-45.52 ± 1.40	0.0499 ± 0.0026
8019.4335	73.03 ± 2.91	-55.26 ± 2.91	0.0583 ± 0.0021	8398.3767	8.54 ± 1.38	528.76 ± 1.38	0.0695 ± 0.0098
8019.4764	65.73 ± 2.52	-44.76 ± 2.52	0.0631 ± 0.0021	8400.4563	14.30 ± 2.04	-44.61 ± 2.04	0.0364 ± 0.0040
8019.5190	64.60 ± 3.43	-43.27 ± 3.43	0.0570 ± 0.0025	8401.4382	38.22 ± 2.99	-116.27 ± 3.01	-0.0400 ± 0.0031
8020.3865	56.35 ± 2.67	-34.26 ± 2.67	0.0552 ± 0.0019	8401.4578	19.36 ± 2.25	-104.18 ± 2.26	-0.0344 ± 0.0035
8020.4292	57.03 ± 2.06	-36.77 ± 2.06	0.0592 ± 0.0018	8404.4002	27.28 ± 2.17	-55.07 ± 2.17	0.0514 ± 0.0035
8020.4721	49.71 ± 3.13	-45.13 ± 3.13	0.0643 ± 0.0035	8405.3428	63.72 ± 2.73	17.82 ± 2.73	0.0540 ± 0.0021
8021.3369	42.95 ± 1.34	-57.23 ± 1.34	0.0744 ± 0.0020	8407.5264	89.60 ± 3.39	-91.51 ± 3.39	0.0737 ± 0.0025
8021.3797	40.32 ± 1.75	-52.90 ± 1.75	0.0615 ± 0.0023	8409.3058	86.60 ± 2.82	-40.03 ± 2.82	0.0907 ± 0.0026
8021.4226	33.92 ± 2.28	-56.63 ± 2.28	0.0637 ± 0.0037	8409.5829	96.48 ± 2.16	-67.53 ± 2.16	0.0803 ± 0.0015
8021.4519	34.37 ± 1.31	-58.32 ± 1.31	0.0615 ± 0.0020	8410.4964	103.89 ± 2.57	-60.77 ± 2.57	0.1000 ± 0.0022
8021.4655	43.08 ± 1.37	-56.58 ± 1.37	0.0622 ± 0.0017	8411.3838	74.45 ± 1.54	0.36 ± 1.54	0.1397 ± 0.0025
8021.5084	39.07 ± 1.82	-55.46 ± 1.82	0.0646 ± 0.0026	8411.4720	75.75 ± 1.80	-4.44 ± 1.80	0.1390 ± 0.0028
8022.4587	40.97 ± 2.83	-48.35 ± 2.83	0.0518 ± 0.0025	8412.4934	184.35 ± 4.87	-62.46 ± 4.87	0.1011 ± 0.0023
8023.3396	67.96 ± 4.84	-71.40 ± 4.84	0.0475 ± 0.0025	8413.4110	88.52 ± 1.69	-49.31 ± 1.69	0.1425 ± 0.0023
8023.4082	49.79 ± 2.72	-77.58 ± 2.72	0.0435 ± 0.0021	8416.4004	94.72 ± 1.51	-56.22 ± 1.51	0.1565 ± 0.0021
8024.3935	46.97 ± 2.01	-43.80 ± 2.01	0.0530 ± 0.0020	8417.3037	79.49 ± 1.05	-24.11 ± 1.05	0.1737 ± 0.0020
8024.4651	32.44 ± 2.05	-36.74 ± 2.05	0.0578 ± 0.0031	8429.3295	95.64 ± 1.53	-60.39 ± 1.53	0.1954 ± 0.0027
8025.3880	37.58 ± 1.67	-27.66 ± 1.67	0.0508 ± 0.0020	8432.2991	98.93 ± 1.69	-52.94 ± 1.69	0.1706 ± 0.0025
8025.4309	39.59 ± 2.13	-24.51 ± 2.13	0.0461 ± 0.0021	8434.2726	85.59 ± 1.20	-31.40 ± 1.20	0.1965 ± 0.0024
8026.3308	53.29 ± 3.44	-31.43 ± 3.44	0.0383 ± 0.0022	8436.3603	93.23 ± 1.25	-45.40 ± 1.25	0.1818 ± 0.0021

Table B5 – *continued* H β Gaussian Parameters for Excess Emission. The HJD column is HJD - 2,450,000.

HJD	FWHM (km s ⁻¹)	Center (km s ⁻¹)	Height (Norm. Flux)	HJD	FWHM (km s ⁻¹)	Center (km s ⁻¹)	Height (Norm. Flux)
8437.3468	87.24 ± 1.12	-37.61 ± 1.12	0.1880 ± 0.0021	8768.4380	97.33 ± 1.61	-55.57 ± 1.61	0.1129 ± 0.0016
8438.3249	95.88 ± 1.54	-52.19 ± 1.54	0.1702 ± 0.0024	8769.3668	87.70 ± 1.97	-70.35 ± 1.97	0.1525 ± 0.0029
8438.4520	100.96 ± 2.48	-42.19 ± 2.48	0.1784 ± 0.0038	8769.3947	77.55 ± 0.95	-66.21 ± 0.95	0.1516 ± 0.0016
8441.2979	92.03 ± 1.38	-54.03 ± 1.38	0.1713 ± 0.0022	8770.3383	75.15 ± 0.91	-26.44 ± 0.91	0.1575 ± 0.0016
8441.4473	107.27 ± 2.16	-47.56 ± 2.16	0.1749 ± 0.0030	8770.4298	73.47 ± 0.88	-22.98 ± 0.88	0.1621 ± 0.0017
8443.4107	105.18 ± 2.78	-58.25 ± 2.78	0.1644 ± 0.0038	8776.3572	80.54 ± 1.23	-37.84 ± 1.23	0.2202 ± 0.0029
8444.3055	96.90 ± 2.17	-45.77 ± 2.17	0.1736 ± 0.0033	8778.3498	97.55 ± 1.46	-41.55 ± 1.46	0.2151 ± 0.0028
8451.3159	79.38 ± 1.77	-40.28 ± 1.77	0.1188 ± 0.0023	8778.5186	114.02 ± 2.20	-42.44 ± 2.20	0.2234 ± 0.0037
8454.2752	70.33 ± 1.76	-41.36 ± 1.76	0.1119 ± 0.0025	8778.6023	103.10 ± 1.49	-36.51 ± 1.49	0.2212 ± 0.0028
8457.3021	72.83 ± 1.84	-48.86 ± 1.84	0.0830 ± 0.0018	8778.6642	104.23 ± 1.98	-36.75 ± 1.98	0.2201 ± 0.0036
8479.2329	29.79 ± 3.23	-48.95 ± 3.23	0.0383 ± 0.0034	8782.3610	98.81 ± 1.13	-52.33 ± 1.13	0.2127 ± 0.0021
8480.2246	18.33 ± 2.75	-34.37 ± 2.75	0.0332 ± 0.0043	8782.4243	96.90 ± 1.01	-57.63 ± 1.01	0.2121 ± 0.0019
8480.2827	16.58 ± 2.03	-46.44 ± 2.03	0.0406 ± 0.0042	8783.3183	83.73 ± 0.89	-69.19 ± 0.89	0.2295 ± 0.0021
8483.2416	17.41 ± 2.93	-33.74 ± 2.93	0.0366 ± 0.0045	8783.3724	87.85 ± 1.03	-62.90 ± 1.03	0.2408 ± 0.0024
8487.3411	15.38 ± 1.59	-44.46 ± 1.59	0.0502 ± 0.0043	8783.4027	82.89 ± 0.84	-65.29 ± 0.84	0.2313 ± 0.0020
8520.2811	30.90 ± 2.90	7.02 ± 2.90	-0.0526 ± 0.0044	8794.2807	83.59 ± 1.25	-61.61 ± 1.25	0.2198 ± 0.0028
8521.2674	36.04 ± 2.92	-117.35 ± 2.92	-0.0550 ± 0.0038	8794.3721	88.04 ± 1.12	-58.30 ± 1.12	0.2101 ± 0.0023
8529.2945	33.04 ± 2.15	-114.42 ± 2.15	-0.0634 ± 0.0036	8800.4499	96.21 ± 2.38	-51.56 ± 2.38	0.1910 ± 0.0041
8713.5377	118.11 ± 4.13	-67.93 ± 4.13	-0.0409 ± 0.0012	8802.3081	95.13 ± 2.25	-46.38 ± 2.25	0.1817 ± 0.0037
8762.4578	41.37 ± 1.59	-37.94 ± 1.59	0.0741 ± 0.0024	8808.2901	89.20 ± 2.57	-54.71 ± 2.57	0.1457 ± 0.0036
8764.4331	70.46 ± 1.42	7.55 ± 1.42	0.0984 ± 0.0017	8808.4162	83.93 ± 2.38	-58.41 ± 2.38	0.1386 ± 0.0034
8766.3172	81.11 ± 2.24	-86.52 ± 2.24	0.1203 ± 0.0029	8819.4005	80.43 ± 2.97	-35.53 ± 2.97	0.1036 ± 0.0033
8766.3652	79.17 ± 1.94	-83.55 ± 1.94	0.1217 ± 0.0026	8819.5133	72.84 ± 1.83	-31.18 ± 1.83	0.0984 ± 0.0021
8766.4357	74.75 ± 1.58	-75.06 ± 1.58	0.1153 ± 0.0021	8822.2635	76.28 ± 3.14	-60.64 ± 3.14	0.0955 ± 0.0033
8767.3710	78.71 ± 1.66	-14.42 ± 1.66	0.1379 ± 0.0025	8847.2837	67.35 ± 2.18	-19.07 ± 2.18	0.0749 ± 0.0021
8767.3740	79.03 ± 2.10	-11.19 ± 2.10	0.1429 ± 0.0033	8848.2818	54.67 ± 1.49	-28.77 ± 1.49	0.0937 ± 0.0022
8767.4553	75.32 ± 1.49	-14.88 ± 1.49	0.1424 ± 0.0024	8865.2392	70.62 ± 0.67	-29.75 ± 0.67	0.2145 ± 0.0018
8768.3466	96.19 ± 1.95	-47.18 ± 1.95	0.1142 ± 0.0020	8867.2999	97.57 ± 1.73	-46.33 ± 1.73	0.2308 ± 0.0035
8768.3660	116.11 ± 3.15	-54.16 ± 3.15	0.1170 ± 0.0027				